

LA-UR 91-3750

AD-A243 198



Los Alamos National Laboratory is operated by the University of California for the United States Department of Energy under contract W-7405-ENG-36

TITLE: SIMULATIONS OF HANE/VHANE DYNAMICS

AUTHOR(S): Dan Winske, X-1

SUBMITTED TO: Report prepared for the Defense Nuclear Agency
under IACRO 91-843, Work Unit 00413

DISTRIBUTION STATEMENT A

Approved for public release;
Distribution Unlimited

Best Available Copy

91-17490



By acceptance of this article, the publisher recognizes that the U S Government retains a nonexclusive, royalty-free license to publish or reproduce the published form of this contribution, or to allow others to do so, for U S Government purposes

The Los Alamos National Laboratory requests that the publisher identify this article as work performed under the auspices of the U S Department of Energy

Los Alamos Los Alamos National Laboratory
Los Alamos, New Mexico 87545

Table of Contents

<u>Section</u>	<u>Page</u>
Title	i
Abstract	i
Table of Contents	ii
Summary	1
1. VHANE simulations	4
2. Energy depositon spectrum in a HANE burst	22
3. Debris/air interactions	42
4. Parallel streaming debris model	69
5. Multibursts	84

Accession For	
USCIB OP441	50
OP441 Tab	11
Accession Number	11
Justification	
By	
Distribution/	
Availability Codes	
Dist	Avail and/or Special
A-1	



Summary

We briefly summarize work carried out in FY91 at Los Alamos in relation to high altitude nuclear bursts. This summary is subdivided into five parts, each representing different aspects of the work. Details of the individual tasks are found in the following sections of the report, each of which is self contained. For each part we briefly discuss the purpose of the work, how it was carried out, the principal results, the consequences, and proposed future studies. The sections are titled: (1) VHANE simulations, (2) Energy deposition spectrum in a HANE burst, (3) Debris/air interactions, (4) Parallel streaming deposition model, and (5) Multibursts.

1. VHANE simulations. This study involved determining the size of the magnetic cavity in a VHANE burst as well as characterizing the properties of the debris and air ions after the magnetic field recovered. We used two hybrid (particle ions, massless fluid electrons) simulation models independently to investigate how the plasma expands across the magnetic field. A newly developed hybrid code that includes electromagnetic radiation was employed to study 2-D (r-z) debris expansions. It was found that the cavity extended out to about $R_B \simeq 0.8R_3$, where R_3 is the classic magnetic confinement radius obtained by equating the initial debris kinetic energy to the magnetic field energy in a sphere of radius R_3 . It was also shown that the cavity size was independent of the background air density ($n_{air} \ll n_{debris}$ or $n_{air} = 0$). A standard hybrid code was also used to study VHANE bursts expanding in the two directions perpendicular to the magnetic field and to characterize the debris when the magnetic cavity collapsed. The final debris radius was about $0.5R_2$, where R_2 is the classic confinement radius for a 2-D expansion. Some ions remained a distance $1 - 2\rho_i$ (ρ_i = ion gyroradius) outside of the main debris cloud; this fraction increased with ρ_i/R_B . The debris remained hot, with a final temperature $T_D \sim 0.5E_o$ (E_o = initial debris kinetic energy), with most of the thermalization occurring as the magnetic field recovered. The debris was also structured, with flute modes forming on the surface at the end of the expansion, as seen in numerous other calculations. The structure persisted, as the debris ions recollapsed with the magnetic field. While the calculations were done in 2-D, one anticipates similar results in 3-D, but with a smaller final radius (due to elongation of the plasma along \vec{B}) and with the debris ions about a third cooler (energy partitioned into three rather than two degrees of freedom). Overall, these results, along with those obtained by MRC, BRA, and LLNL, have led to a very good understanding of the magnetic field and debris properties in a VHANE burst. Except for multiburst effects (see Part 5), no new effort in this area is needed or planned.

2. Energy deposition spectrum in a HANE burst. This study was not part of our planned program for the year, but was carried out to help resolve a controversy between the BRA and MRC deposition spectra. Thompson's use of these spectra in NORSE calculations yielded significant differences in the phenomenology, leading to a discussion of the origin of these spectra. We carried out some 2-D hybrid simulations of relatively low yield HANE bursts (i.e., initial debris Mach number of 16) to obtain spectra of energized air ions. As these spectra were calculated locally, rather than at lower altitudes where the

deposition actually occurs, they were not deposition spectra *per se*, but exhibited characteristic features of kinetic ion (*e.g.*, BRA) calculations. The features included a double peaked spectrum in v_{\parallel} and a maximum $v_{\parallel} \geq V_D$ (=initial debris expansion velocity). We also showed examples of spectra from collisionless shocks in space that exhibited similar features. While supporting the basic BRA-type deposition spectrum, this work has also suggested the need for further BRA/MRC spectrum comparisons in NORSE calculations (J. Thompson has already carried out some additional runs) to further understand what aspects of the phenomenology are sensitive to what features of the spectrum. As the kinetic simulations also tend to show that a significant fraction of the debris energy remains undeposited, there is also a need to understand where this energy eventually goes and how to model it appropriately in the systems codes. Finally, the question of the importance of the deposition spectrum suggests the use of the AGNES laser facility to directly measure debris energy spectra (both as a function of space and time) and compare with appropriate numerical calculations.

3. Debris/air interactions. This work involved a series of hybrid simulations in the HANE and VHANE regimes to characterize the properties of the debris and air ions as a function of debris Mach number, M_D . The calculations were done in 2-D, perpendicular to the magnetic field. Generally it was found at low M_D (VHANE regime) that the debris remained well confined and heated as the magnetic field collapsed. A small number of air ions were trapped in the debris during the collapse of the field and were likewise heated. At higher M_D (≥ 4), a collisionless shock formed that heated the air ions. The debris did not completely collapse in this case, because the present simulations did not realistically let the magnetic field recover. At $M_D = 1$, aspects of both low and high M_D expansions were observed to occur: structuring of the debris and resultant heating as the magnetic cavity collapsed, like the low M_D expansions, and the formation of a weak shock and heating of the air ions, as in high M_D expansions. There was no noticeable large coupling to magnetosonic waves at $M_D = 1$, as some EMP models predict. As a function of M_D , the final debris radius increased, while the energy in the confined debris and air decreased, as M_D increased. These calculations have shown that it is possible to characterize the properties of the debris and air ions when the debris has stopped and the magnetic field recovers. At higher Mach number, some improvements in the calculations are needed to follow the evolution further in time. However, the preliminary results here are encouraging and provide the basis for developing a complete model for the debris location and energy spectrum in HANE and VHANE bursts.

4. Parallel streaming deposition model. This study involved the development of a model for the slowing and deposition of debris ions streaming relative to the air along the magnetic field via electromagnetic ion beam instabilities. We reviewed properties of the instabilities and developed simple criteria for their application to VHANE/HANE bursts. To apply these criteria we considered two simple models for the debris expansion. The first model assumed that the debris expanded uniformly. In this case the debris density quickly dropped below that of the air, and the resonant ion beam instability provided the coupling. This model indicated that the instability was reduced at lower altitudes, as the debris density

falls off rapidly from the burst point, so any coupling that might occur happens at higher altitude. The second model assumed that the debris remained in a narrow coupling shell, and hence the debris density exceeded that of the air down to low (~ 200 km) altitudes. In this case the nonresonant ion beam instability was the dominant coupling mechanism, and the stopping distance due to anomalous wave-particle collisions was shorter by about three orders of magnitude than that due to binary collisions. The two models in some sense represented extreme conditions, with the actual situation somewhere in between. Nevertheless, the calculations do suggest that anomalous debris-air coupling by electromagnetic ion streaming instabilities can lead to the deposition of the debris ions at somewhat higher altitudes than is usually assumed. Thus far, the calculations have been limited to point by point comparisons of anomalous versus binary collisional effects. What is needed is a model for the continuous slowing of the debris ions by anomalous effects, allowing for the spread of the debris and the increase in the air density at lower altitudes. Also needed are simulations of such spatially varying situations to verify the assumptions of the model.

5. Multibursts. The final topic we addressed was the question of new effects due to multiple bursts. We carried out both full particle and hybrid simulations of two simultaneous bursts in the VHANE regime. We chose the VHANE regime, because most of the physics of a single burst is now well understood. We found that many aspects of the multiburst calculations were similar to the single burst case. We observed the initial expansion of the debris ions and their compression into a thin shell, which ultimately structured. However, the two simultaneous bursts gave rise to greater heating of both the ions and electrons than in a single burst, and structure tended to be magnified rather than suppressed. We interpreted these results as being due to the interaction of the plasma from one burst with the macroscopic and microscopic fields of the second burst, rather than due to some sort of ion/ion instability. Such instabilities would tend to be numerically suppressed in the present calculations. These preliminary results suggest that treating multiple bursts as superpositions of single bursts is likely to underestimate heating and structuring effects, perhaps by a large amount. Even two bursts will lead to a larger diamagnetic cavity, enhanced fluctuations, and increased (factor of two) heating. It is felt that this is an area where the AGNES facility could be most useful. Experiments involving two explosions could be carried out in a straightforward manner to study these types of enhancements as well as to investigate ion/ion coupling in a collisionless medium.

1. VHANE Simulations

1.1 Introduction

Simulations of VHANE bursts have been carried out with two hybrid algorithms, one being a “standard” hybrid model that requires a background plasma and makes the low frequency (Darwin) approximation and the other being a new model that allows expansion into vacuum and keeps all electromagnetic radiation effects. The calculations have been done to determine the maximum spatial extent of the debris as well as the debris location and energy distribution after the magnetic bubble collapses. We first describe the results with the new hybrid algorithm in Section 1.2 and then calculations with the standard algorithm concerning the debris characteristics in Section 1.3. Conclusions are given in Section 1.4.

1.2 Debris Extent Calculations with a New Hybrid Model

1.2.A Background

In the VHANE regime the expanding debris is contained by the Earth’s magnetic field. The magnetic confinement radius R_3 is easily estimated by equating the initial kinetic energy of the debris (ion mass m_D , number N_D , velocity V_D) with the equivalent magnetic field energy in a volume of radius R_3 ,

$$\frac{1}{2}N_D m_D V_D^2 = \frac{B^2}{8\pi} \frac{4\pi}{3} R_3^3 \quad (1.1)$$

to give

$$R_3 = \left(\frac{3N_D m_D V_D^2}{B^2} \right)^{1/3} \quad (1.2)$$

If one instead assumes a 2-D expansion perpendicular to \vec{B} (as we will later), one finds a similar formula,

$$R_2 = \left(\frac{4\hat{N}_D m_D V_D^2}{B^2} \right)^{1/2} \quad (1.3)$$

with \hat{N}_D the debris line density (particles per cm^2).

The key issue is whether in an actual 3-D expansion, the debris extends out to R_3 . Kilb [1990], for example, argues that one should use $1.5B$ rather than B in Eq. (1.1) so that the actual debris expansion radius, here called R_B , reduces to

$$R_B = \left(\frac{4N_D m_D V_D^2}{3B^2} \right)^{1/3} \simeq 0.76 R_3 \quad (1.4)$$

Alternatively, Gisler and Lemons [1989] have concluded that because the debris is not expanding everywhere perpendicular to the magnetic field, as assumed in Eq. (1.1), R_B is smaller by a factor of $(0.5)^{1/3}$ so that

$$R_B \sim 0.88 R_3 \quad (1.5)$$

For typical VHANE conditions ($N_D m_D \sim 10^6 g$, $B \sim 0.3G$, $V_D \sim 2000\text{km/sec}$), one finds $R_3 \sim 1100\text{km}$. Thus, the difference between Eqs. (1.1) and (1.4) or (1.5) for the maximum extent of the debris is about 260 km.

1.2.B New Hybrid Algorithm

Particle simulations that we have carried out [Winske, 1990], as well as hybrid simulations by Brecht [private communication], Simonson and Hewett [1991], and us generally tend to show $R_B \sim 0.8R_3$, in agreement with Eq. (1.4), except in a few cases. To help resolve the differences, we have used a new hybrid algorithm [Jones *et al.*, 1989], which can treat debris expansion into a magnetized vacuum as well as into a low density background plasma and does not make the usual low frequency approximation (hence includes electromagnetic radiation).

In a "standard" hybrid code, one assumes massless electrons ($m_e = 0$) and solves the electron momentum equation for the electric field

$$m_e n_e d\vec{V}_e/dt = 0 = -en_e(\vec{E} + \vec{V}_e \times \vec{B}/c) - \vec{\nabla} p_e + en_e \eta \vec{J} \quad (1.6)$$

(where \vec{V}_e is the electron fluid velocity, \vec{E} is the electric field, \vec{B} is the magnetic field, p_e is the electron pressure, η is the resistivity, and \vec{J} is the current). The electron current ($\vec{J}_e = -en_e \vec{V}_e$) is obtained from the ion current and Ampere's law (in the Darwin limit)

$$\vec{J}_e = -\vec{J}_i + \frac{c}{4\pi} \vec{\nabla} \times \vec{B} \quad (1.7)$$

The new algorithm solves Maxwell's equations as

$$\frac{\partial \vec{E}}{\partial t} = c \vec{\nabla} \times \vec{B} - 4\pi(\vec{J}_i + \vec{J}_e) \quad (1.8)$$

$$\frac{\partial \vec{B}}{\partial t} = -c \vec{\nabla} \times \vec{E} \quad (1.9)$$

In this case Eq. (1.6) is solved for \vec{J}_e and the Eqs. (1.8-1.9) are advanced as in a standard explicit electromagnetic particle code [Birdsall and Langdon, 1985].

1.2.C Simulation Results: No Background Plasma

In order to show the utility of this approach, we have considered the axisymmetric (r-z) expansion of a debris cloud into a vacuum, in which is embedded a uniform magnetic field, $\vec{B} = B_0 \hat{z}$. Instead of expressing the initial parameters in terms of code units, we can express lengths in terms of R_3 and the time in terms of $\tau = V_D t / R_3$. The initial debris cloud has a cosine-shaped density profile that extends out to $0.125 R_3$. The ions are cold with directed radial velocity V_D such that the ratio of the gyroradius ($\rho_i = V_D / \Omega_i$, where $\Omega_i = eB_0 / m_i c$ is the ion gyrofrequency) to R_3 is 0.0625.

Figure 1.1 shows a time history of the debris ion kinetic energy E_D and the magnetic field energy E_B (in terms of the initial debris energy). As expected, E_D decreases, while E_B increases accordingly. Eventually, E_D reaches a minimum as the debris stops, while E_B maximizes as the cavity reaches its largest radius; this occurs at $\tau \simeq 1$. Figure 1.2 shows a radial cut of the magnetic field at $\tau \simeq 0.9$. The field is completely excluded from the cavity, which extends out to $R_B \simeq 0.75R_3$. At the edge of the cavity the magnetic field is compressed to a value about 40% above the ambient field. The magnetic field diffuses to some extent (the applied resistivity in terms of a collision frequency is $\nu_c/\Omega_i \sim 10$) so that the magnetic field (and density) scale length is about ρ_i . Figure 1.3 shows a contour plot of the magnetic field at $\tau \sim 0.9$. One sees a smooth cavity, with an elongation factor ($L_z/R_B \sim 1.4$), consistent with theoretical expectations [Gisler and Lemons, 1989]. Finally, Figure 1.4 shows the debris ions at various times. The ions compress into a shell as they expand, eventually reaching $R_B \simeq 0.75R_3$. A small number of ions are beginning to leak out the ends of the cloud along the z axis at this time.

1.2.D Calculation with Background Plasma

Brecht [private communication] had suggested that differences in these new hybrid calculations and in our previous particle simulations with some of the hybrid calculations done at BRA and LLNL might be due to the absence of a background plasma in our work. The above calculation was thus repeated including a low density background plasma. In the previous calculations the initial debris density was $n_D/n_c = 17280$ (n_c = code reference density), with an expansion velocity of $V_D/v_A = 0.17$, with v_A = Alfvén speed in terms of the reference density. Here, the background density was $n_o/n_c = 3.75$, so that the debris would overrun a background mass that was 10% of the debris mass if it expanded to R_3 . Figure 1.5 shows a contour plot of the debris density at $\tau \sim 1.0$. Again, the ions extend out to $R_B \simeq 0.75R_3$, consistent with the earlier result. Also, no strong anomalous heating due to the interaction of the debris ions with the background plasma was observed.

1.3 VHANE Debris Characteristics

We next consider two dimensional expansions in the plane perpendicular to the magnetic field to determine properties of the debris after the bubble collapses. The 2-D calculations allow the development of flute instabilities on the surface of the cloud and provide a good comparison with the r - z simulations of this problem by Brecht [private communication] and Simonson and Hewett [1991].

1.3.A Description of One Simulation

In this case we use a standard hybrid algorithm [e.g., Winske and Quest, 1986], making the usual assumptions of low frequency and massless electrons. The debris has an initial Gaussian shaped profile ($n_D(r) = n_D \exp(-r^2/r_o^2)$, $r_o = 0.16R_2$) with expansion velocity $V_D \gg$ the ion thermal speed (v_i , expressed in terms of $\beta_i = 8\pi n_o T_D/B_o^2$, $T_D = 0.5m_D v_i^2$). The initial peak debris density is $n_D/n_o = 41$ with $m_D/m_o = 4$, and $\beta_i = 0.01$. The expansion velocity expressed in terms of a debris Alfvén Mach number, is $M_D = V_D/v_A =$

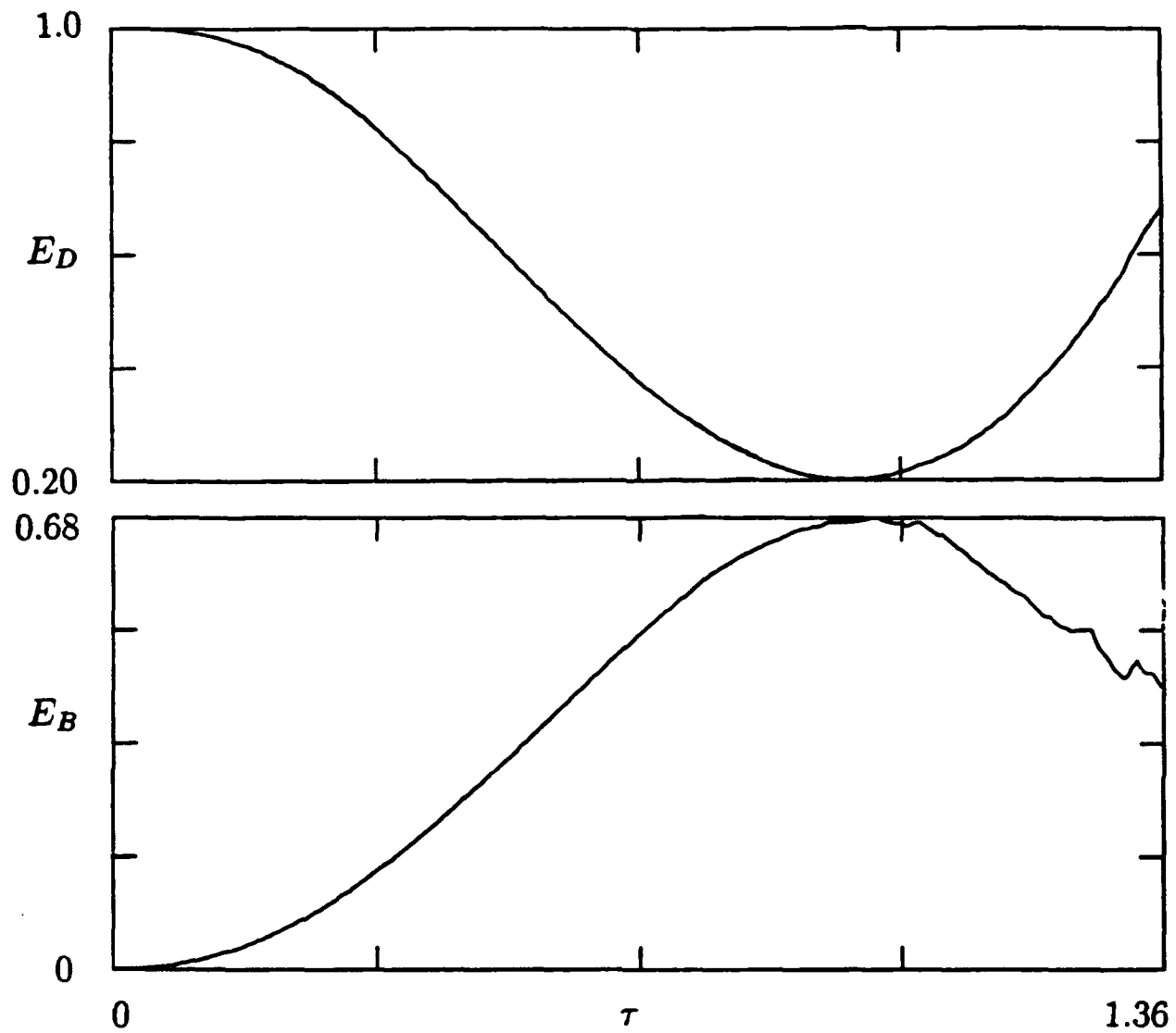


Figure 1.1. Time histories of the debris kinetic energy E_D and magnetic field energy E_B , showing decrease of E_D and corresponding increase of E_B . Maximum debris expansion occurs at $\tau \simeq 1.0$, when E_D is a minimum.

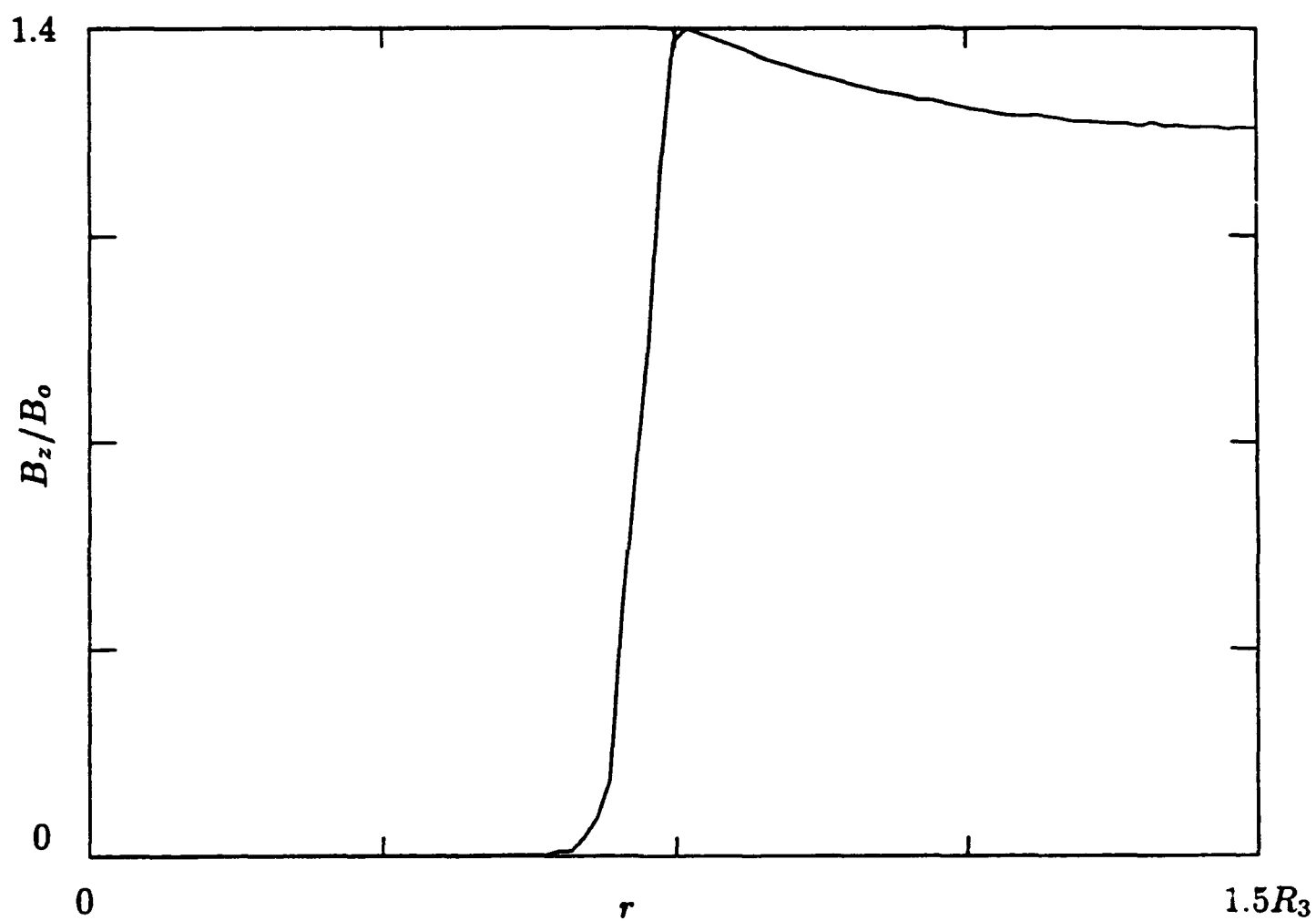


Figure 1.2. Radial cut of the magnetic field at $\tau \sim 0.9$, showing the cavity, the B field enhancement on the outside, and the steep gradient at the edge of the cavity.

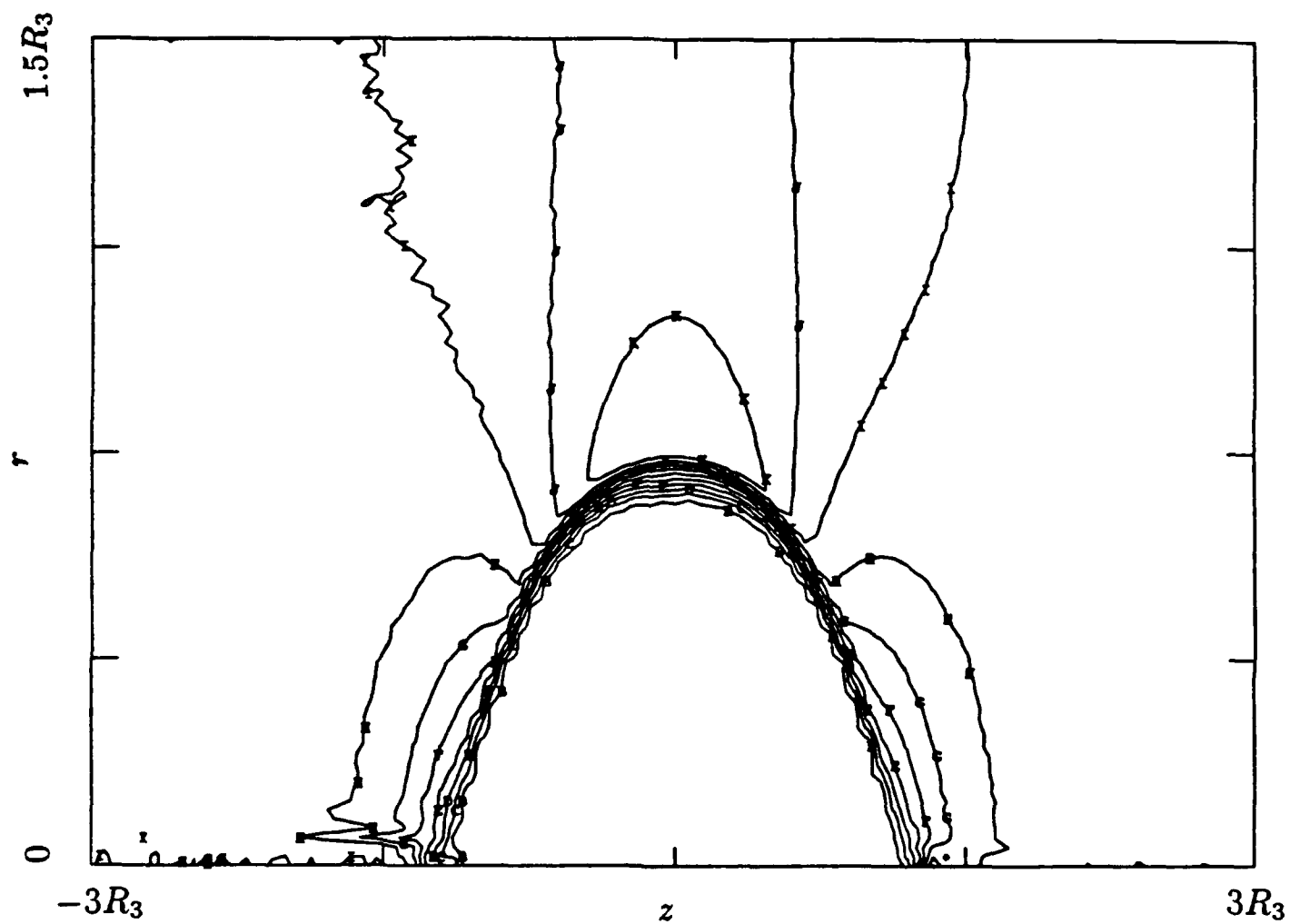


Figure 1.3. Contour plot of the magnetic field at $\tau \sim 0.9$, showing smooth cavity at maximum expansion, somewhat elongated along \vec{B} .

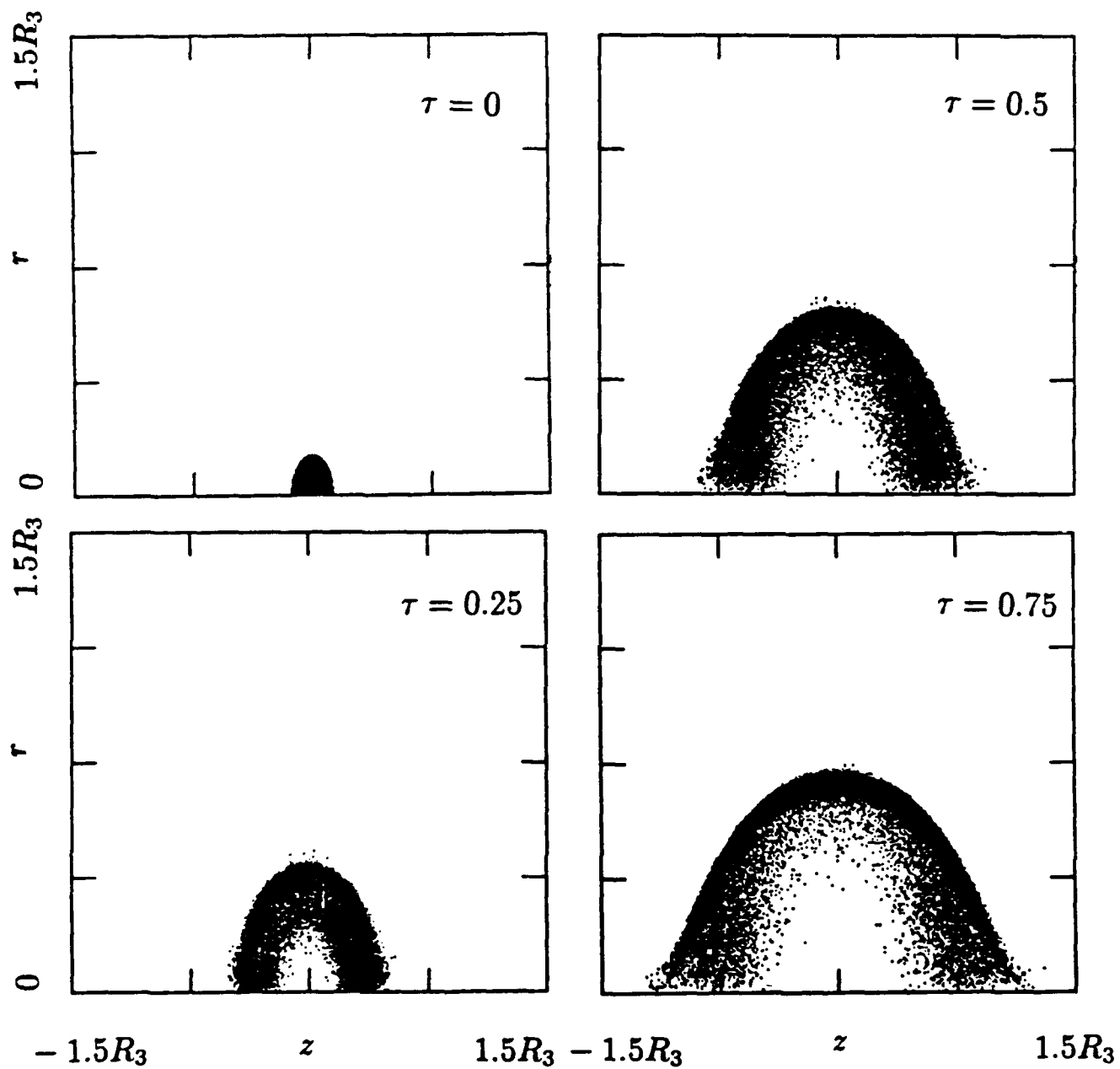


Figure 1.4. Debris ions in r - z at four times, showing expansion out to $R_B \simeq 0.75R_3$.

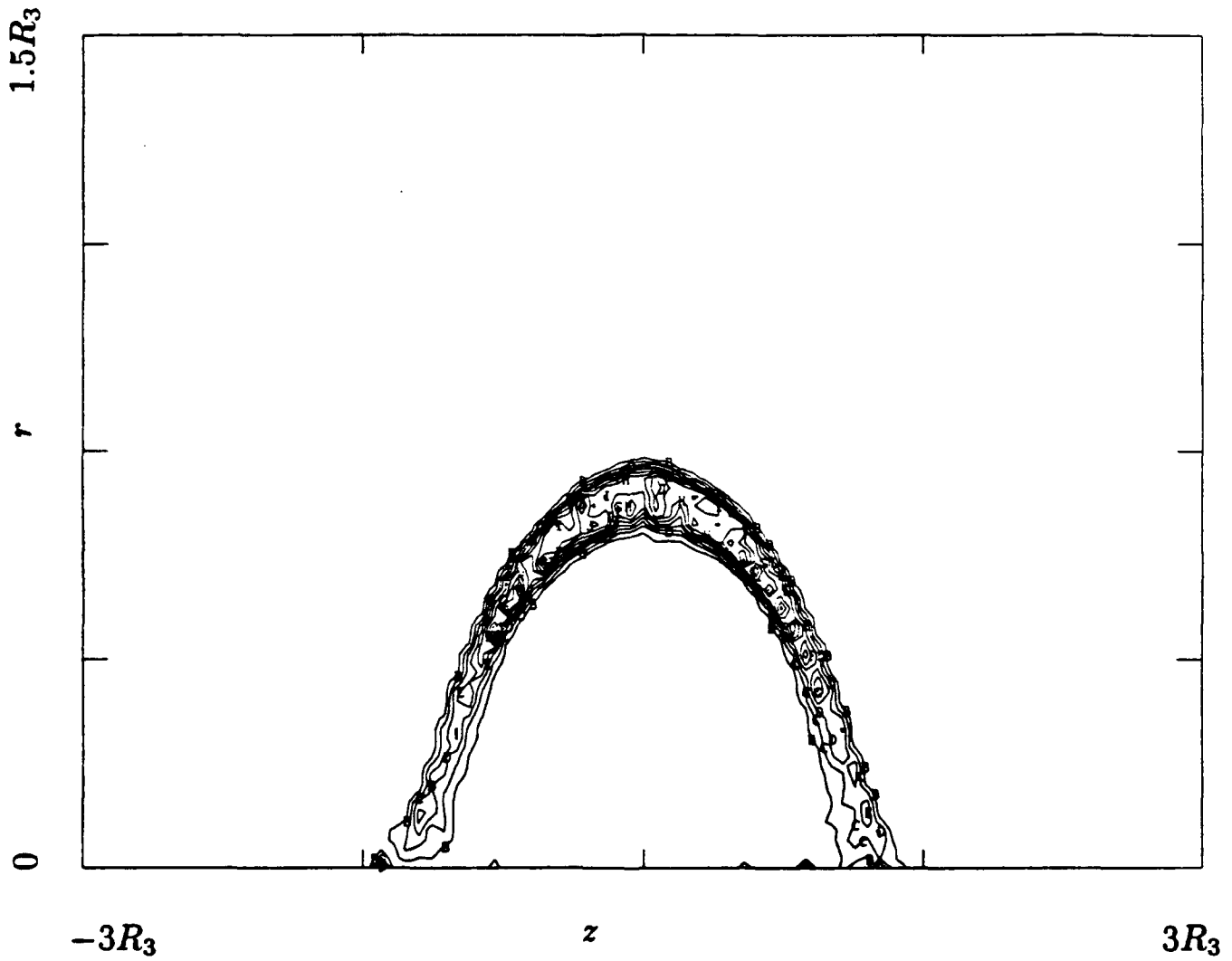


Figure 1.5. Contour plot of debris density at $\tau = 1$, showing expansion to same radius in a calculation with a weak background plasma.

0.5, with v_A defined in terms of the background density and ion mass. Figure 1.6 shows the debris density at various times. The debris expands out to a radius $r \simeq R_2$. Flute modes begin to develop as the debris stops. The flutes elongate as the plasma collapses, leading to a rather well contained, highly structured debris cloud. Figure 1.7 displays 3-D perspective plots of the debris density, the debris energy ($E_D = 0.5m_D[v_x^2 + v_y^2]$), and the background air ion energy, when the cloud has collapsed ($\Omega_i t = 80$). The highly structured nature of all three quantities is evident. Figure 1.8 shows a radial slice of the debris density and energy. We characterize the collapsed cloud in terms of an inner radius r_1 and an outer radius r_2 , along with corresponding average values of the debris density and debris and air energies in the regions $r < r_1$ and $r_1 < r < r_2$. r_1 is defined as the radius where the debris density drops to 20% of its peak value, while r_2 is the radius of maximum extent of the debris. This is not the only characterization possible, but does allow one to then compare these properties as a function of burst parameters.

In Figure 1.9 we plot the energy distribution $f(E)$ ($E = 0.5m_D[v_x^2 + v_y^2]$), normalized to the initial debris energy E_o , for the debris ions at $\Omega_i t = 40$ [top panel] at the time of maximum debris expansion, and at $\Omega_i t = 80$ [bottom panel] after the cloud has collapsed. At the earlier time most of the debris energy has gone into excluding the magnetic field. The ions have stopped at this time and remain fairly cold. When the magnetic field recollapses and gives its energy back to the debris, the debris ions have become thermalized, with some ions energized to about $4E_o$. The energy distribution function can be characterized at this time as $f(E) \sim \exp(-E/E_c)$, with $E_c \simeq 0.5E_o$.

1.3.B Scaling Studies

One parameter of interest in VHANE bursts is the ratio of the direct ion gyroradius ρ_i to R_3 . For actual VHANE's $\rho_i/R_3 \ll 1$, but numerous experimental studies, including the laser experiments at NRL [Ripin *et al.*, 1987] and LLNL [Dimonte and Wiley, 1991], and various simulations [e.g., Winske, 1990] have considered a range of ρ_i/R_3 to values exceeding unity. We thus consider a series of hybrid simulations in the manner described above, varying the value of ρ_i/R_2 . The other important parameter is $M_D = V_D/v_A$, which we will consider later.

Figure 1.10 shows the debris ions in the x-y plane at about the time of maximum bubble size for four values of ρ_i/R_2 . At small ρ_i/R_2 the ions have compressed into a thin shell, and flute modes have begun to appear on the surface. For $\rho_i/R_2 = 0.63$ the instability, which occurs at a shorter wavelength, has already heated the ions in the shell to some extent and scattered some ions to larger radius. At even larger $\rho_i/R_2 = 1.25$, some of the ions have compressed into a shell that shows no sign of instability, while more ions have been scattered to an even larger radius. The collapsed debris ions at later time are shown in Figure 1.11. In the small ρ_i/R_2 cases the debris is confined to a narrow cylinder; at intermediate ρ_i/R_2 some ions remain outside the main cloud in a thin halo. At larger ρ_i/R_2 a significant number of ions do not recollapse with the magnetic field. In the latter case, however, one questions the validity of the results. In the full particle calculations with $\rho_i/R_2 > 1$ a strong flute instability occurs at short wavelengths [Winske, 1990]. In

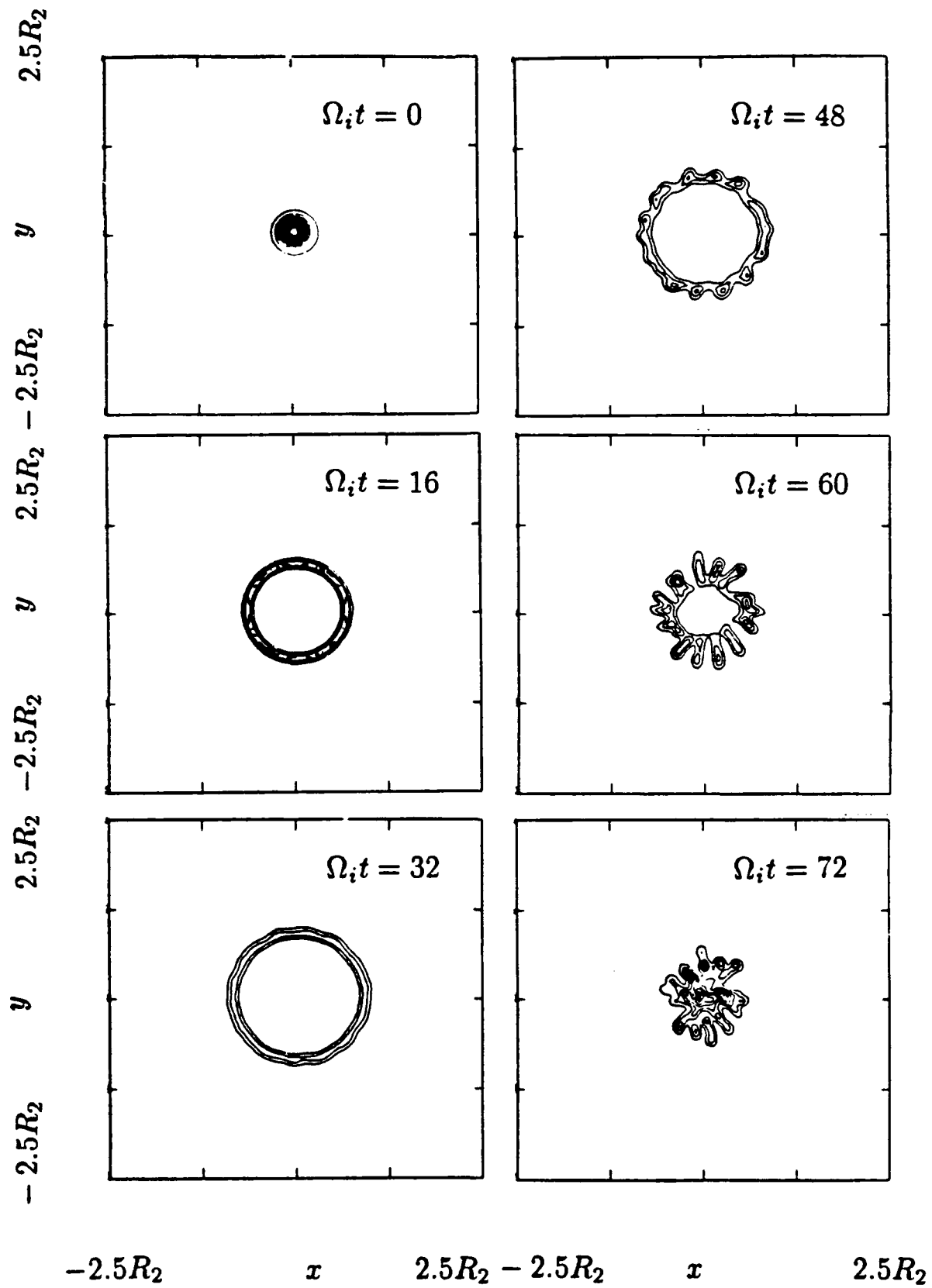


Figure 1.6. 2-D contour plot of debris density at various times for an expansion at $M_D = 0.5$ with $\rho_i/R_2 = 0.16$, showing the expansion of the debris, development of flute instability, and recollapse.

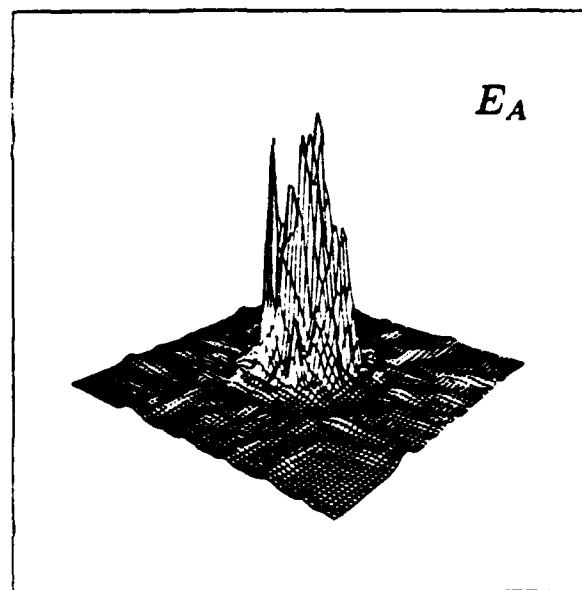
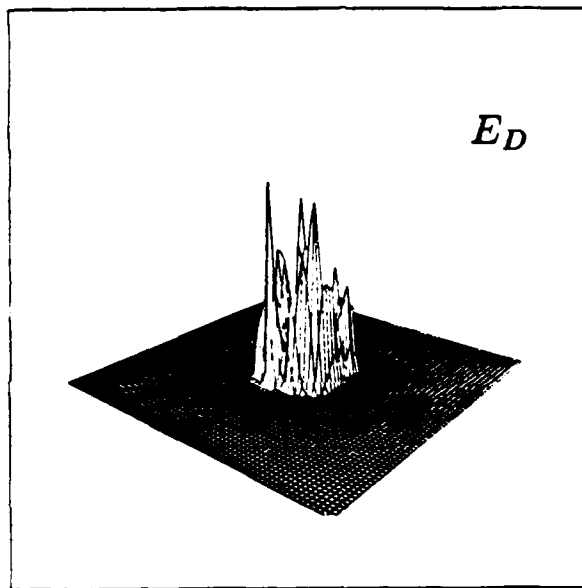
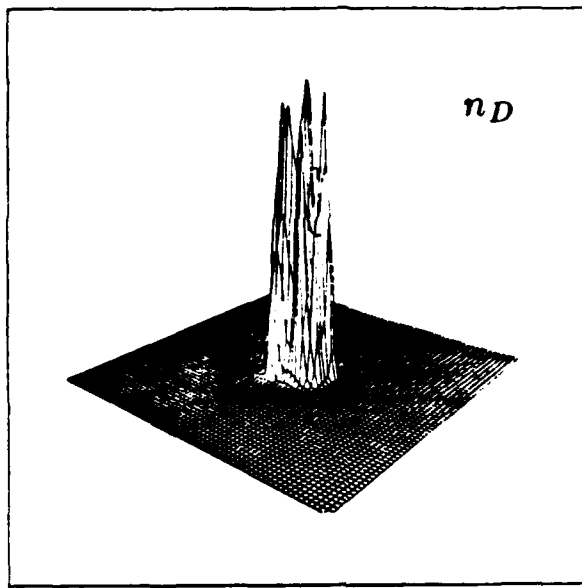


Figure 1.7. 3-D perspective plots of the debris density and debris and air ion energy at $\Omega_i t = 80$ for the same calculation, showing highly structured nature of these quantities.

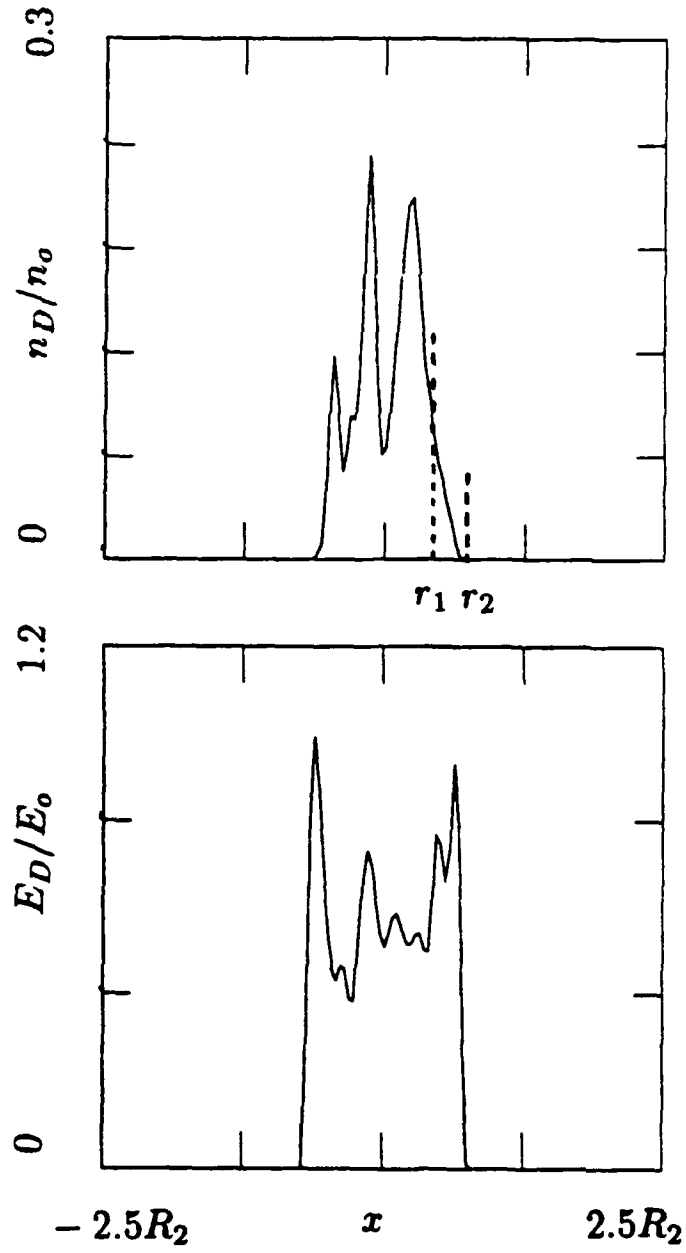


Figure 1.8. Radial slice of the debris density and energy, showing debris cloud radius r_1 and halo radius r_2 .

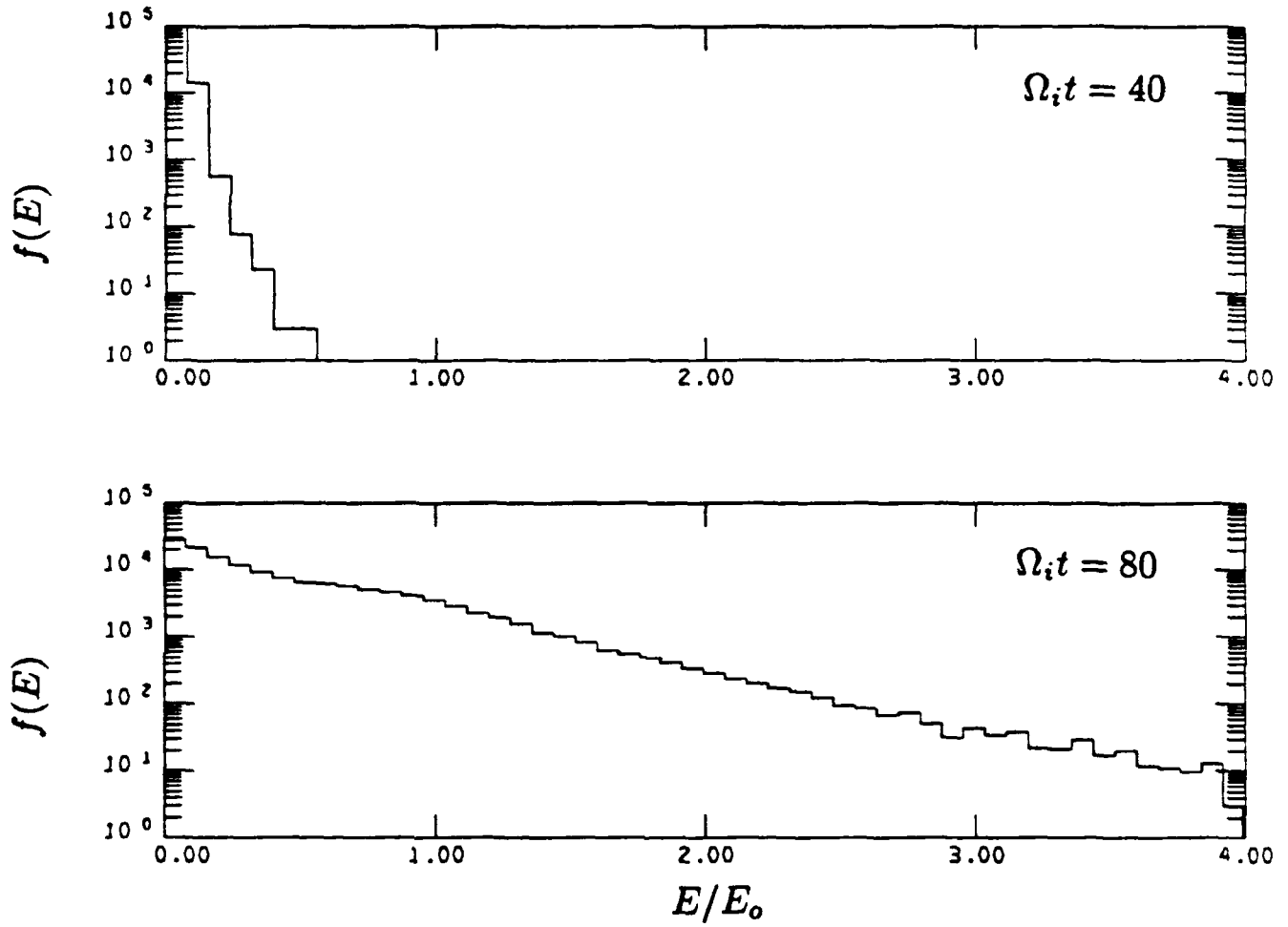


Figure 1.9. Energy distributions for the debris ions $f(E)$ at $\Omega_i t = 40$ [top panel] and $\Omega_i t = 80$ [bottom panel], showing ions thermalized when the magnetic bubble collapses.

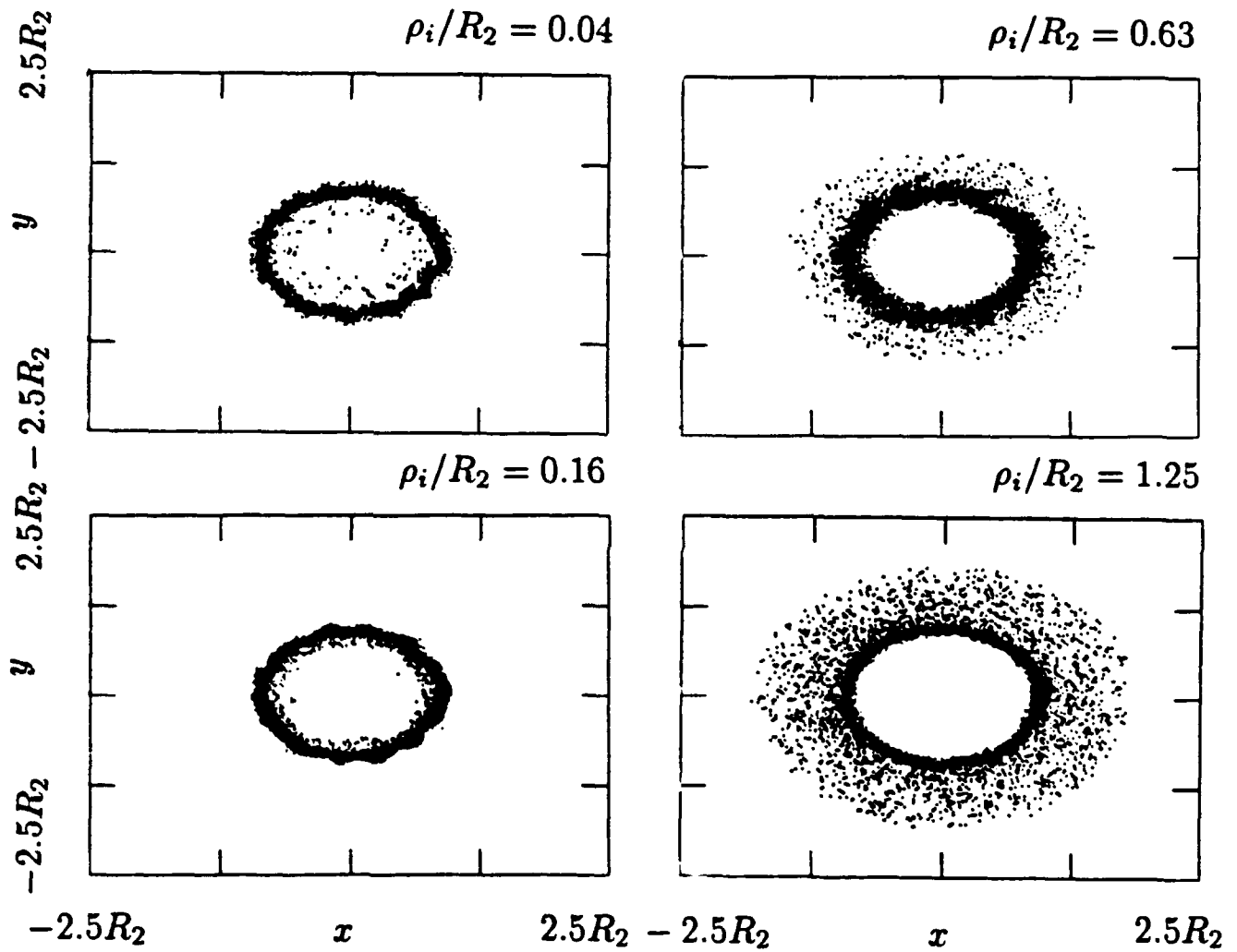


Figure 1.10. Debris ions in x-y space at about the time of maximum bubble size for four values of ρ_i/R_2 , showing some ions scattered beyond R_2 when ρ_i/R_2 is large.

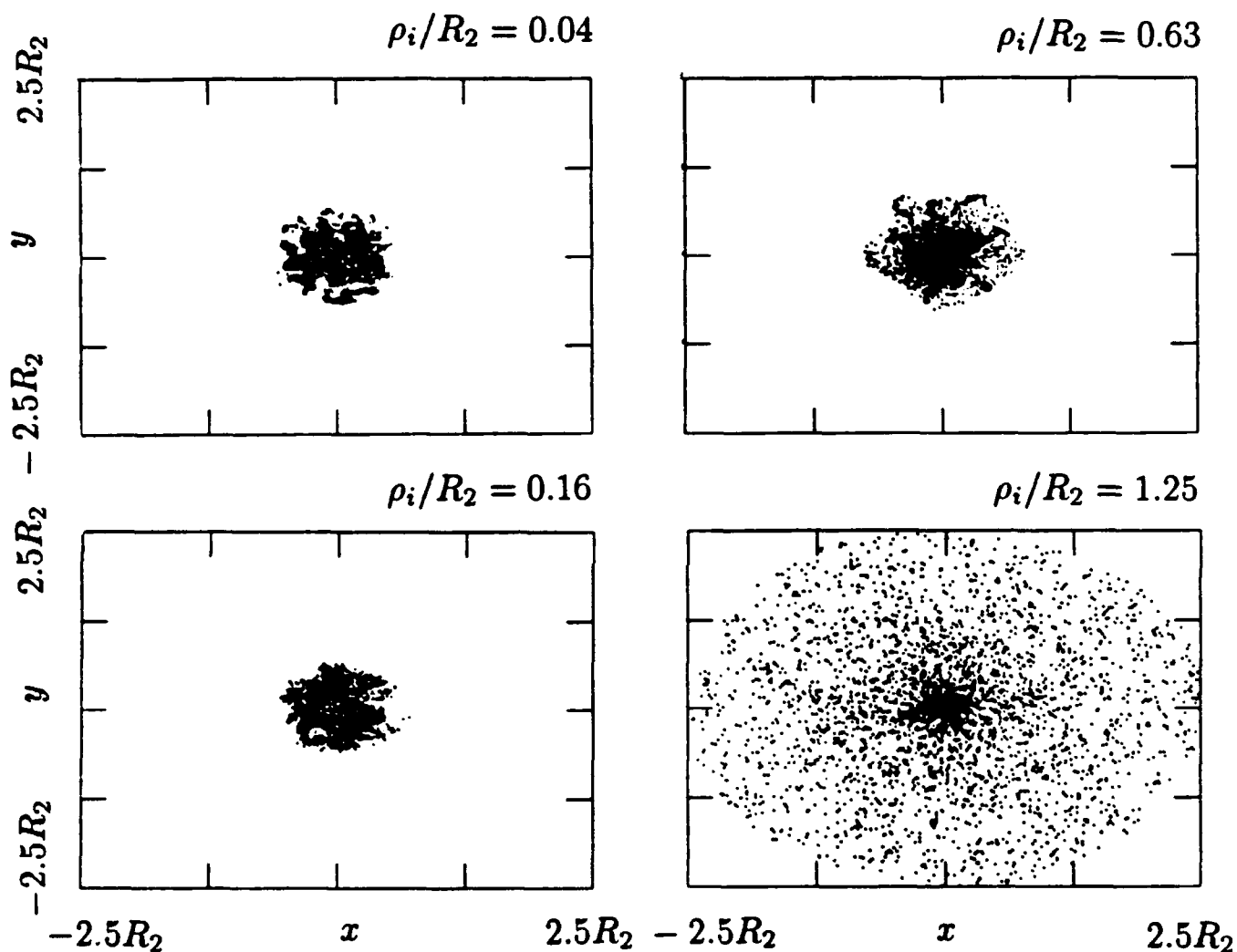


Figure 1.11. Debris ions in x-y space at about the time of bubble collapse for four values of ρ_i/R_2 . At large ρ_i/R_2 a significant number of the ions do not recollapse with the main debris cloud.

this regime charge separation effects are significant. The quasi-neutral hybrid calculations presented here, however, ignore this physics, which probably explains the absence of an instability in this case. Nevertheless, the overall tendency for some ions to remain at distances on the order of $1-2 \rho_i$ beyond the final debris column size is evident.

The results of these runs are summarized in Table 1.1. In order to vary ρ_i/R_2 keeping R_2 constant, we have changed the mass m_D and the initial density n_D of the debris ions compared to the (fixed) background m_o , n_o . Tabulated for these four runs are r_1/R_2 , n_{D1}/n_o , E_{D1}/E_o , and E_{A1}/E_o (radius r_1 , average debris density, average debris ion energy, and average air ion energy for $r < r_1$), as well as the corresponding values, r_2 , n_{D2}/n_o , E_{D2}/E_o , and E_{A2}/E_o , for $r_1 < r < r_2$, where n_o is the background density and E_o is the initial debris kinetic energy $E_o = 0.5m_D V_D^2$. The last entry in the table is $f(r > r_1)$, the fraction of debris ions that remain outside of radius r_1 . Generally, for the debris in the main cloud ($r < r_1$), r_1/R_2 decreases with ρ_i/R_2 , E_{D1} is approximately constant, and n_{D1} and E_{A1} increase with ρ_i/R_2 . In the halo region ($r_1 < r < r_2$), r_2/R_2 , n_{D2}/n_o , E_{D2}/E_o , E_{A2}/E_o , and $f(r > r_1)$ all tend to increase with ρ_i/R_2 ($0.04 < \rho_i/R_2 < 0.63$).

Ignoring the somewhat anomalous case with $\rho_i/R_2 = 1.25$, one would conclude that almost all of the debris ions tend to recollapse with the magnetic field to a radius $r_f \sim 0.5R_2$. Less than about 2% of the debris ions remain outside the main cloud in the VHANE regime ($\rho_i/R_2 < 0.04$). Due to the interaction of the debris with the magnetic field the directed debris energy becomes thermalized, with a final debris ion temperature about one-half of the initial debris kinetic energy. Air ions are trapped in the cloud as the debris collapses and are also heated to a comparable temperature. The heating of the air ions here increases with ρ_i/R_2 , because the energy is shared with fewer air ions relative to debris ions. The few debris (and the air) ions that exist in the halo around the debris cloud (halo radius $\sim 1 - 2\rho_i$) are heated to similar temperatures. In an actual 3-D expansion the cloud will also elongate along the magnetic field, leading to about a 20% small final radius across the magnetic field (i.e., $r_f \sim 0.4R_2$) when the field collapses, and with reduced temperatures (the energy being shared by all three degrees of freedom).

1.4 Conclusions

We have used two types of hybrid codes to study the debris in a VHANE burst. Calculations with a new hybrid algorithm confirm our previous simulations results and most of the LLNL and BRA calculations that in a 3-D expansion debris will extend out to about $0.8 R_3$, consistent with Kilb's estimate. The absence or presence of a background plasma makes little difference in the expansion. Two dimensional debris expansions perpendicular to the ambient magnetic field have been carried out to times comparable to the collapse of the magnetic bubble. The debris becomes structured in the field, but nevertheless collapses to a final radius, $r_f \sim 0.5R_2$, leaving only some debris ions one or two ion gyroradii beyond the collapsed cloud; the fraction of such ions decreases as ρ_i/R_2 is reduced. The debris (and air ions inside the debris cloud) become thermalized, with energies roughly half of the directed debris kinetic energy. The ratio of ρ_i/R_2 has little overall effect on the thermalization or the development of the flute instability, as long as $\rho_i/R_2 < 1$. This result seems

Table 1.1 Debris and Air Characteristics for Hybrid Runs at Various ρ_i/R_2 .

Run	1	2	3	4
n_D/n_o	163.0	41.0	10.2	5.1
m_D/m_o	1.0	4.0	16.0	32.0
ρ_i/R_B	0.04	0.16	0.63	1.3
r_1/R_B	0.61	0.53	0.45	0.25
n_{D1}/n_o	0.08	0.09	0.14	0.22
E_{D1}/E_o	0.63	0.51	0.55	0.62
E_{A1}/E_o	1.39	2.30	4.32	2.71
r_2/R_B	0.19	0.22	0.45	2.34
n_{D2}/n_o	0.002	0.003	0.009	0.0003
E_{D2}/E_o	0.34	0.69	0.91	0.27
E_{A2}/E_o	1.39	2.30	4.32	2.71
$f(r > r_1)$	0.017	0.032	0.16	0.48

somewhat contrary to our earlier results obtained with full particle codes [Winske, 1990]. However, in the particle calculations short wavelength (lower hybrid) modes dominated, which are suppressed as ρ_i/R_2 decreases. The hybrid simulations, on the other hand, involve longer wavelength modes that apparently are less susceptible to ρ_i/R_2 effects.

While the hybrid results presented here have been done only in 2-D, one expects that in 3-D the final debris radius to be slightly smaller, due to the elongation of the cloud along \vec{B} , yielding $R_f \sim 0.4 * 0.8R_3 \sim 0.3R_3$, which interestingly is similar to that which Brecht [private communication] gets in some cases when the debris anomalously slips through the field without making much of a magnetic cavity. And in 3-D one expects the debris to thermalize in all three directions to a final energy of about $1/3E_0$ (rather than $1/2E_0$ in 2-D). Yet to be determined is the slope of the more energetic part of the debris energy spectrum and the eventual deposition of the debris energy in the ionosphere.

References

- Birdsall, C. K., and A. B. Langdon, *Plasma Physics via Computer Simulation*, McGraw-Hill, 1985.
- Dimonte, G., and L. G. Wiley, Dynamics of exploding plasmas in a magnetic field, *Phys. Rev. Lett.* 67, 1755, 1991.
- Gisler, G., and D. S. Lemons, Dynamics of a plasma expanding in a uniform magnetic field, *J. Geophys. Res.*, 94, 10145, 1989.
- Jones, M. E., V. A. Thomas, R. J. Mason, and D. Winske, A fully electromagnetic hybrid model for high density plasma simulations, 13th Conf. Num. Sim. Plasmas, Sante Fe, 1989.
- Kilb, R. W., Debris location after nuclear bursts, Working Paper, November, 1990.
- Ripin, B. H., E. A. McLean, C. K. Manka, C. Pawley, J. A. Stamper, T. A. Peyser, A. N. Mostovych, J. Grun, A. B. Hassam, and J. D. Huba, Large Larmor radius interchange instability, *Phys. Rev. Lett.*, 59, 2299, 1987.
- Simonson, G., and D. W. Hewett, Recent magnetic debris containment calculations (U), Livermore National Lab. Report, UCRL-ID-10741, 1991.
- Winske, D., Plasma dynamics in very high altitude nuclear explosions: 1. Ions, Los Alamos National Lab. Report, LA-UR-90-1005, 1990.
- Winske, D., and K. B. Quest, Hybrid simulations of debris-air interactions: Ions streaming perpendicular to the magnetic field, Los Alamos National Lab. Report, LA-UR-86-4297, 1986.

2. Energy Deposition Spectrum in a HANE Burst

2.1 Introduction

The essential question for nuclear explosions at high altitudes is how the weapon energy is deposited in the atmosphere when the ambient air density is so low that, when fully ionized, the medium is collisionless. Much of the energy goes off as ionizing radiation, but some fraction remains as kinetic energy in the debris. The initial expansion velocity of the debris ions is much greater than the local Alfvén speed so that a high Mach number collisionless shock forms, which causes the debris to stop as it gives up its energy to form the shock, and energizes the air ions that are eventually deposited in the atmosphere. This complex process is modeled differently in various "first principles" codes. In CMHD [Kilb and Glen, 1978] numerical viscosity is included to stably model the air-shock process and through this viscous interaction the air ions are thermalized, resulting in a rather soft energy spectrum. In the BRA SHYPS code [Brecht and Thomas, 1988] the ion kinetics of the debris-air-shock are modeled self-consistently, resulting in a nonclassical collisionless shock and a more energetic deposition spectrum.

Recently, the consequences of these two different energy deposition spectra have been compared using the systems code NORSE [Thompson, 1991]. The spectra used as initial conditions in these two calculations differ in a number of aspects: total energy deposited (CMHD deposits about three times as much energy as SHYPS), radial distribution of the energy (SHYPS deposits more energy further from the burst point), and velocity distribution (while the CMHD spectrum falls off monotonically, the SHYPS spectrum has two peaks and extends to higher velocity). Not surprisingly, the two deposition models give rise to significantly different nuclear phenomenologies: different ionization levels, electron temperatures, and atmospheric heave. Of particular interest here are the resulting differences in the electron density, which at certain altitudes and times are about two orders of magnitude larger in the calculations using the CMHD spectra. In part this is due to the greater total energy deposited in the CMHD run and its concentration closer to the burst point field line. It is also due to the softer CMHD spectrum that deposits the energy higher in the atmosphere and shares it with fewer background ions, yielding higher electron temperatures.

In order to help understand these differences and perhaps reconcile them, we were asked by DNA to provide an independent verification of the energy deposition spectra in HANE events. Rather than reproduce the BRA result, we have carried out more restricted kinetic calculations (which we could do on a rather short time scale) to demonstrate the essential features of the spectrum. These simulations are described in Section 2.2. These features are also corroborated by observations of high Mach number collisionless shocks in space; we briefly review some of the major findings in Section 2.3. Finally, in Section 2.4 we summarize our results. We also describe other effects that may tend to bring the two models into better agreement and discuss some further tests that can be done in the systems codes to understand the differences.

2.2 Simulations

Our purpose here is to show the origin of the energized air spectrum, which is not a deposition spectrum *per se*, but which contains the essential features. As such we carry out the calculations in restricted geometries. The simulations are done with a hybrid code that treats the ions kinetically by means of particle-in-cell techniques and the electrons as a massless fluid, similar to that used by Clark *et al.* [1973], Goodrich *et al.* [1985], and Thomas and Brecht [1986]. We describe simple planar and cylindrical calculations in one and two spatial dimensions. In the planar calculations [Winske and Quest, 1986], the debris initially is uniform over the region $0 \leq x \leq L_D$ and flows in the +x direction with initial velocity V_D . The air occupies the remaining region $L_D \leq x \leq L$, is uniform, and at rest initially. A constant magnetic field of magnitude B_o , which lies in the x-y plane, fills the region. A closed system with reflecting particle boundaries, on which the electric field is zero, is assumed. In the two-dimensional calculations similar initial and boundary conditions along x are employed; in the y direction the plasma is uniform and periodic boundary conditions are imposed.

We begin with a simple 1-D simulation that shows the essential features of the interaction. In this case the debris Mach number, with the Alfvén speed defined with the air parameters ($v_A^2 = B_o^2/4\pi n_A m_A$), is 16. The system length is $L = 200c/\omega_A$ [$\omega_A^2 = 4\pi n_A e^2/m_A$], the cell size $\delta = 0.25c/\omega_A$, $m_D/m_A = 2$, $L_D = 20c/\omega_A$, $\beta_D = \beta_A = \beta_e = \beta = 1$, $c/v_A = \omega_A/\Omega_A = 4000$, and the resistivity $\eta = 10^{-5}\omega_A/4\pi$. Figure 2.1 shows the normalized debris density $n_D(x)/n_D(t=0)$ (dashed line), air density $n_A(x)/n_A(t=0)$ (solid line), and magnetic field magnitude $B(x)/B_o$ (dotted line) as a function of x. (Note that the normalized B field is given on a different scale so that it can be more easily seen in the figures.) Frames at three different times are displayed: $\Omega_A t = 0$, $\Omega_A t = 2.5$, and $\Omega_A t = 10$ ($\Omega_A = eB_o/m_A c$ = gyrofrequency of air ions). The $\Omega_A t = 0$ show the initial configuration. The steep gradients give rise to a small pulse on the magnetic field, which is not easily seen in the figure. Other initial configurations with smoother density profiles or compressed magnetic fields in the debris region have also been used. Except for some slight differences at very early time, which are to be expected, the long time behavior is similar [e.g., Clark *et al.*, 1973]. By $\Omega_A t = 2.5$ the debris, the air, and the magnetic field have all been strongly compressed, with a shock-like structure already formed. At later times, $\Omega_A t = 10$, the shock propagates to the right through the unperturbed air, while the debris spreads out and eventually stops. Note that in this strictly perpendicular configuration that there is little mixing of the debris and air plasmas; a quantitative measure of which is given in Winske and Quest [1986]. Both the magnetic field and air density show large pulses, called "overshoots", at the leading edge of the shock.

The dynamics of the interaction is better seen in $v_x - x$ phase space for both ion species at these same times, as given in Figure 2.2. Again, at $t = 0$ both species have uniform densities and velocities. At $\Omega_A t = 2.5$, the compression of the magnetic field causes the air ions at the debris-air interface to be picked up, gyrate in the compressed field to velocities larger than V_D , while the debris motion is somewhat more complicated at this early time. The dynamics at very early times have been described by Goodrich *et al.* [1985]. At later

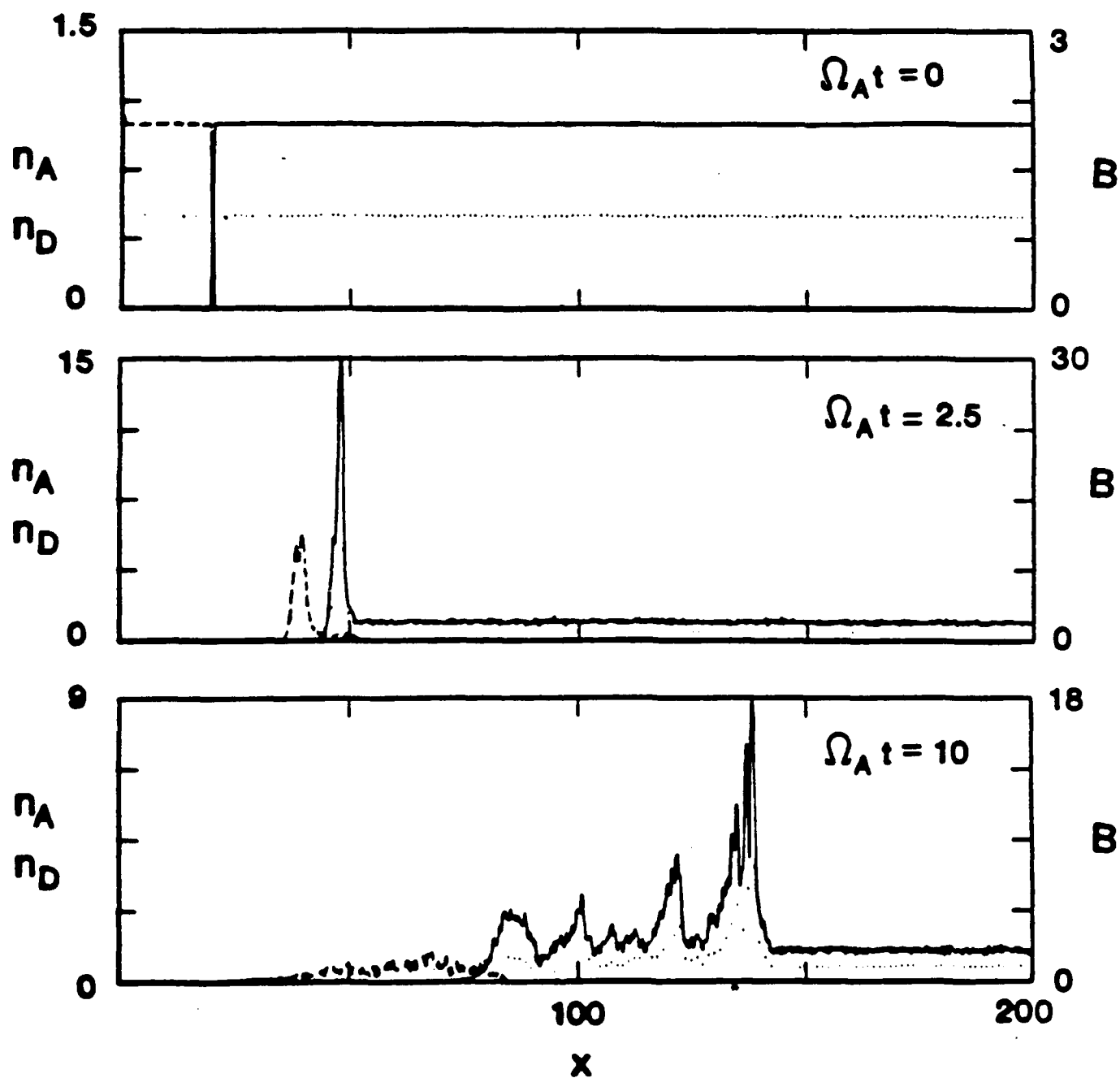


Figure 2.1. Results of 1-D planar simulations at various times showing air density (solid curves), debris density (dashed curves), and magnetic field magnitude (dotted curves) normalized to their initial values for $M_D = 16$, $\beta = 1$, $\theta = 90^\circ$.

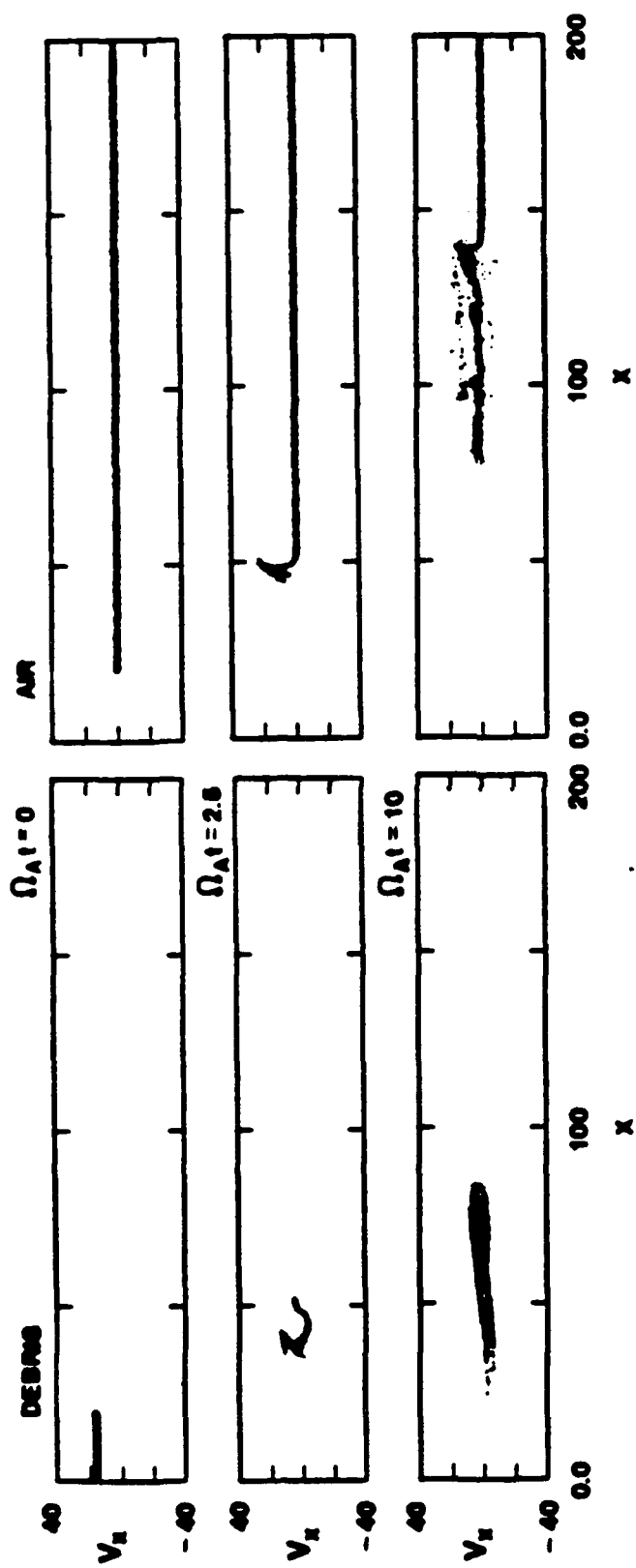


Figure 2.2. Results of same run as Figure 2.1: $v_z - x$ phase space for debris ions (left panels) and air ions (right panels).

times, a fraction of the background ions interacting with the leading pulse are strongly scattered. This ion reflection process generally occurs at supercritical, quasiperpendicular collisionless shocks and has been well described by Leroy *et al.* [1981], Goodrich [1985], and for high Mach number shocks by Quest [1986]. These reflected ions determine the main features of the shock structure and give rise to the harder SHYPS deposition spectrum. The debris, on the other hand, has essentially stopped. Some debris ions still have positive x velocities, but other have been reflected at the front edge of the debris and have been heated.

The process of shock formation and energization of the air ions is, of course, not just restricted to planar calculations. Figures 2.3 and 2.4 show the results of a cylindrical expansion of debris ions into background air, again with an initial Mach number of 16. Figure 2.3 shows the magnetic field (directed out of the plane of the simulation) about the time the debris (initially a dense cylinder expanding radially) has come to rest, with a cylindrical shock expanding outward. In Figure 2.4 radial cuts of B and the background ions in $v_x - x$ and $v_y - x$ phase space at the same time [left panels] show the shock fronts at $x \simeq 10$ and $x \simeq 90$, with corresponding energized background ions. The right panels of Figure 2.4 show the air and debris ions in the x - y plane at the same time. The debris ions have come to rest, while most of the background ions have been swept out by the shock. Outside the shock, the background ions are still undisturbed.

Planar simulations with two spatial dimensions have also been run using the same initial conditions. These calculations show the same ion reflection and energization process as the 1-D simulations and because they include the magnetic field in the plane of the simulation ($\vec{B} = B_0 \hat{y}$), they further show how ions are scattered in the direction of the magnetic field by an electromagnetic instability. These energized air ions can then stream along the magnetic field and be deposited at lower altitudes. As with the first example presented in Figures 2.1 and 2.2, the 2-D example is characterized by $M_D = 16, \beta = 1, \theta = 90^\circ$ with $L_D = 5c/\omega_A$ and $n_D/n_A = 2$. The system size is 200×32 with the cell size $\Delta_x = \Delta_y = 0.5c/\omega_A$. Results at $\Omega_A t = 7.5$ are displayed in the figures. Figure 2.5 shows $v_x - x$ and $v_y - x$ phase space for both debris ions [left panels] and air ions [right panels]. In the air ion phase space one again sees a well formed shock; the reflection process is somewhat less clear because the figure averages over the entire y direction. Most significantly is that heating of the air ions in v_y along the magnetic field is also seen. This effect is due to the Alfvén ion cyclotron instability, as such an effect does not occur in the one-dimensional simulations [Tanaka *et al.*, 1983; Thomas and Brecht, 1986]. The heating occurs behind the shock front, and leads to parallel velocities not much different than those in the perpendicular direction. The debris, on the other hand, shows little parallel heating, which is not surprising, as the Alfvén ion cyclotron instability occurs only near the front of the shock. Profiles in x (averaged over all y) of the normalized debris (dashed line) and air (solid line) [top panel] and magnetic field magnitude [bottom panel] are given in Figure 2.6 at the same time. In this case there is slightly more debris-air mixing with some air ions left behind. The air density and magnetic field show a well formed shock, similar to Figure 2.1.

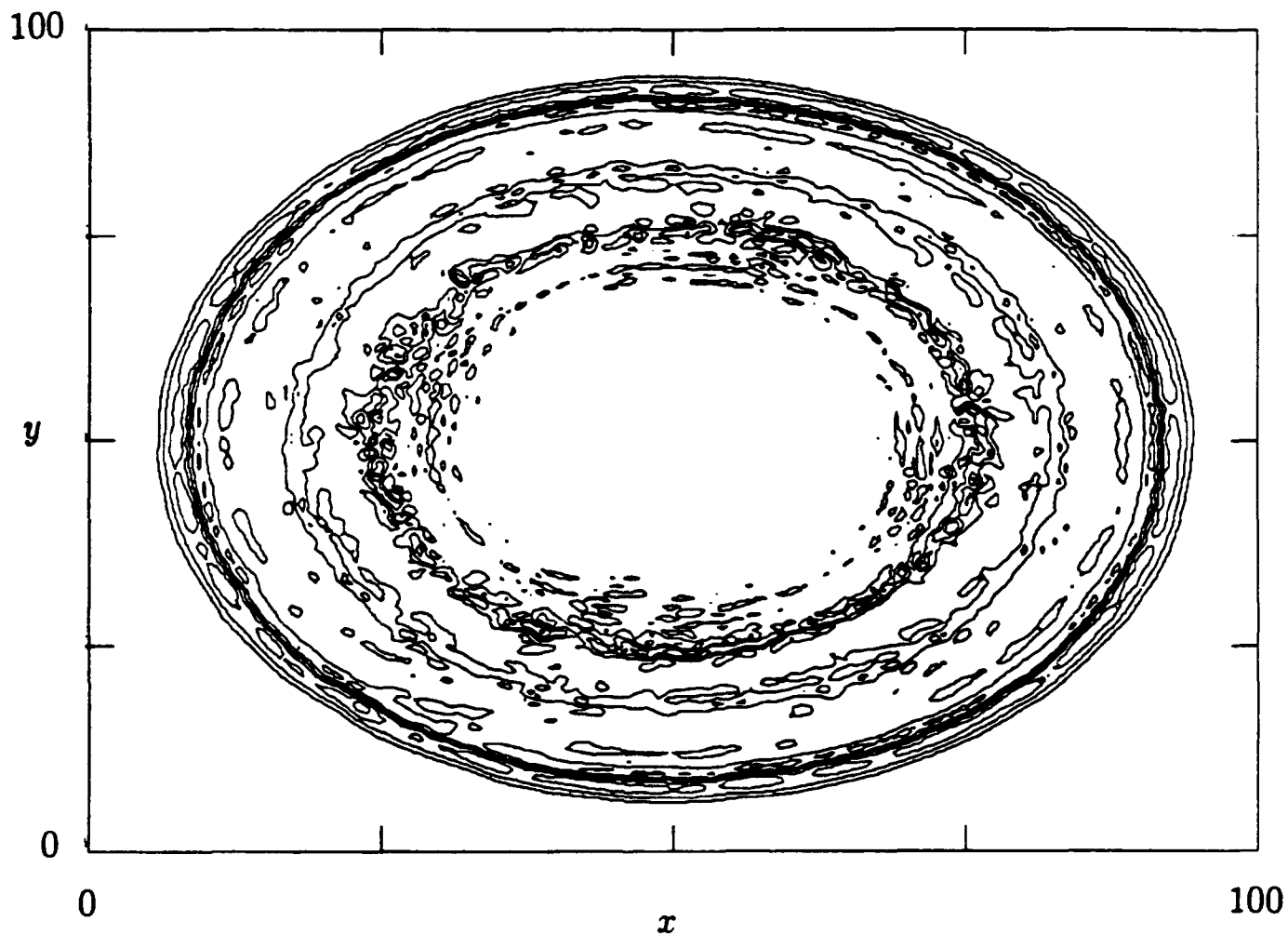


Figure 2.3. Contours of the magnetic field at $\Omega, t = 8$ showing expanding shock generated by debris in a cylindrical calculation, initially expanding from narrow cylinder with $M_D = 16$.

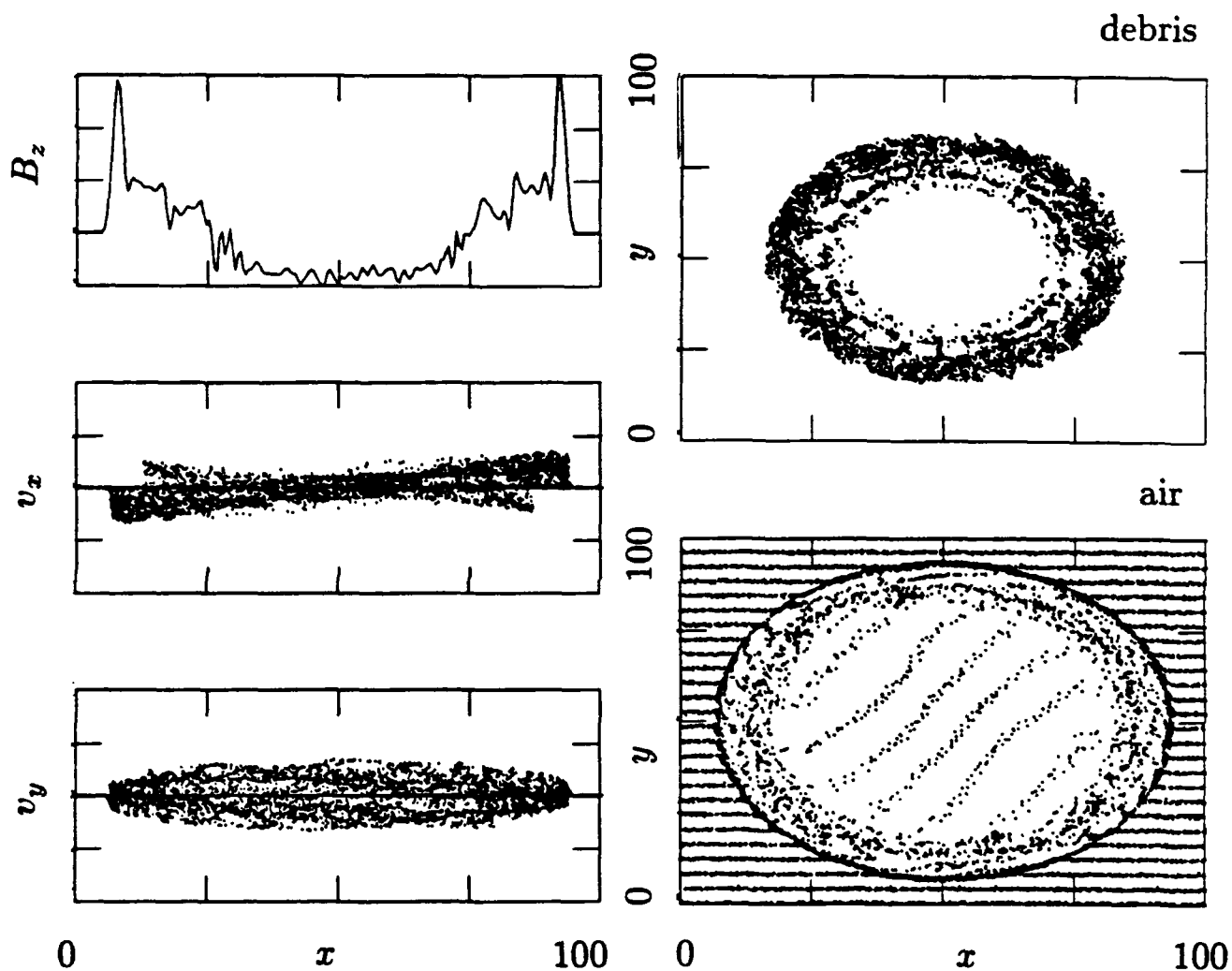


Figure 2.4. [left panels] Cuts through center of simulation region showing magnetic field profile and background ion $v_x - x$ and $v_y - x$ phase space; [right panels] debris and background ions in x - y at the same time of the calculation shown in Figure 2.3.

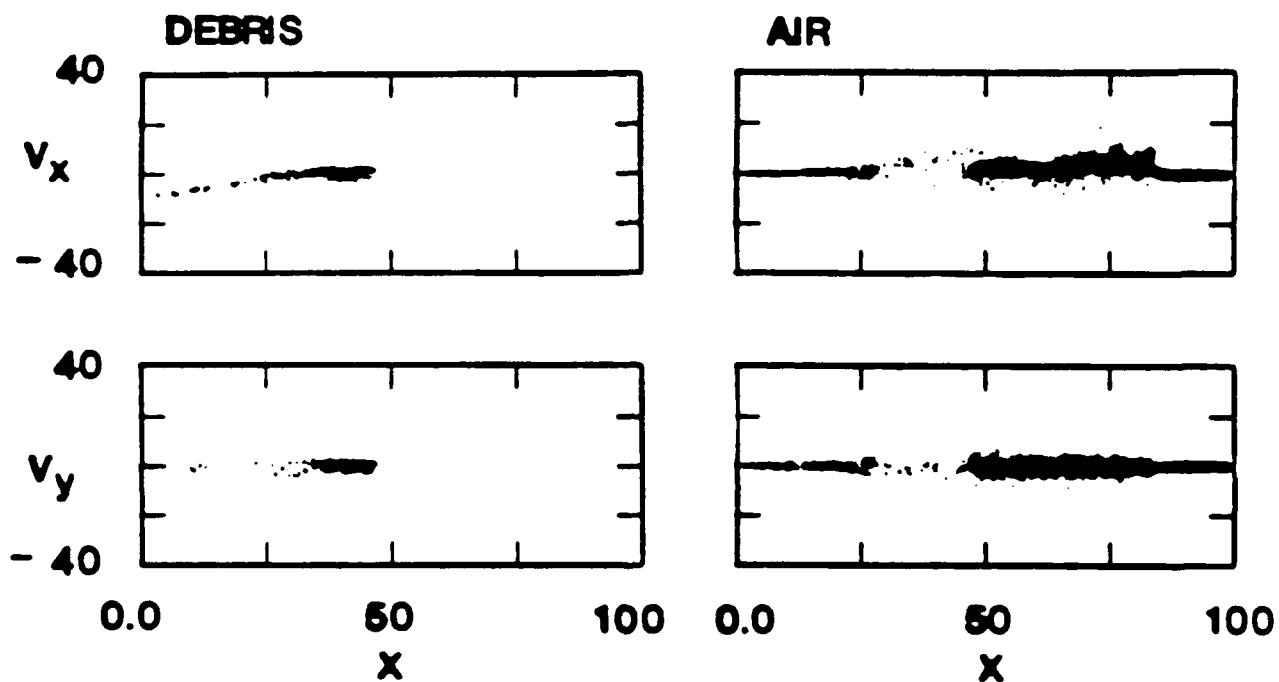


Figure 2.5. Results of a planar 2-D simulation with parameters: $M_D = 16$, $\beta = 1$, $L_D = 10c/\omega_A$, $\theta = 90^\circ$ at $\Omega_A t = 7.5$, showing $v_x - x$ and $v_y - x$ phase space for debris ions (left panels) and air ions (right panels).

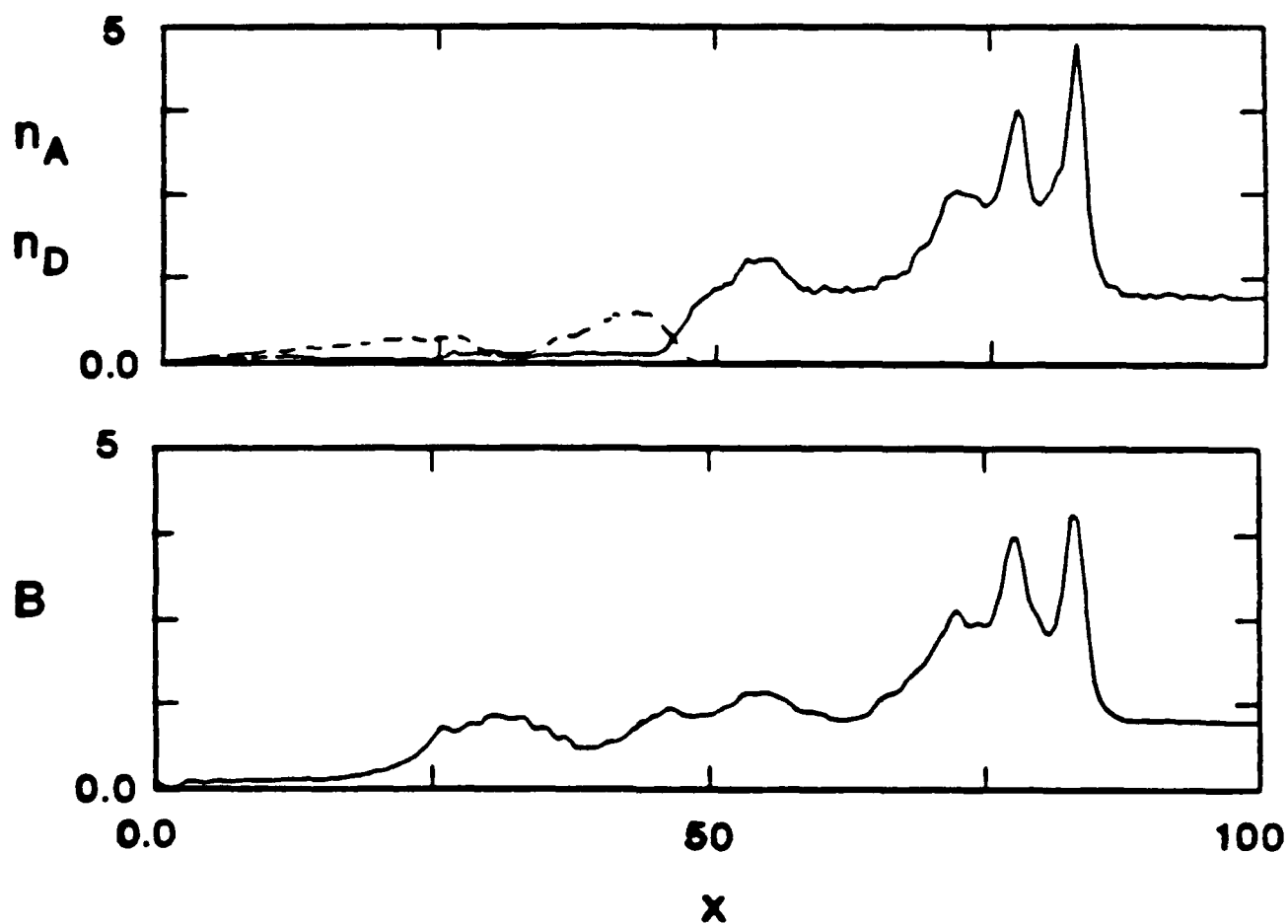


Figure 2.6. Results of same 2-D simulation showing profiles in x (averaged over all y) of [top panel] normalized air density (solid line) and debris density (dashed line) and [bottom panel] magnetic field magnitude.

Contour plots of the debris and air densities are displayed in Figure 2.7. One notes immediately that the shock front is slightly rippled. In addition, the air density shows some well defined wave structure just behind the shock, with a peak density of 11. The contours, which are not labelled, run from 0.0 to 1.6 in steps of 0.1 for the debris and 0.0 to 11.0 in steps of 1.0 for the air. They indicate more clearly the lack of mixing of the two plasmas and the absence of any structure in the debris ions. Corresponding 2-D plots of the magnetic field components B_y and B_z are given in Figure 2.8. Contours for B_y range from 0.0 to 5.0 in steps of 0.5, while those for B_z range from -2.0 to 2.0 with similar increments. While the turbulence in B_y is less evident because of the macroscopic shock profile, the level of fluctuations in B_y is comparable to that in B_z (as well as B_x), with $\delta B/B_0 \sim 2.0$. The primary area of wave activity, as best seen in B_z , is slightly behind the shock front, the region where the reflected ions become isotropized by the Alfvén ion cyclotron instability.

The important new results of the calculation are shown in Figure 2.9. From the 2-D simulation shown in Figures 2.5-2.8 we calculate the parallel velocity spectrum $f(v_{\parallel})$ [top panel] and the related "deposition spectrum" dE/dv_{\parallel} [bottom panel] of the air ions just behind the shock front, as a function of v_{\parallel} at the same time $\Omega_i t = 7.5$. The spectra are normalized to the shock velocity v_s ($\sim 8v_A$). The solid curve in the top panel is the corresponding Maxwellian distribution. At low v_{\parallel} , $f(v_{\parallel})$ is Maxwellian, but deviates significantly at high v_{\parallel} due to the energized reflected ions. Because of the high energy tail, dE/dv_{\parallel} is double peaked (compare with model CMHD, NRL, and BRA spectra shown in Figure 2.10, from Brecht *et al.* [1990]). As is readily seen, the spectrum here agree quantitatively with the SHYPS spectra in two important aspects. First, the spectrum generally has two peaks: one at low energy, due to the thermal ions, and one at higher energy, due to the reflected ions. Secondly, the spectrum extends out to about $2v_s$ (which in this case is about the initial debris velocity). (Had we driven the shock harder, the shock velocity would have been about the debris velocity and the spectrum would then extend to about twice the initial debris velocity, as it does in the SHYPS calculation.) These two features are generic properties of the kinetic aspects of the interaction of the air ions with the shock [e.g., Tanaka *et al.*, 1983] and are not affected much by the limited geometry of the present calculation.

That the spectrum we find agrees with the BRA calculations is not unexpected, as the two simulation codes contain the same physics, even though we have done a planar shock and BRA has carried out a more complete calculation. Also, one should note that our "deposition spectrum" is computed in the source region, not the deposition region. One expects fewer air ions at lower v_{\parallel} to reach the deposition region early in the explosion and hence there will be an absence of ions at small dE/dv_{\parallel} , enhancing the double peaked structure of the spectrum. Also, with our planar shock, the shock does not slow down very much in time, so that our spectrum does not evolve in time as does the BRA spectrum. In a more realistic calculation, as the shock expands, it slows down. At lower Mach number, the number of air ions reflected by the shock front decreases, resulting in a weaker peak at higher energy in the spectrum.

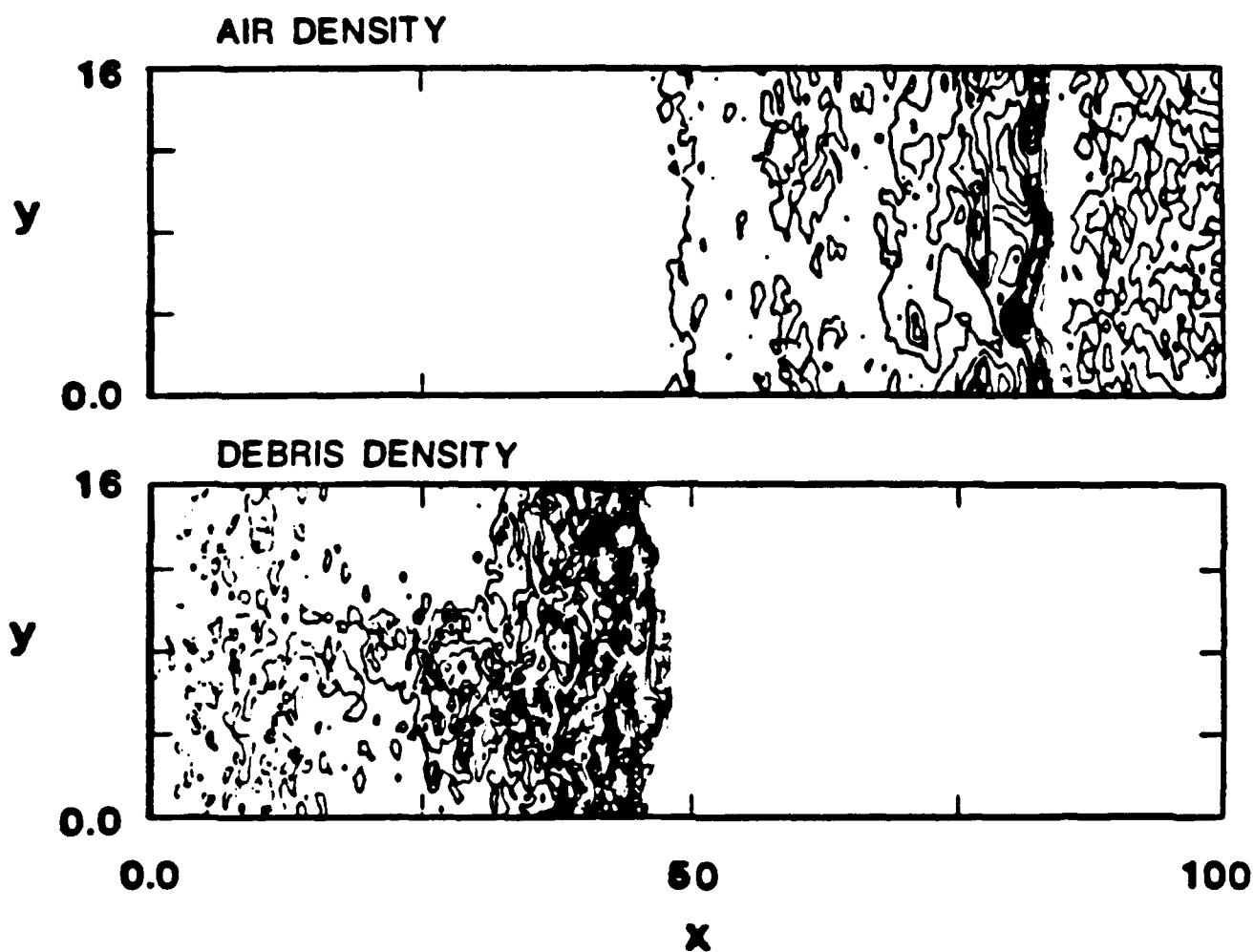


Figure 2.7. Contour plots in x and y of air [top] and debris [bottom] ion densities normalized to their initial values; contours are evenly spaced and vary as 0.0, 0.05, 0.1, ..., 0.6 for debris and 0.0, 0.5, 1.0, ..., 7.0 for air.

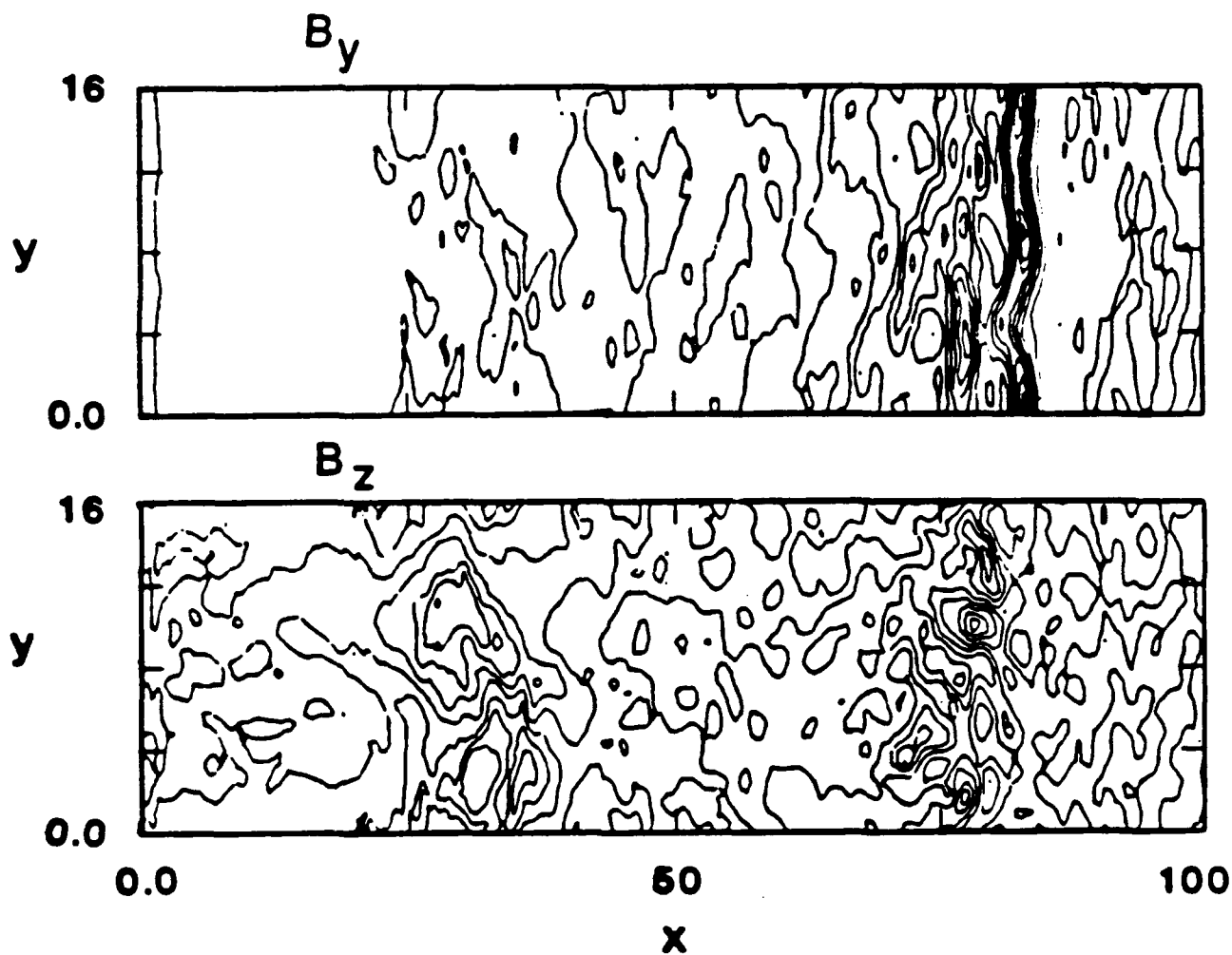


Figure 2.8. Contour plots in x and y of B_y [top] and B_z [bottom] normalized to B_0 ; contours are evenly spaced and vary as 0.0, 0.5, 1.0, ..., 5.0 for B_y and -2.0, -1.5, ..., 2.0 for B_z .

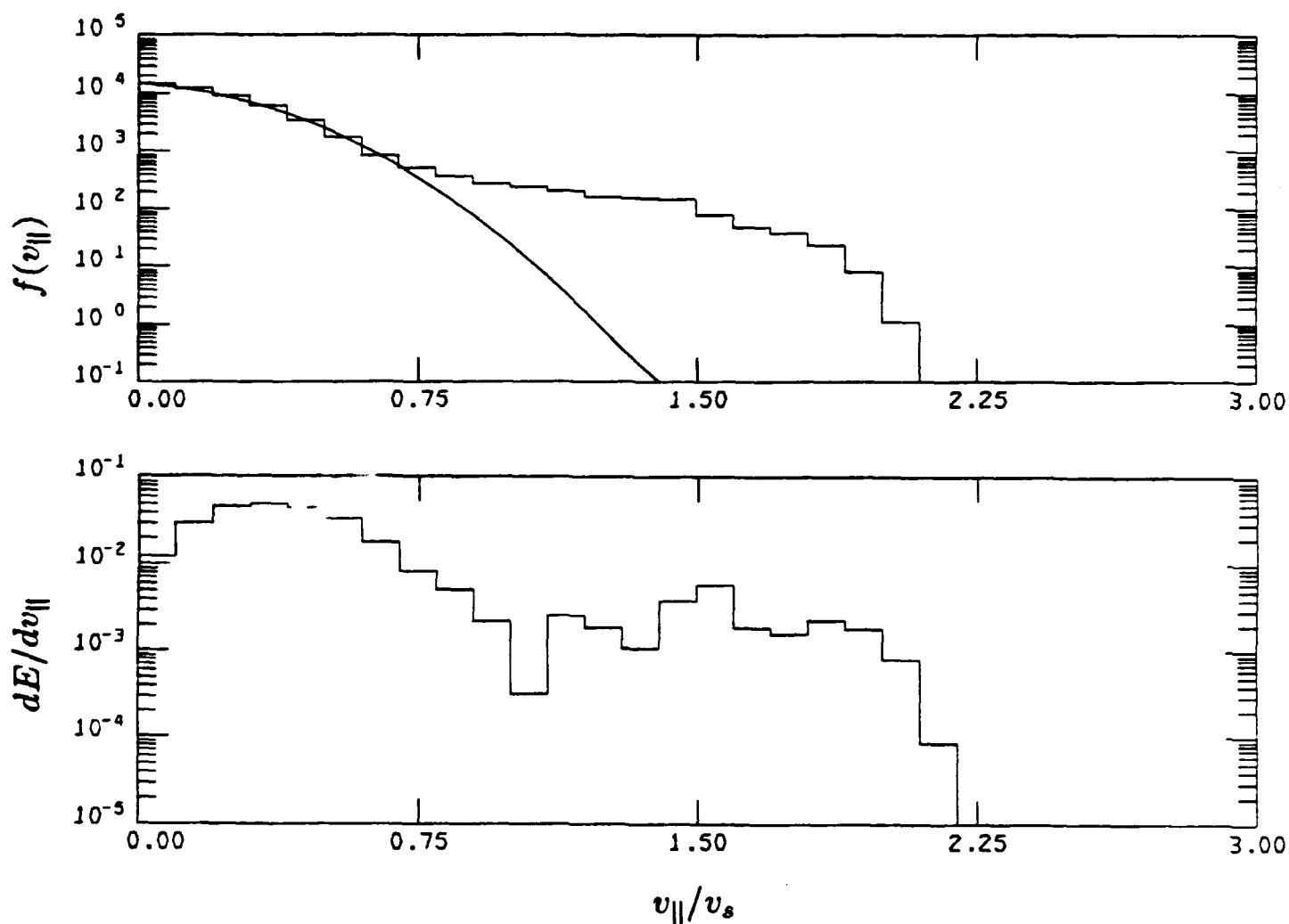


Figure 2.9. [top panel] Parallel velocity spectrum, $f(v_{||})$, for the air ions just behind the shock; [bottom panel] deposition spectrum, $dE/dv_{||}$, at the same time for the simulation in Figures 2.5-2.8. Both spectra are plotted versus $v_{||}$, normalized to the shock speed, v_s .

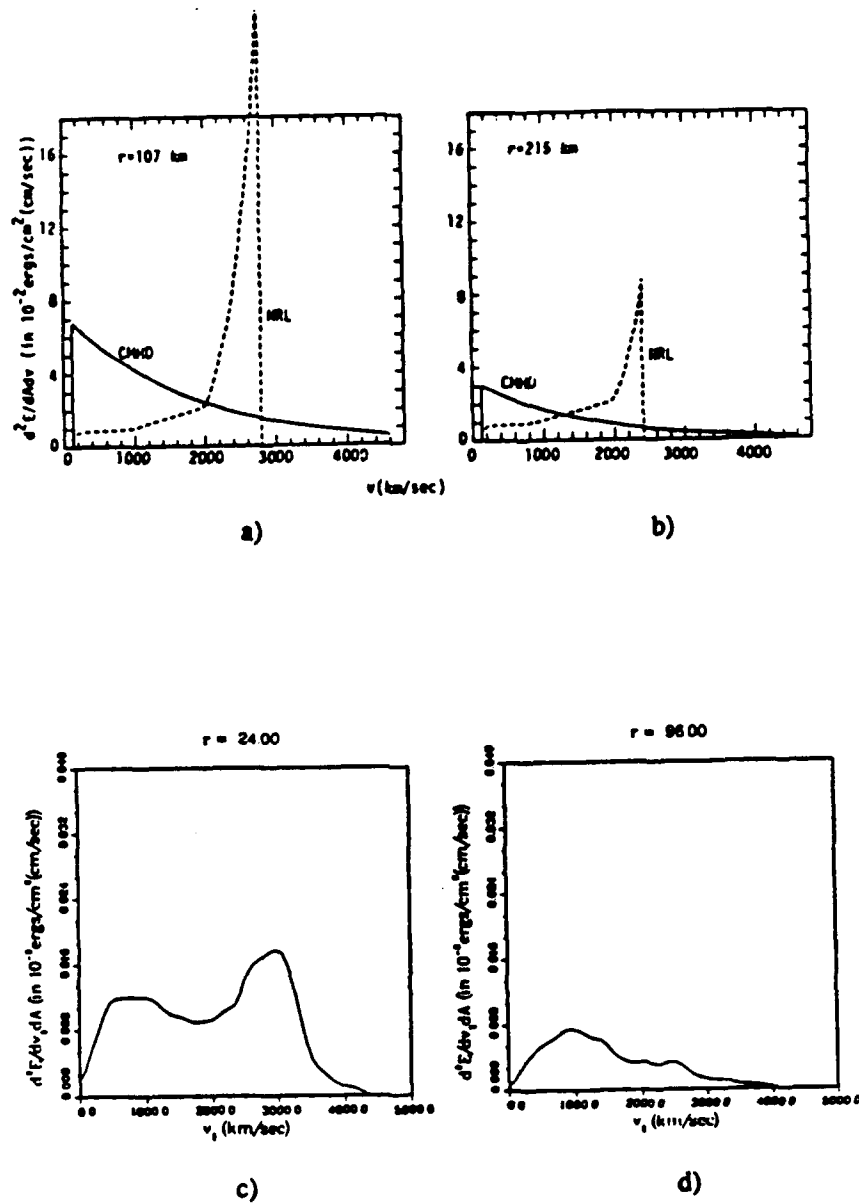


Figure 2.10. Model deposition spectra from CMHD and NRL models and computed spectra from SHYPS [from Brecht *et al.*, 1990].

2.3 Evidence from Space Data

The above picture of a rather hard deposition spectrum resulting from the interaction of an outgoing magnetic shock with background air ions is supported by data from various spacecraft. We briefly show three examples that corroborate the results presented previously. Detailed description of the results and supporting modeling efforts are found in the references.

1. The collisionless shock that results from a high Mach number debris expansion is non-laminar. Unlike a classical MHD shock, the magnetic field profile is characterized by a large "overshoot" at the leading edge of the shock. This overshoot is seen in numerous crossings of the bow shock of the Earth and other planets, especially the outer planets where the Mach number is higher. Figure 2.11 is from Bagenal *et al.* [1987], showing the bow shock of Uranus. The Mach number here is 23. The shock front exhibits a very large overshoot; behind the shock front, the magnetic field reduces to the level expected from the Rankine-Hugoniot relations. These results are also relevant to a recent analysis of the STARFISH magnetic field measurements [Brecht and Thomas, 1988].

2. The interaction of the shock produces two populations of air ions. One population is transmitted through the shock and heated. The other population is reflected and energized. These two populations then give rise to the double peaked nature of the deposition spectrum. Spacecraft observations [Sckopke *et al.*, 1983] show this reflection process and the two distinct populations in great detail [Figure 2.12]. Simulations of this process demonstrate the dynamics quite clearly [Leroy *et al.*, 1981].

3. The subsequent thermalization of the reflected ions and their energization along the magnetic field by the Alfvén ion cyclotron instability produce a highly nonthermal distribution which persists far downstream of the shock (Figure 2.13). Again, the observations of Sckopke *et al.* [1983] show the non-Maxwellian nature of the ion distribution and the persistence of an energized ion component in the downstream region, which is the origin of the harder SHYPS energy spectrum. Simulations confirm both the spectrum shape and the persistence of this effect in the downstream [Winske and Quest, 1988].

2.4 Conclusions

We have used hybrid simulations of high Mach number debris-air ion interactions to verify the essential features of the SHYPS energy deposition spectrum that have been modeled in NORSE calculations by Thompson [1991]. Contrary to the CMHD model, the energy deposition spectra are characterized by two peaks at finite $v_{||}$ and a maximum value of $v_{||}$ that extends to above the initial debris velocity. We have also shown examples of space data that lend additional, independent support to this picture.

While the NORSE calculations are a good start in putting some of the kinetic aspects of debris-air interactions into systems codes and showing that significant differences are possible, we believe that these effects should be pursued in parallel with other modeling efforts enumerated below.

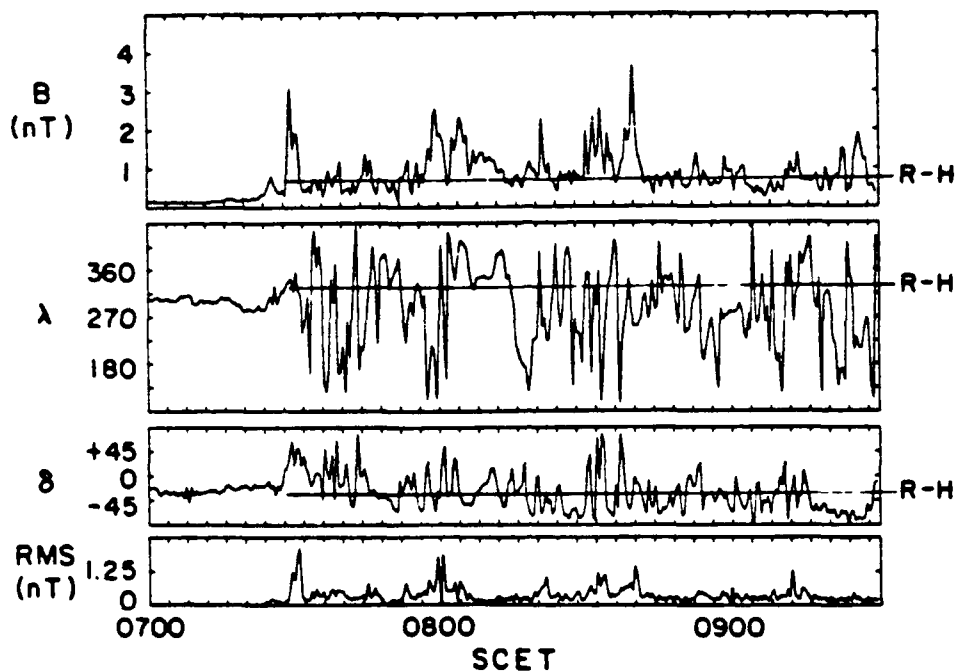


Fig. 5. The 9.2-s averages of the magnetic field magnitude (B), direction (angles λ , δ), and rms in heliographic co-ordinates. The angle λ is defined by $\tan\lambda = B_T/B_R$. The angle δ is defined by $\sin\delta = B_N/B$. The values of the parameters predicted by the Rankine-Hugoniot (R-H) relations are shown by horizontal lines.

Figure 2.11. Profiles of the magnetic field magnitude and other related quantities at the crossing of the Uranus bow shock, showing large overshoot [from Bagenal *et al.*, 1987].

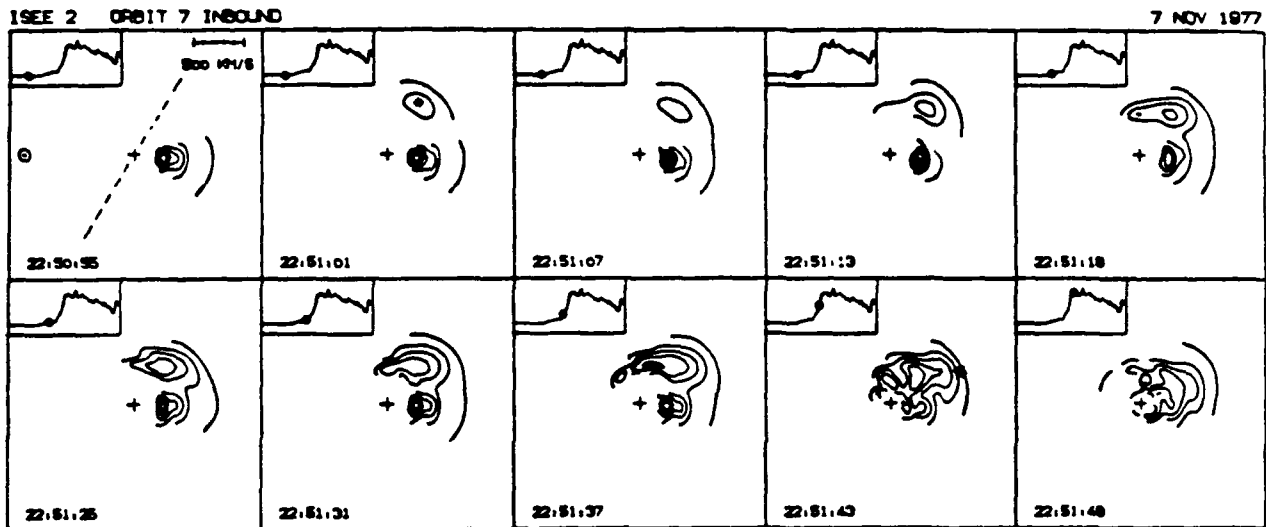


Fig. 2. Ion velocity space distributions for the inbound shock crossing on November 7, 1977, spanning the range from the pure solar wind to the shock ramp. To emphasize the evolution of the distributions, only every other of those measured is shown. The relative positions where the measurements were made are indicated by the dots on the plasma density profiles shown as insets that cover an interval of 2.5 min. The distributions are shown as contours of constant phase space density in two-dimensional velocity space, $f(v, \phi) = \text{const}$, where v is the ion speed and ϕ is the ecliptic azimuth of the velocity vector, with $\phi = 0$ pointing toward the sun on the left. Density levels represented by adjacent contours differ by an order of magnitude. The plus symbols indicate the coordinate origin $v = 0$ in the spacecraft (or, approximately, the shock) frame of reference with the velocity scale given in the first frame. The dashed line in this frame is the projection of a vector parallel to the shock front and perpendicular to the magnetic field, onto the ecliptic plane. The asterisks in frames 2 and 9 indicate the speed and azimuth of specularly reflected ions at their forward turning point and near the shock ramp, respectively.

Figure 2.12. Ion phase space measured at the Earth's bow shock showing two ion populations [from Sckopke *et al.*, 1983].

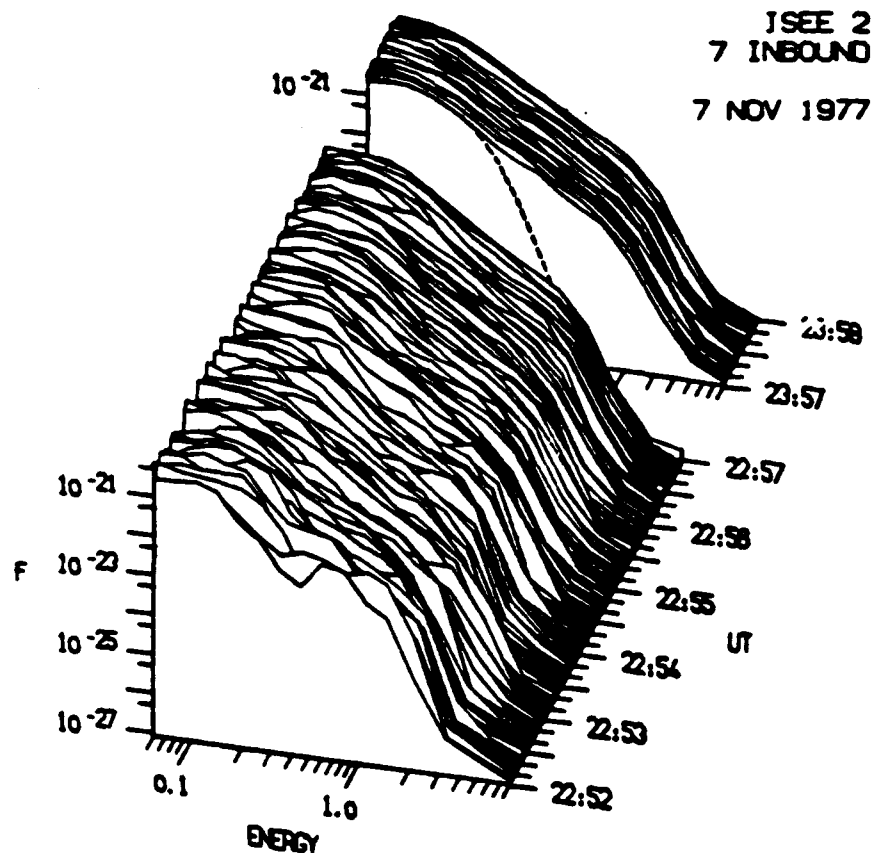


Fig. 15. Time sequence of one-dimensional ion distributions downstream of the November 7, 1977, shock, beginning a few seconds after the shock crossing. The distributions are shown as cuts, $f(E, \Phi = \text{const})$, along the direction Φ of the bulk flow, with $E \propto v^2$ given in keV, and f in units of $\text{cm}^6 \text{s}^{-3}$. Secondary maxima of f due to gyrating ions are present only for a short time, but a broad shoulder of f persists, nearly unchanged, for more than one hour. The dashed curve represents a Maxwellian fit to the low-energy part of the distribution.

Figure 2.13. Ion energy distributions downstream of a bow shock crossing showing persistence of non-Maxwellian, high energy ion component [from Schopke *et al.*, 1983].

1. The use of direct output at discrete times from SHYPS to initialize NORSE has been an expedient way to use the SHYPS data. A more useful format would be analytic expressions for the energy deposition spectra that are derived from the properties of the air-shock interaction. This would then allow a systematic study of kinetic effects on nuclear phenomenology based on the various system codes for a range of burst parameters. This so-called "turning model" could also be used in CMHD to distribute the energy resulting from viscous heating to the air ions.

2. One way to reconcile the differences between the two models might be to try the deposition model of Witt and Kilb [1988] that uses blast wave formulas to calculate shock parameters and the Rankine-Hugoniot relations to distribute the energy. These formulas could be generalized to introduce a population of energetic reflected ions, consistent with the hybrid simulations.

3. One effect that will bring the two models into better agreement is the possibility of further electromagnetic interactions of the energized air ions as they propagate down the field lines. At the debris modeling meeting last fall we showed preliminary calculations of electromagnetic ion/ion instabilities that could slow and thermalize air ions, leading to a softer energy spectrum and deposition at higher altitudes due to such anomalous effects. Some of this work will be presented later in this report.

4. The initial NORSE comparisons using the SHYPS and CMHD spectra contain a number of important differences: (a) total energy deposited, (b) energy spectrum shape, and (c) energy deposited with distance from the burst point. All three of these differences can affect the resulting phenomena in various ways. It would be useful to carry out the systems calculations varying only one effect at a time to see how these processes result in which differences to the phenomenology and how sensitive those differences are to the models.

5. As noted by Thompson [1991], the present NORSE calculations do not include debris energy that remains undeposited, which for the SHYPS calculations can be significant. What is needed is a model for where the debris is and what its energy characteristics are [as has become very apparent at the last two debris modeling meetings], as well as the capability to include such undeposited debris energy in the systems codes.

6. Finally, the study of high Mach number debris air interactions in the collisionless limit using the AGNES facility would be highly desirable. Properly designed experiments could measure the deposition spectra and provide a controllable environment for doing detailed modeling studies.

References

Bagenal, F., J. W. Belcher, E. C. Sittler, and R. P. Lepping, The Uranian bow shock: Voyager 2 inbound observations of a high Mach number shock, *J. Geophys. Res.*, 92, 8603, 1987.

Brecht, S. H., and V. A. Thomas, Contact authors for reference, 1988.

- Brecht, S. H., R. W. Kilb, and D. Winske, Working paper, 1990.
- Clark, R. W., J. Denavit, and K. Papadopoulos, Laminar interactions in high Mach number plasma flows, *Phys. Fluids*, 16, 1097, 1973.
- Goodrich, C. C., Numerical simulations of quasi-perpendicular collisionless shocks, in *Collisionless Shocks in the Heliosphere: Reviews of Current Research*, ed. B. T. Tsurutani and R. G. Stone, p. 153, Amer. Geophysical Union, 1985.
- Goodrich, C. C., K. Papadopoulos, and J. D. Huba, Early time coupling studies using a 1D hybrid code, NRL Memo Report 5553, 1985.
- Kilb, R. W., and D. E. Glen, Contact authors for reference, 1978.
- Leroy, M. M., C. C. Goodrich, D. Winske, C. S. Wu, and K. Papadopoulos, Simulation of a perpendicular bow shock, *Geophys. Res. Lett.*, 8, 1269, 1981.
- Quest, K. B., Simulations of high Mach number collisionless perpendicular shocks in astrophysical plasmas, *Phys. Rev. Lett.*, 54, 1872, 1986.
- Sckopke, N., G. Paschmann, S. J. Bame, J. T. Gosling, and C. T. Russell, Evolution of ion distributions across the nearly perpendicular bow shock: Specularly and non-specularly reflected-gyrating ions, *J. Geophys. Res.*, 88, 6121, 1983.
- Tanaka, M., C. C. Goodrich, D. Winske, and K. Papadopoulos, A source of backstreaming ions in the foreshock region, *J. Geophys. Res.*, 88, 3046, 1983.
- Thomas, V. A. and S. H. Brecht, Two dimensional simulation of high Mach number plasma interactions, *Phys. Fluids*, 29, 2444, 1986.
- Thompson, J. H., Contact author for reference, 1991.
- Winske, D., and K. B. Quest, Hybrid simulations of debris-air interactions: Debris streaming perpendicular to the magnetic field, Los Alamos Report LA-UR-86-4297, 1986.
- Winske, D., and K. B. Quest, Magnetic field and density fluctuations at perpendicular supercritical collisionless shocks, *J. Geophys. Res.*, 93, 9681, 1988.
- Witt, E. F., and R. W. Kilb, Contact authors for reference, 1988.

3. Debris/Air Interactions

3.1 Introduction

The collisionless interaction of energetic debris ions with ionized air ions in HANE bursts remains an important problem. While numerous aspects of this interaction have been studied for more than two decades, improvements in numerical simulation methods and of understanding of the underlying physical processes have led to continuing investigations. Indeed, Thompson's [1991] recent comparisons of the effect of different early time deposition spectra in NORSE calculations on late time characteristics of electron temperature and density indicate significant differences between two early time models and a continued need for refinement of early time calculations. In this section we concentrate on debris characteristics, such as spatial distribution, energy spectra, and interactions with air ions, as obtained from hybrid (particle ion, massless fluid electron) simulations. These calculations are relatively simple, in that they involve only two spatial dimensions and expansion perpendicular to a uniform geomagnetic field. The plan here is to look for scaling relations as a function of initial debris Mach number. Also, the simulations are used to develop new diagnostics to characterize the properties of the debris. Later, we plan to carry out more extensive simulations to test the scaling relations and include additional physics. We will also compare these results with simulation studies of Brecht [unpublished, 1991] and Simonson and Hewett [1991].

3.2 Simulations

Figure 3.1 shows the basic configuration used in the simulations. A debris cloud with a Gaussian density profile [$n_D(r) = n_{D0} \exp(-r^2/a^2)$, $a \sim 2c/\omega_i$] is situated in the center of the simulation domain ($0 \leq x \leq L_x$; $0 \leq y \leq L_y$; with $L_x = L_y = 100c/\omega_i$). The debris ions with mass m_D expand radially with velocity V_D and have a thermal velocity v_{tD} , expressed in terms of an ion beta ($\beta_D = 4\pi n_o m_D v_{tD}^2 / B_o^2$). The debris expands into a uniform background plasma, with density n_o and ion mass m_o . An ambient magnetic field $B_o \hat{z}$ is perpendicular to the simulation plane. With these background parameters we define the ion inertial length, c/ω_i , where c is the speed of light and ω_i is the ion plasma frequency ($= [4\pi n_o e^2 / m_o]^{1/2}$), and the Alfvén speed $v_A = B_o (4\pi n_o m_o)^{-1/2}$. Time is measured in terms of the inverse of the ion cyclotron frequency, $\Omega_i = eB_o / m_o c$. In these calculations we take $m_D = 2m_o$, $\beta_D = 0.01$, while the ratio of n_{D0}/n_o is varied (see Table 3.1).

At the boundary of the simulation the electric field is set equal to zero, as are the normal derivatives of the magnetic field components. This allows electromagnetic (magnetosonic) waves to be partially reflected at the boundaries. An alternative plan would be to let all the waves out of the system, but the boundary conditions that we use have the advantage that the recovery of the magnetic field is modeled, at least for the lower Mach number expansions. As will be seen, in the higher Mach number cases, these boundary conditions give rise to a reflected shock wave. This is not quite appropriate for HANEs, although it is an interesting way to model multi-bursts. To mitigate the reflection effect, the normal velocities of energized background air ions are set equal to zero at the boundary. For our

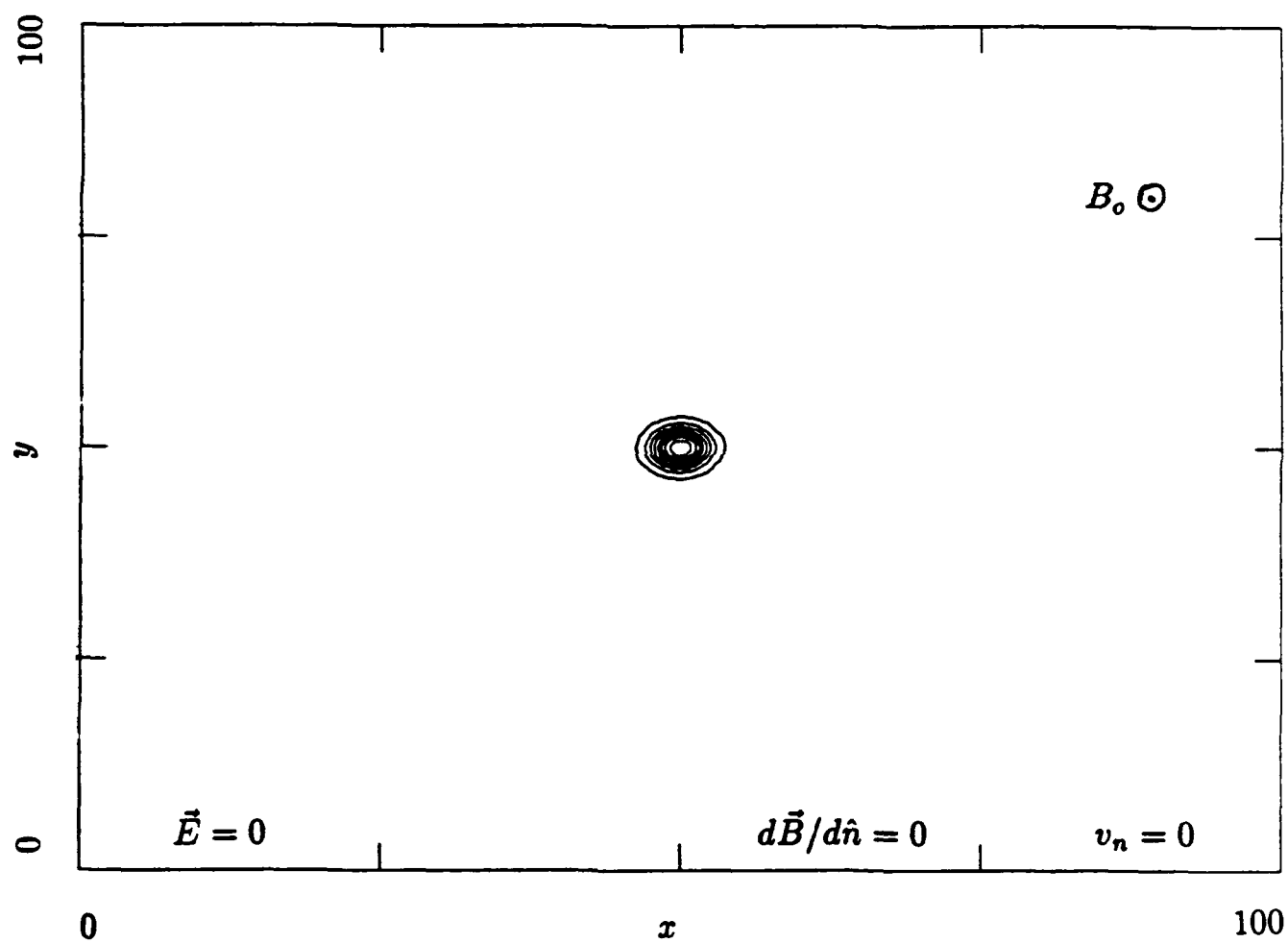


Figure 3.1. Schematic of the simulation domain and the initial configuration.

Table 3.1. Parameters and results of simulations at different debris Mach number.

M_D	0.2	0.4	0.75	1.0	2.0	4.0	8.0
n_{D0}/n_o	512	128	56.9	32	32	32	32
$R_B(c/\omega_i)$	12.8	12.8	16	16	32	64	128
$R_M(c/\omega_i)$	64	32	21.3	16	16	16	16
$E_o/0.5m_ov_A^2$	4	16	56.3	100	400	1600	6400
r_1/r_*	0.43	0.49	0.47	0.47	0.91	1.06	1.05
r_2/r_*	0.37	0.30	0.27	0.30	0.20	0.24	0.92
n_{D1}/n_{D0}	0.13	0.12	0.08	0.07	0.02	0.003	0.005
n_{D2}/n_{D0}	0.006	0.005	0.01	0.005	0.001	0.001	0.003
n_{A1}/n_o	0.55	0.66	0.77	0.60	0.31	0.10	0.035
n_{A2}/n_o	0.98	1.05	0.96	1.13	0.91	1.07	0.90
E_{D1}/E_o	1.65	0.75	0.29	0.18	0.10	0.04	0.15
E_{D2}/E_o	1.32	0.67	0.16	0.14	0.22	0.19	0.02
E_{A1}/E_o	3.67	2.58	1.16	0.48	0.17	0.04	0.01
\bar{E}_{A2}/E_o	0.69	0.25	0.09	0.05	0.05	0.04	0.04

later calculations we plan to do only a quadrant of the present simulations, i.e., put the expanding debris in one corner. We will also use an adjustable grid to allow the shock to move out of the system. How to model the important effect of the recovery of the ambient magnetic field in this case, however, remains unclear at this time. Typically, in these calculations we use 200×200 cells with 160000 background and 160000 debris ions. In this section we show results of three different calculations, with debris Mach number $M_D = V_D/v_A = 8, 0.2, \text{ and } 1$, respectively. Scaling relations obtained from these and other simulations are discussed in the next subsection.

We begin with the $M_D = 8$ case. Representative results are displayed in Figures 3.2-3.7. Figure 3.2 shows contour plots of the total ion density at various times. At $t = 0$ we can see only the debris ions ($n_{D0}/n_0 \approx 32$). As time proceeds, the debris density drops and the outermost contours represent air ions that are beginning to be compressed by the expanding debris. By $\Omega_i t = 4.8$, the outer dark edge represents the front of an expanding shock in the air. By $\Omega_i t = 7.2$ the debris ions, whose density is represented by the innermost, wavy contours, are essentially stopped, while the shock continues to expand and eventually ($\Omega_i t = 12$) reflects from the ends of the system. Corresponding 3-D perspectives of the magnetic field are displayed in Figure 3.3 at comparable times. The high Mach number expansion rapidly compresses the magnetic field, which then expands out as a collisionless shock wave. The region behind the shock remains highly turbulent. Again, complex interactions occur at the boundaries, as the shock arrives and reflects.

Figure 3.4 shows a contour plot of the magnetic field at $\Omega_i t = 6$. The smooth outer contours of the shock region and the more structured contours in the region of the debris are evident. Figure 3.5 displays slices in x of the magnetic field and $v_x - x$ phase space for both the air and debris ions. The magnetic field profiles show the expanding shock with a large overshoot, separating out from the driving piston. The shock has evidently energized the air ions, by the reflection/gyration process discussed in the previous section. By this time ($\Omega_i t = 6$), the debris has stopped. As Table 3.1 shows, the equal mass radius in this case is $12.8c/\omega_i$, but because the ion gyroradius is so large ($\rho_i = V_D/\Omega_i = 8$), the debris actually extends out as far as $R_M + 2\rho_i \sim 30c/\omega_i$. Most of the debris ions have stopped and not thermalized much. Some debris ions, however, are energized during the debris/air interaction.

In Figure 3.6 are displayed 3-D perspective plots of the debris density, the debris energy [$E_D = 0.5m_D(v_x^2 + v_y^2)$], and the air ion energy at later time ($\Omega_i t = 16$) for the same case. All three quantities are characterized by very spiky features that indicate the highly turbulent nature of the interaction. The debris ions, however, remain fairly well contained at about the same radius as they were at earlier times. Again, this is because the present calculations do not model well the recollapse of the ambient magnetic field, i.e., the recollapse is accompanied by the reflected shock wave. The debris energy is also highly structured, with a more energetic debris core and a more highly variable energy in the outer halo region. The air ion energy is also structured, with most of the energization occurring in the outer regions, as expected. In order to show these effects in a more quantitative fashion, narrow slices in y of these same quantities at the same time are plotted as a function of

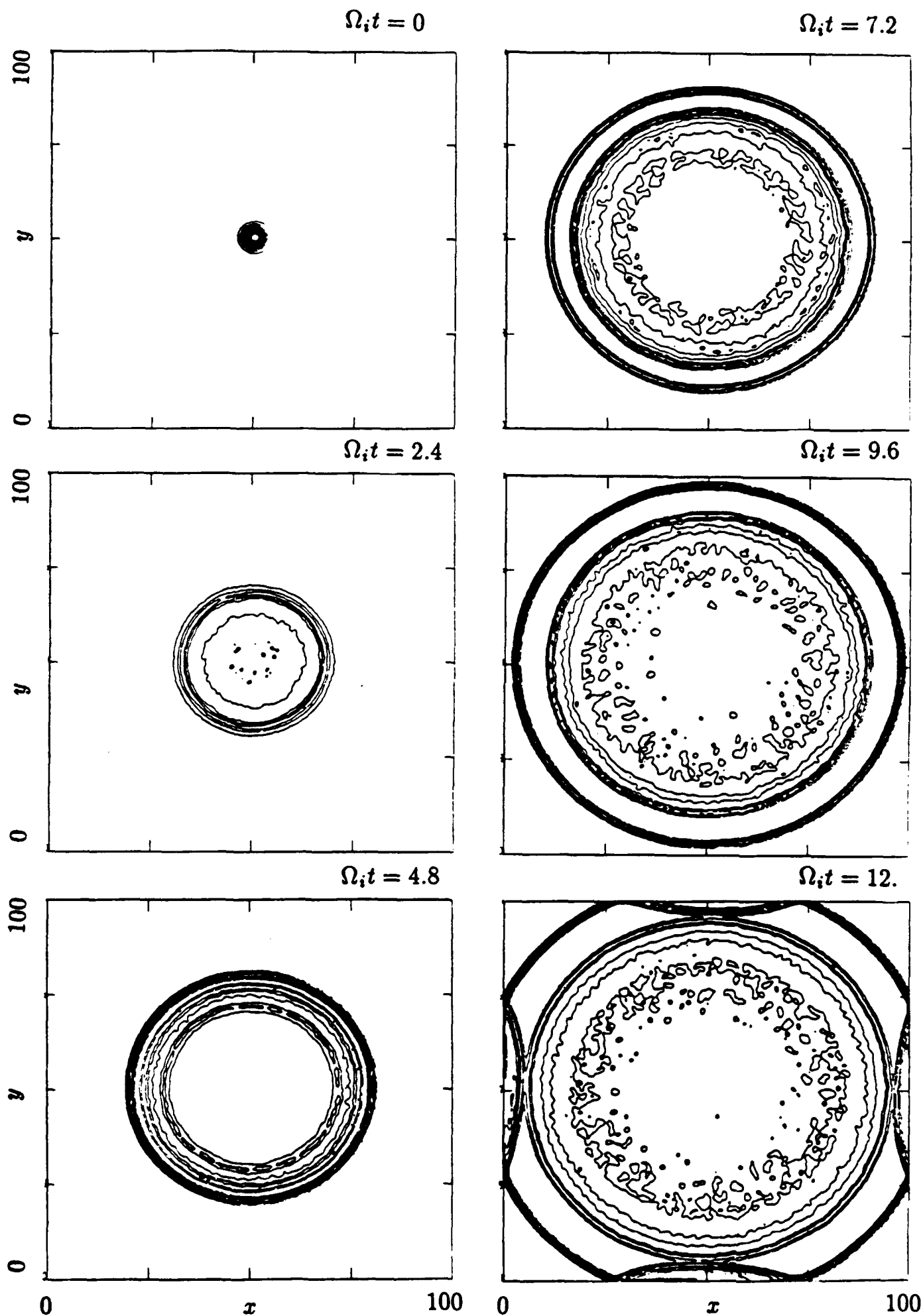
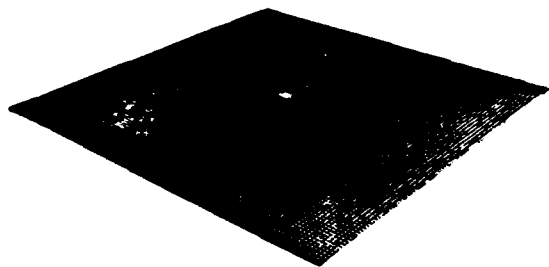
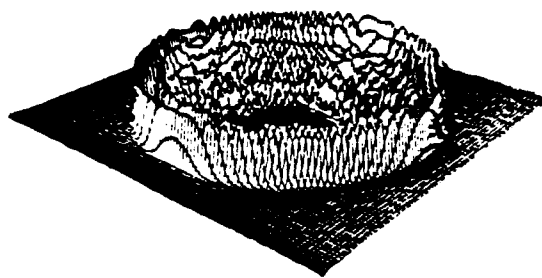


Figure 3.2. 2-D density contours at various times for the $M_n = 8$ run.

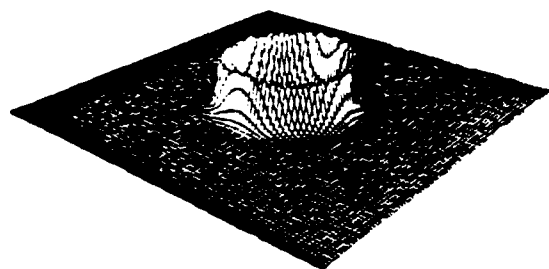
$\Omega_i t = 0$



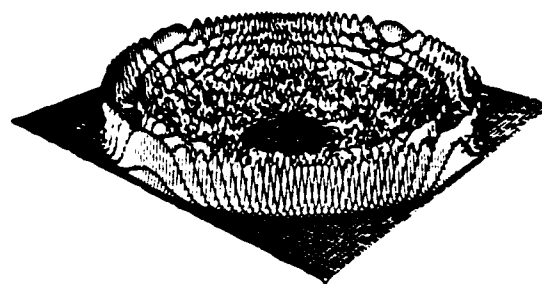
$\Omega_i t = 7.2$



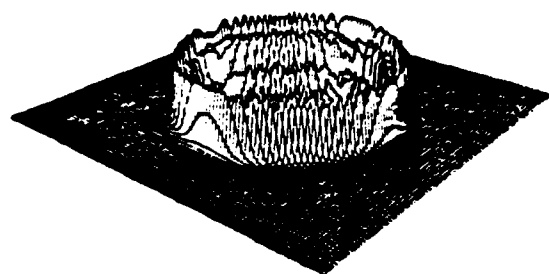
$\Omega_i t = 2.4$



$\Omega_i t = 9.6$



$\Omega_i t = 4.8$



$\Omega_i t = 12.$

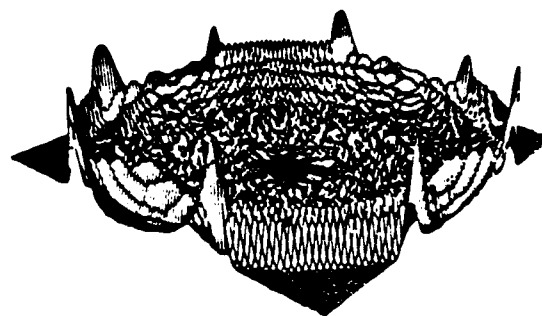


Figure 3.3. 3-D perspectives of the magnetic field at the same time for the same run.

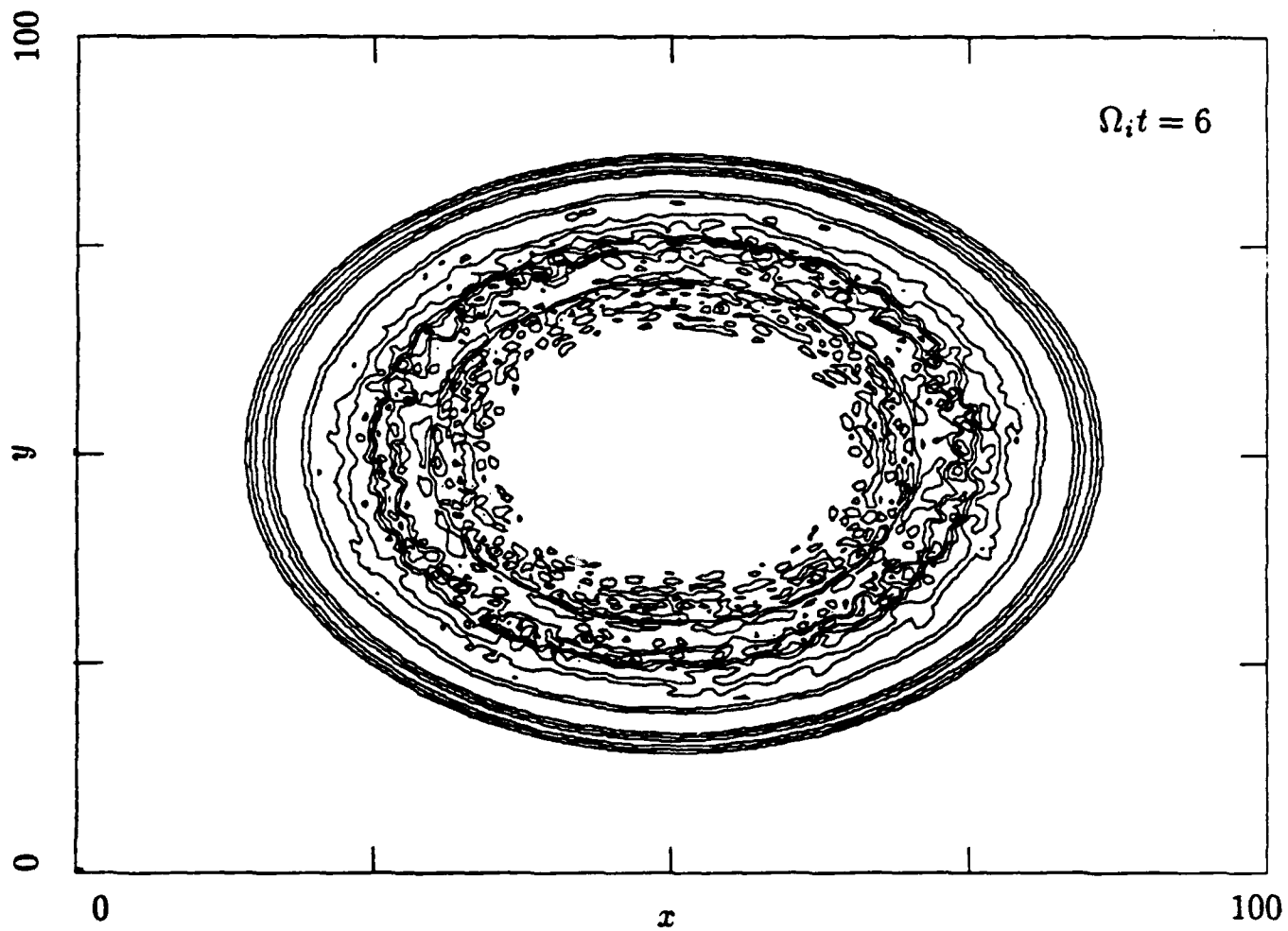


Figure 3.4. 2-D contour plot of the magnetic field at $\Omega_i t = 6$ for the same run.

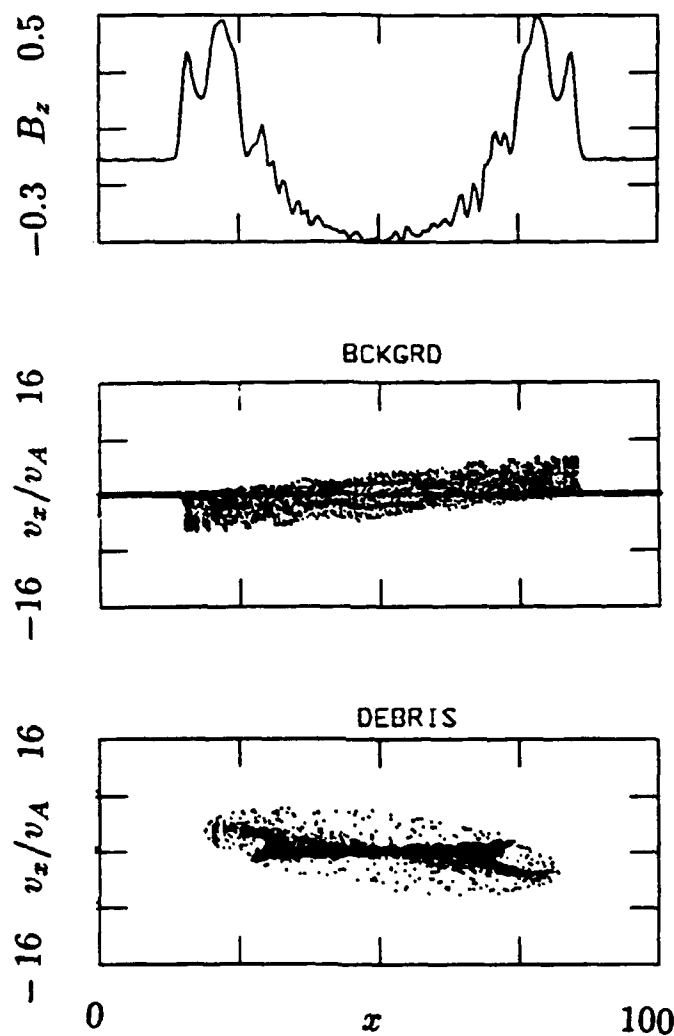


Figure 3.5. Slices in x of B_z and $v_z - x$ phase space for the air and debris ions at the same time as in the previous figure.

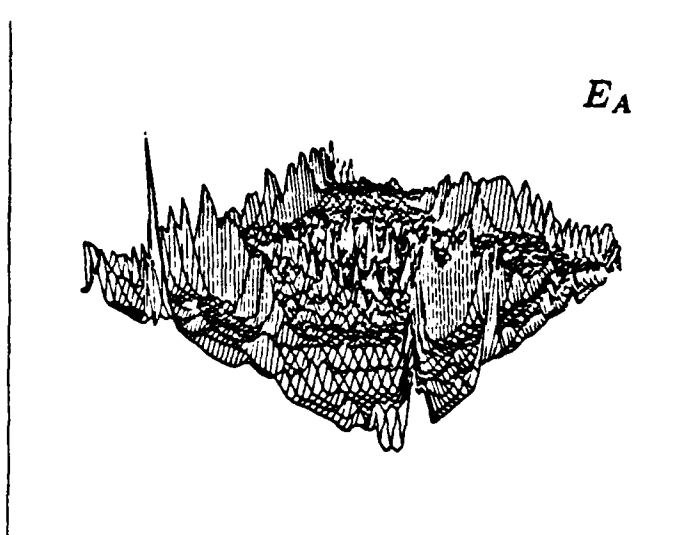
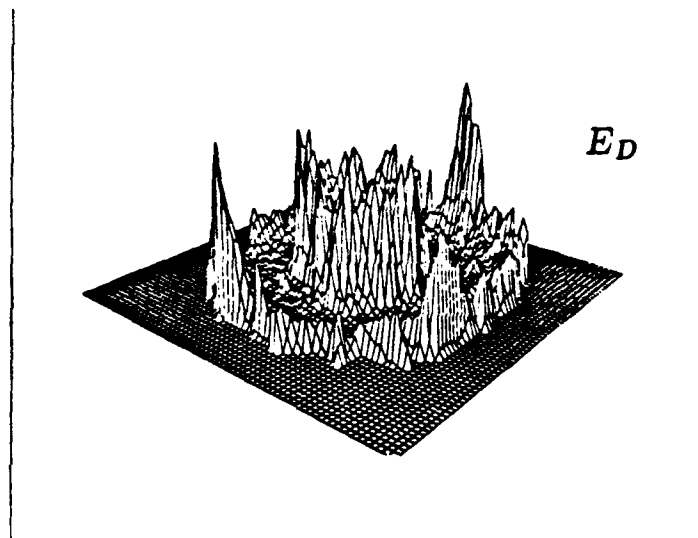
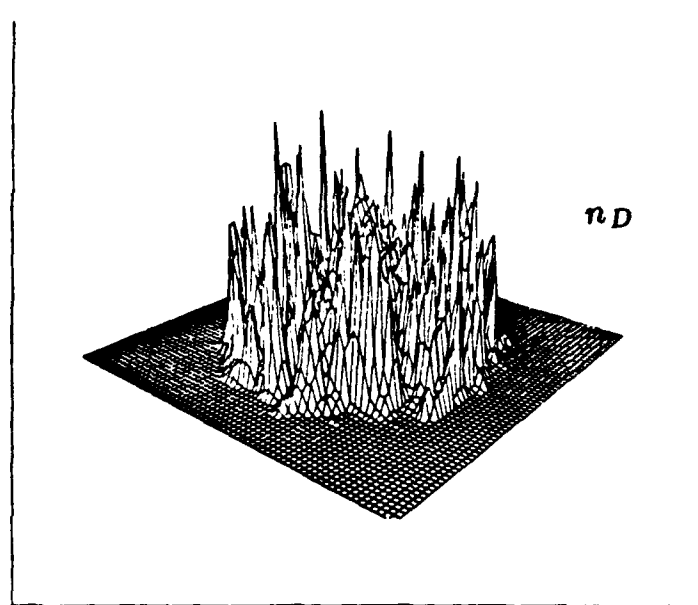


Figure 3.6. 3-D perspectives of the debris density, debris energy, and air ion energy at $\Omega_i t = 16$ for the same run.

x in Figure 3.7. The spiky nature of the debris ion density (normalized in terms of the peak debris density) is especially evident in the outer regions. Near $x = 0$ the density remains small; better collapse of the magnetic field would tend to compress the density, giving rise to a more expected monotonic falloff. A fraction of the density remains in a low density halo. The second panel in Figure 3.7 shows the debris energy, normalized to the initial debris kinetic energy. As with the density, the debris energy profile can be subdivided into an inner energetic core at $r < r_1$ and an outer halo of less energetic debris ions ($r_1 < r < r_2$). The corresponding air ion energy is plotted in the bottom panel. The inner region is essentially devoid of air ions. Air ions outside of this region have been energized to a significant fraction of the initial kinetic energy by the shock.

In contrast, we plot in Figures 3.8-3.11 corresponding quantities from a low Mach number expansion at $M_D = 0.2$. Because similar low Mach number cases have been discussed previously in Section 1 in relation to VHANE bursts, we limit the discussion here to a few plots to compare with the $M_D = 8$ case. In Figure 3.8 is displayed a contour plot of B_z at $\Omega_i t = 24$. (Note that this calculation is done in a $64 \times 64 c/\omega_i$ system with correspondingly fewer cells and macroparticles.) The plot shows the formation of a magnetic cavity with weak magnetosonic waves propagating outward. A profile of the magnetic field for this case is shown in the top panel of Figure 3.9. The cavity and the weak magnetic compression ahead of the cavity are clearly seen. The bottom panels show $v_x - x$ phase space for the air and debris ions at the same time. The cavity formation has led to some slight heating of the air ions at the edge of the cavity. The debris ions are still expanding at this time ($\Omega_i t = 24$). With the magnetic confinement radius in this case, $R_B = 12.8c/\omega_i$, the debris continues to expand until $\Omega_i t \sim 60$.

Three dimensional perspectives of the debris density, debris energy, and air ion energy are shown in Figure 3.10 at a much later time, $\Omega_i t = 160$, when the debris has collapsed with the magnetic field. The debris remains well confined in this case, although the energy of the debris is quite variable. Unlike the high M_D case, here the air ions that become strongly energized are those that collapse with the debris. The air ions outside the main cloud, which interact with weak magnetosonic disturbances, are not heated very much. These results are reenforced in Figure 3.11, which show corresponding cuts of these distributions along x . The debris is well contained within a radius r_1 ; a small fraction resides in a narrow halo region, $r_1 < r < r_2$. Air ions in the core region are strongly heated. Less air heating occurs in the halo region, even less so at larger radii.

Finally, in Figures 3.12-3.17 we show results from an intermediate case, with $M_D = 1$. Figure 3.12, like Figures 3.4 and 3.8, shows a 2-D contour plot of B_z at $\Omega_i t = 32$. The inner contours correspond to the location of the diamagnetic cavity, while the outer contour is the edge of a weak expanding shock. Figure 13 shows the corresponding density contours. The inner contours represent the debris, which has essentially stopped at this time, compressed into a thin shell, and structured. The outer contours are air ions behind the shock front. Figure 3.14 (again like Figures 3.5 and 3.9) show profiles of the magnetic field (again the cavity and shock are clearly seen) and $v_x - x$ phase space for the air and debris ions.

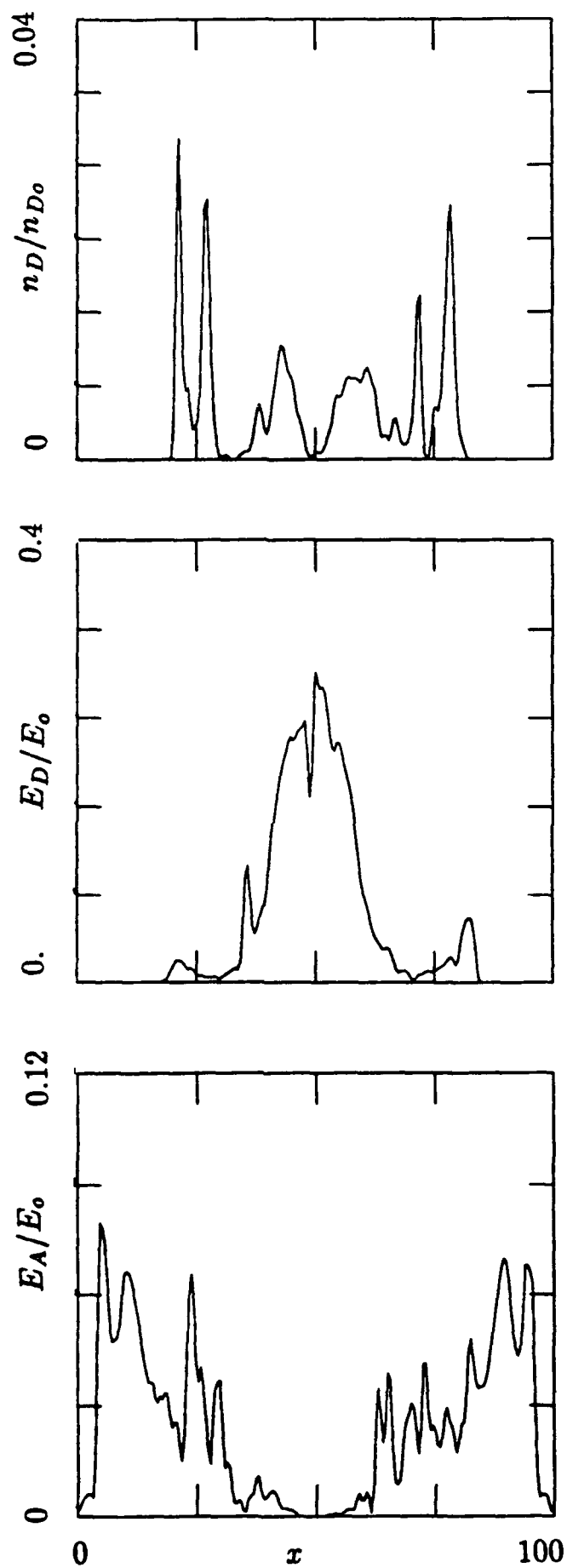


Figure 3.7. Slices in x of the debris density, debris energy, and air ion energy at the same time as in the previous figure.

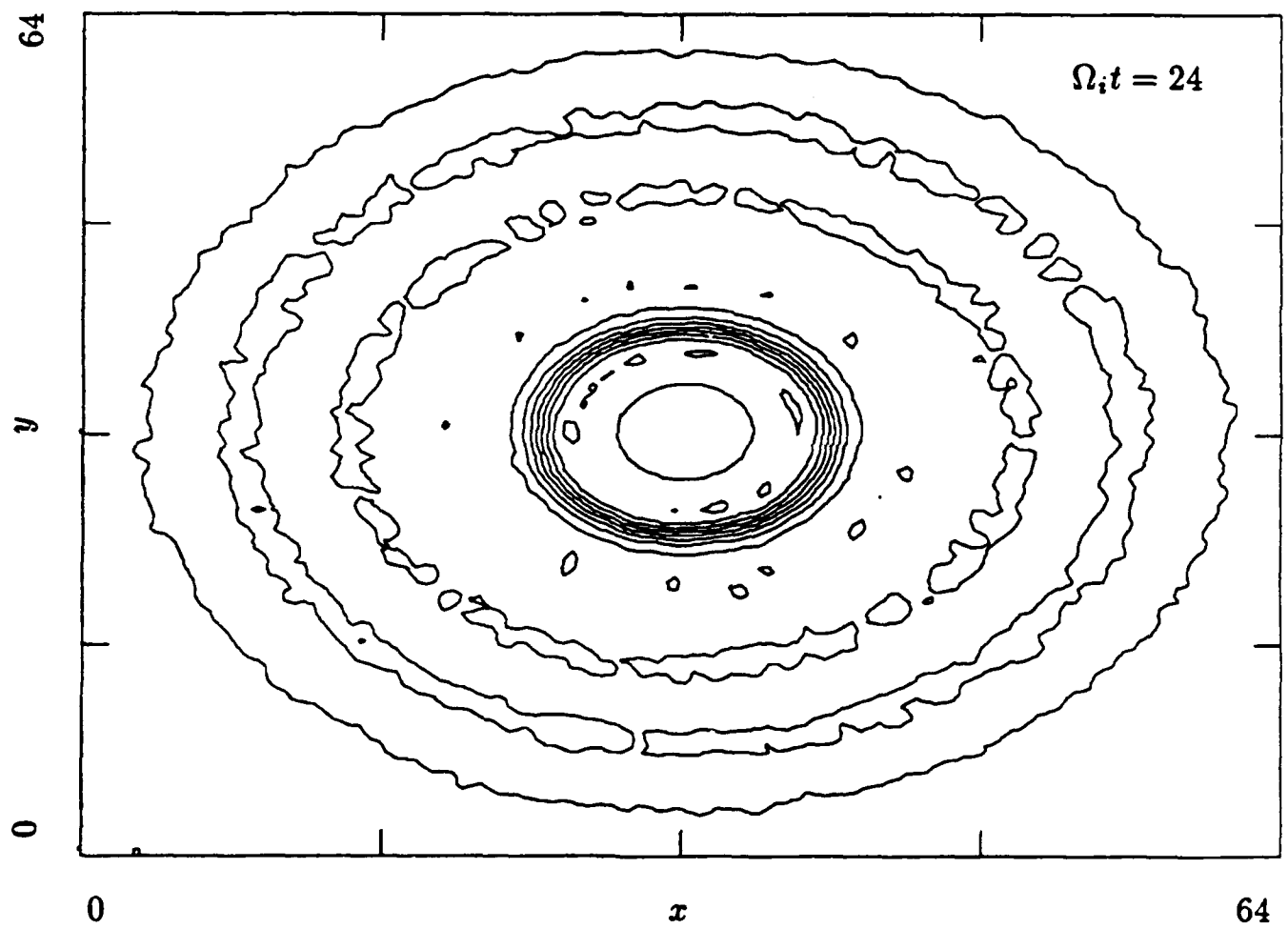


Figure 3.8. 2-D contour plot of the magnetic field at $\Omega_i t = 24$ for the $M_D = 0.2$ run.

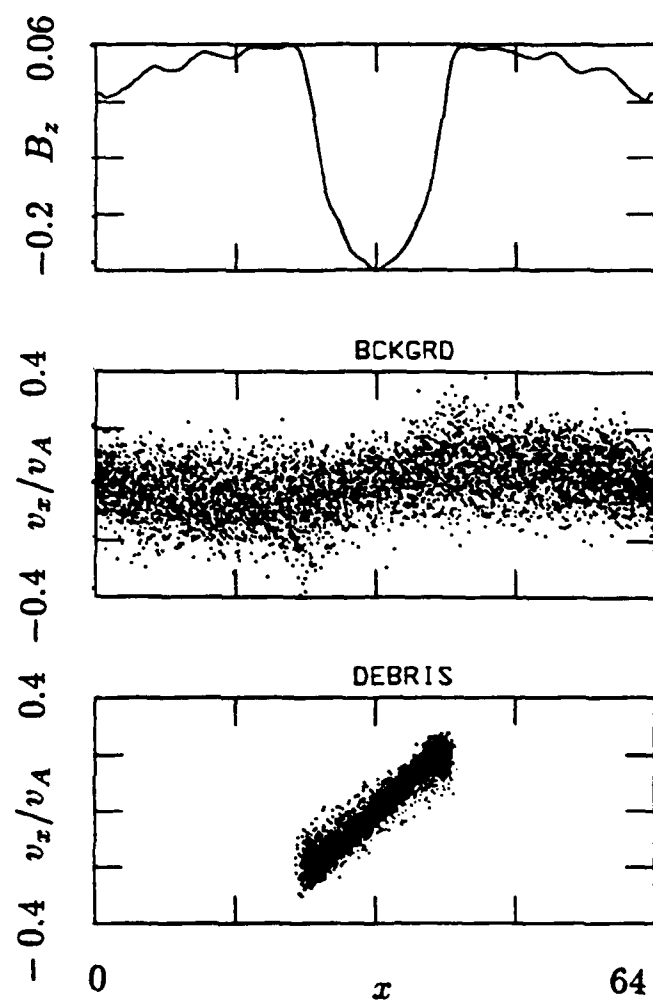


Figure 3.9. Slices in x of B_z and $v_x - x$ phase space for the air and debris ions at the same time as in the previous figure.

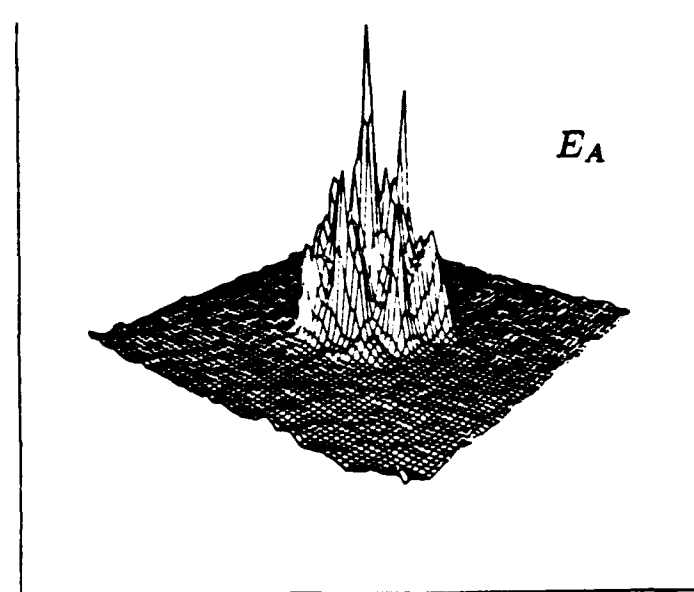
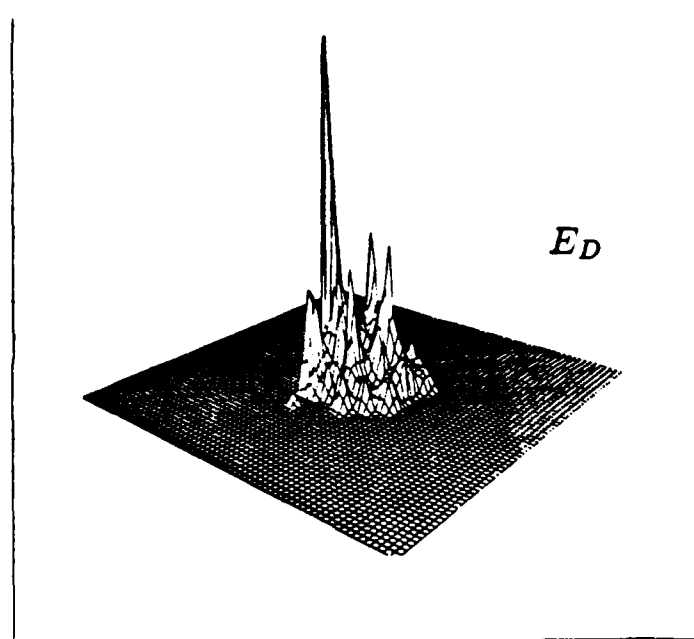
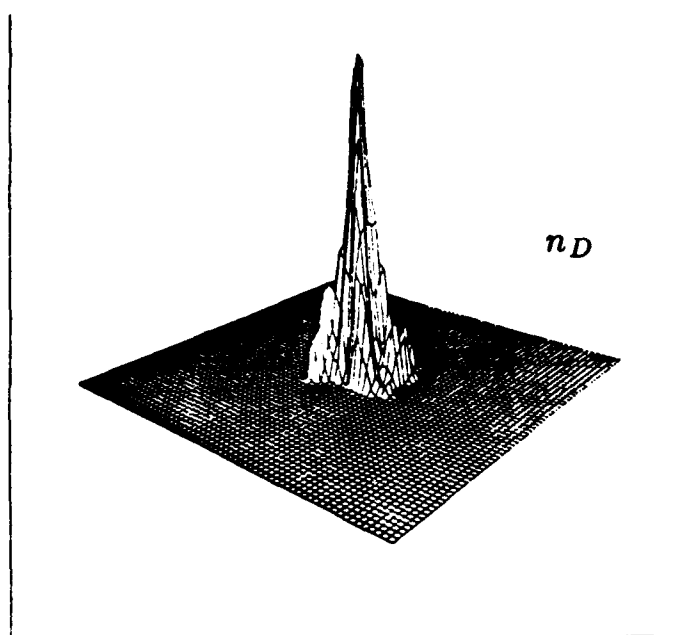


Figure 3.10. 3-D perspectives of the debris density, debris energy, and air ion energy at $\Omega_i t = 160$ for the same run.

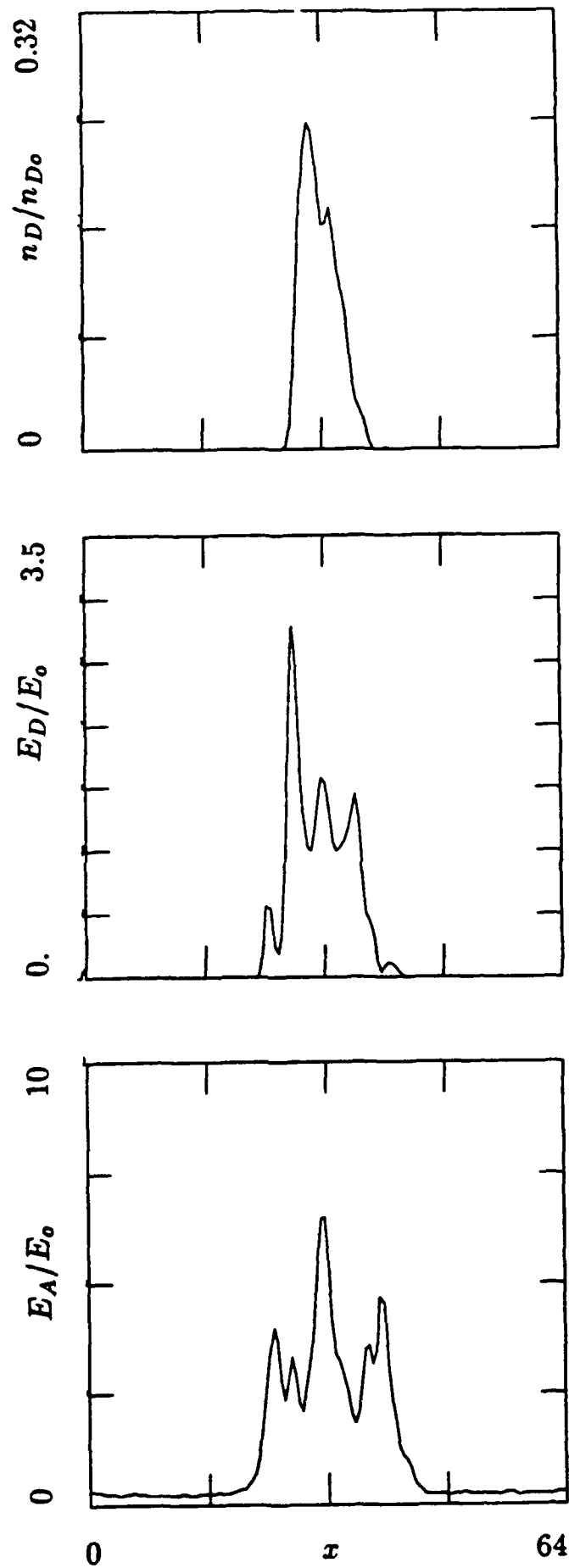


Figure 3.11. Slices in x of the debris density, debris energy, and air ion energy at the same time as in the previous figure.

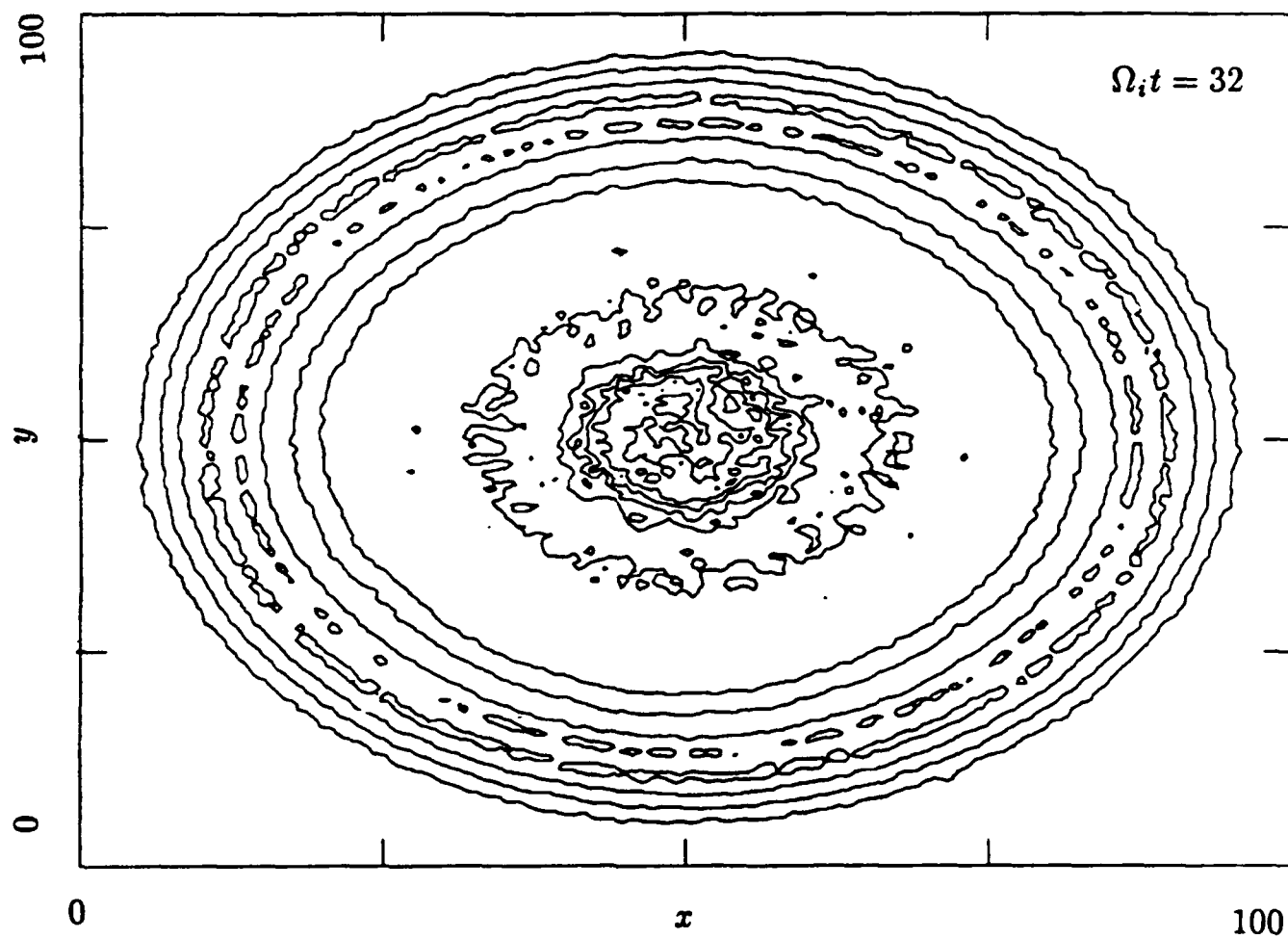


Figure 3.12. 2-D contour plot of the magnetic field at $\Omega_i t = 32$ for the $M_D = 1.0$ run.

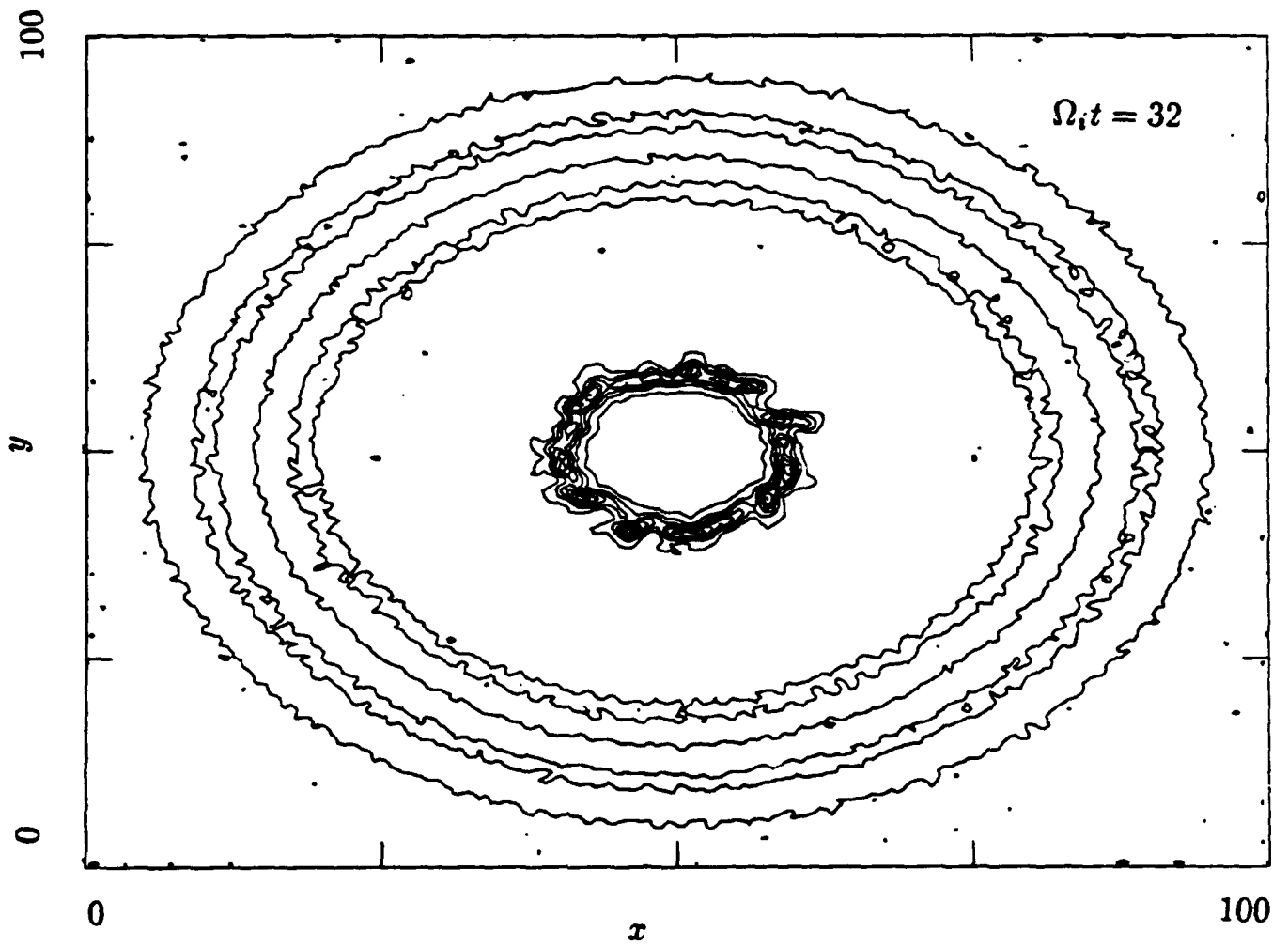


Figure 3.13. 2-D contour plot of the ion density at the same time.

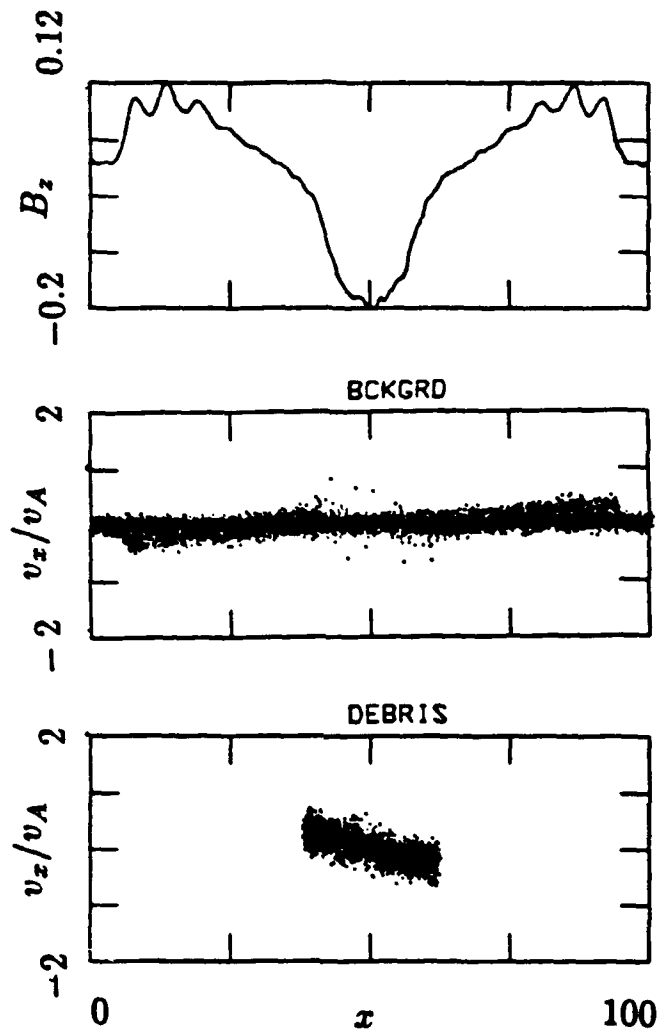


Figure 3.14. Slices in x of B_z and $v_z - x$ phase space for the air and debris ions at the same time as in the previous figure.

The air ions are weakly heated behind the shock. The debris ions have actually begun to collapse ($v_x < 0$ at the right edge of the cloud) with the magnetic field at this time.

Three dimensional perspectives and radial slices of the debris density, debris energy, and air energy are displayed in Figures 3.15-3.16. Like Figures 3.10-3.11 for the $M_D = 0.2$ case, the debris remains well confined and the air ions trapped in the cloud are strongly energized. Like Figures 3.6-3.7 for the $M_D = 8$ case, air ions outside the main debris cloud have been heated by the shock. And overall, there are large fluctuations of each quantity in the cloud.

In Figure 17 are plotted energy distributions for the debris ions for the same $M_D = 1$ case at various times. Initially, the debris energy peaks around E_o with some thermal spread. As the debris expands and stops, the spectrum becomes peaked at $E \sim 0$ and is fairly cold. As the magnetic field recovers ($\Omega_i t = 48$), the debris ions are heated. Eventually ($\Omega_i t = 120$), the spectrum consists of dense, moderately hot component and a more energetic tail, extending out to $E \sim 3E_o$.

Figure 3.18 displays debris ions at the end of the simulations for the three cases we have discussed in detail: $M_D = 0.2$, 1, and 8 as well as for $M_D = 2$. The $M_D = 0.2$ and 1 cases show the debris has collapsed to a relatively small, highly structured cloud. The $M_D = 2$ case also exhibits structure, but the debris ions lie in a ring distribution. If run longer, the debris will slowly collapse further. In the $M_D = 8$ case a small central component of the debris has collapsed, but much of the debris remains out at its point of maximum extent and is highly structured. In this case, however, the ambient field does not recover well, so that the final debris size is not resolved. The larger spatial extent of the debris in this case is probably also due to the large ion gyroradius ($\rho_i = M_D c / \omega_i$).

3.3 Scaling Relations

In addition to the three cases discussed above, we have carried out additional simulations of the same type, varying only the debris Mach number. The results of these simulations are summarized in Table 3.1. For each case we give the initial debris Mach number, debris density (n_{D0}/n_o), debris energy ($E_o/0.5m_o v_A^2$), the magnetic confinement radius R_B , and equal mass radius R_M . At the end of the run, when the debris has collapsed, we calculate, as in Figures 3.7, 3.11, and 3.16, a cloud radius r_1 and a halo radius r_2 , normalized to the smaller of R_M or R_B , the debris and air density and energy inside the cloud (n_{D1} , n_{A1} , E_{D1} , E_{A1}) and in the halo (n_{D2} , n_{A2} , E_{D2} , E_{A2}), normalized to n_{D0} , n_o and E_o . As in Section 1 of this report, r_1 is defined to be the radial position where the density drops to 20% of its peak value; r_2 is the maximum radial extent of the debris. Again, as in Figure 3.7 and 3.18 indicate, at higher M_D the debris does not fully collapse, so the final size of the debris cloud may be overestimated and the energy in the debris may be underestimated.

Nevertheless, some interesting conclusions can be drawn from the results in the table, which have been plotted in Figures 3.19-3.20. The debris radii, r_1 and r_2 normalized by

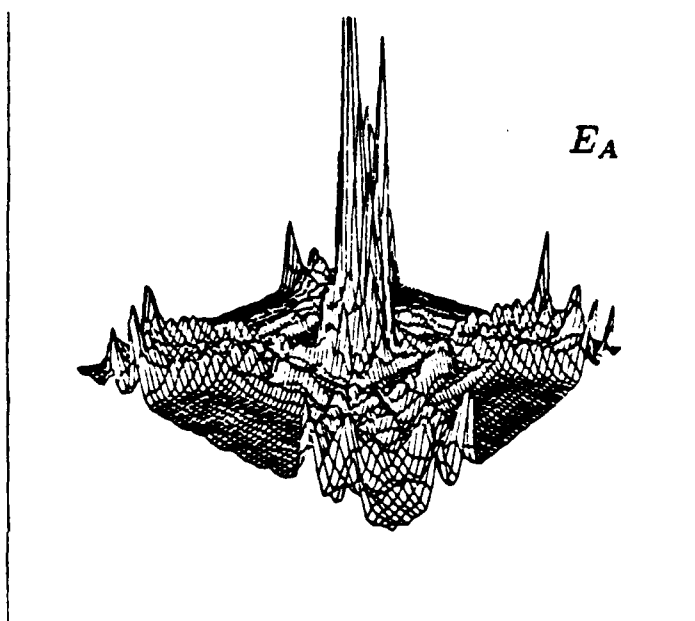
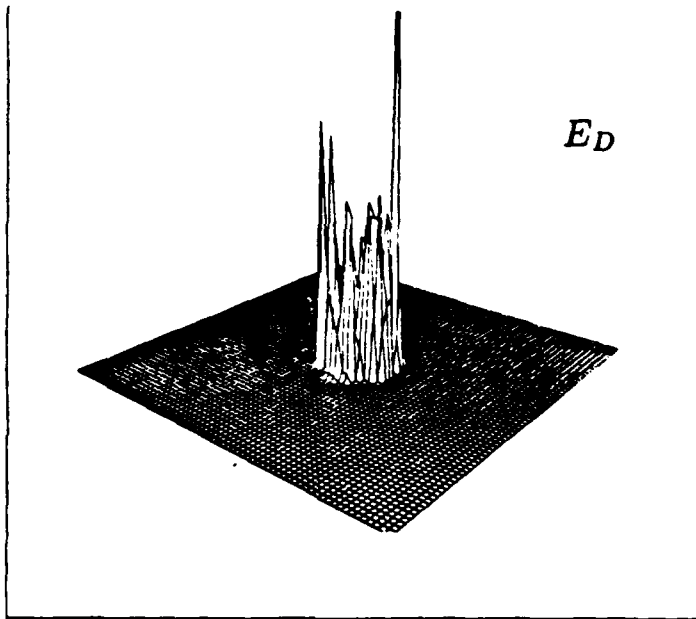
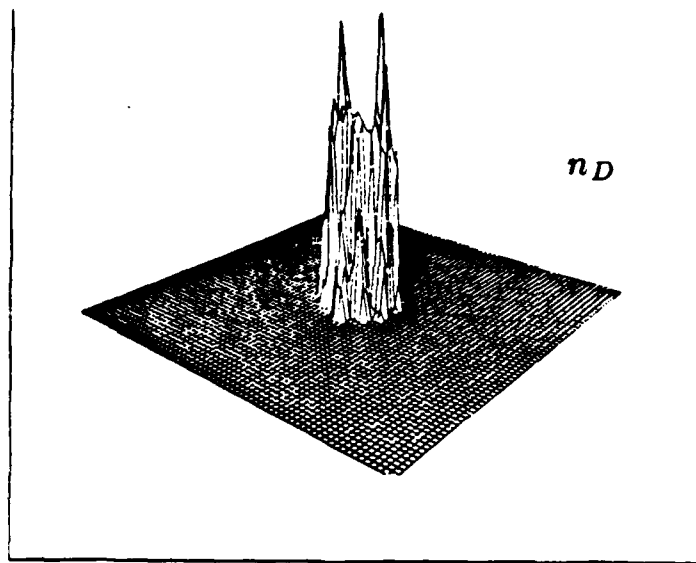


Figure 3.15. 3-D perspectives of the debris density, debris energy, and air ion energy at $\Omega, t = 72$ for the same run.

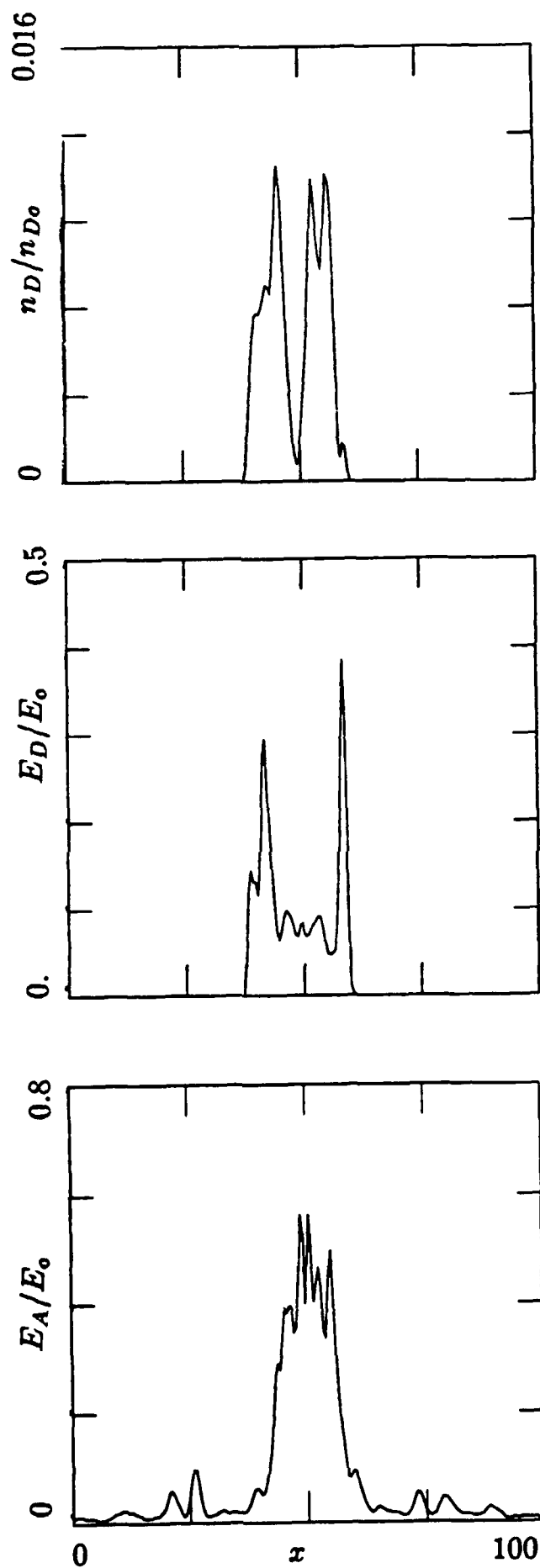


Figure 3.16. Slices in x of the debris density, debris energy, and air ion energy at the same time as in the previous figure.

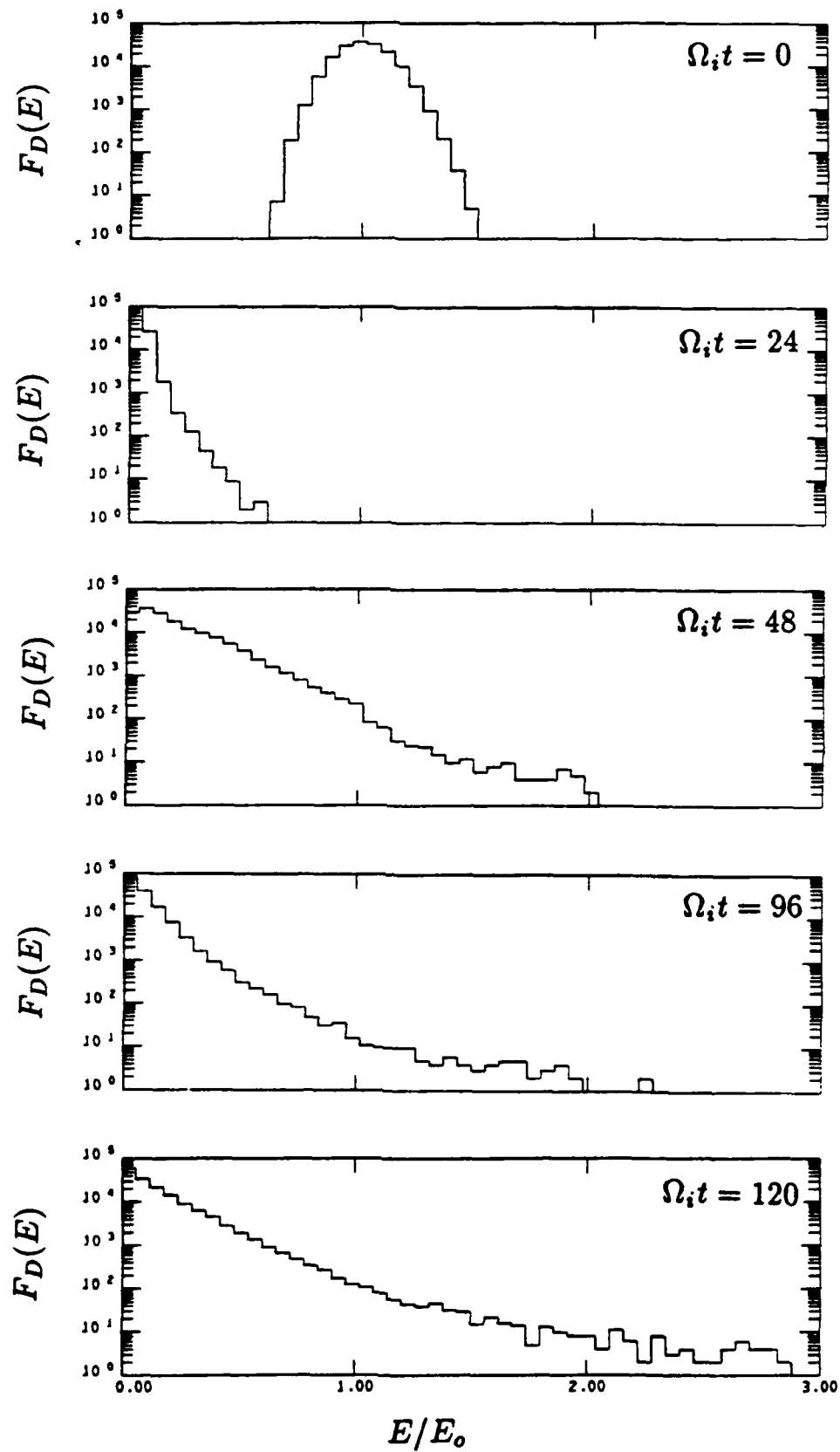


Figure 3.17. Energy spectra of the debris ions (normalized to the initial debris energy) at various times for the $M_D = 1$ run.

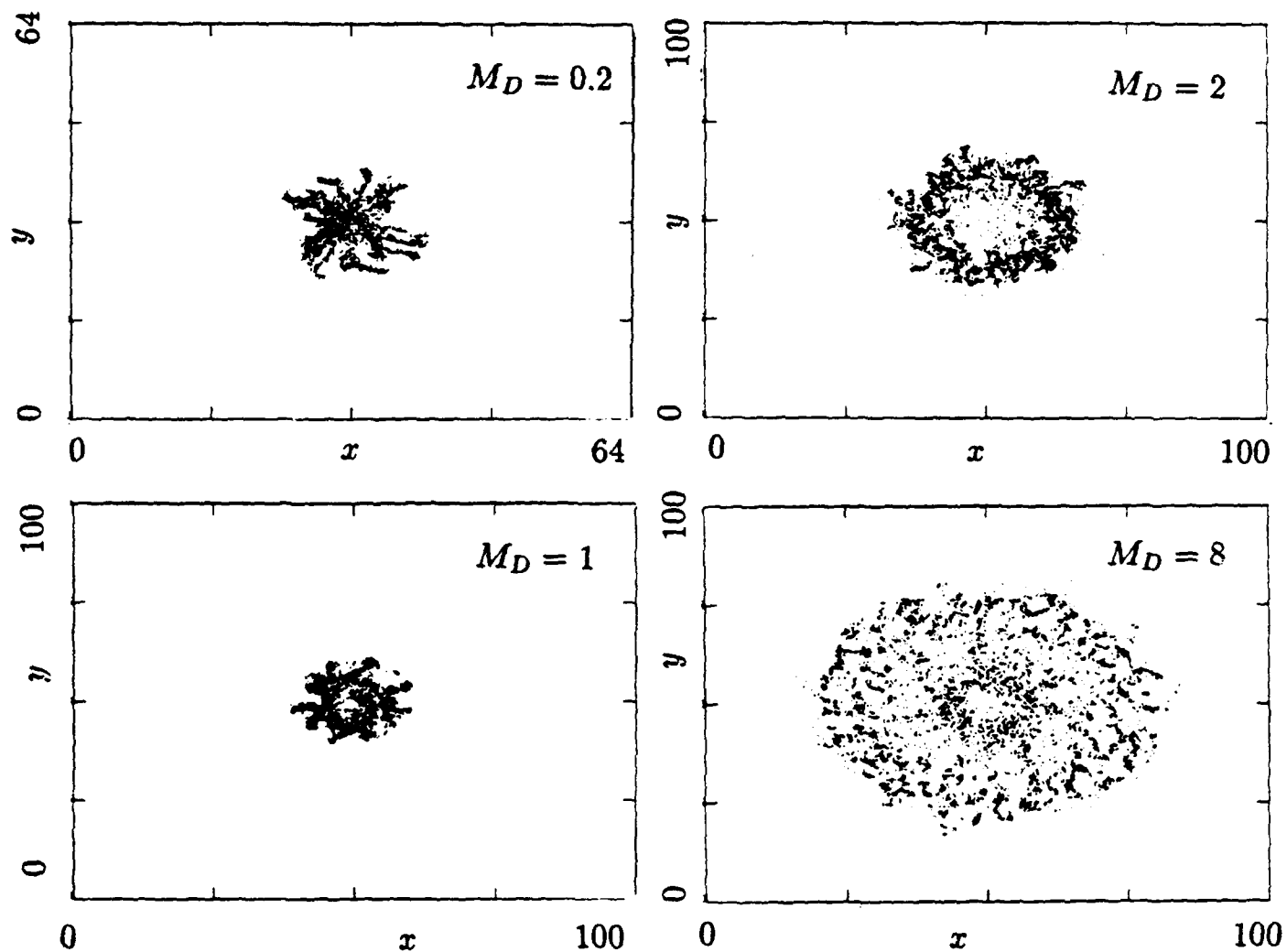


Figure 3.18. Debris ions in the x-y plane at the end of the calculation for runs with $M_D = 0.2, 1.0, 2.0, 8.0$.

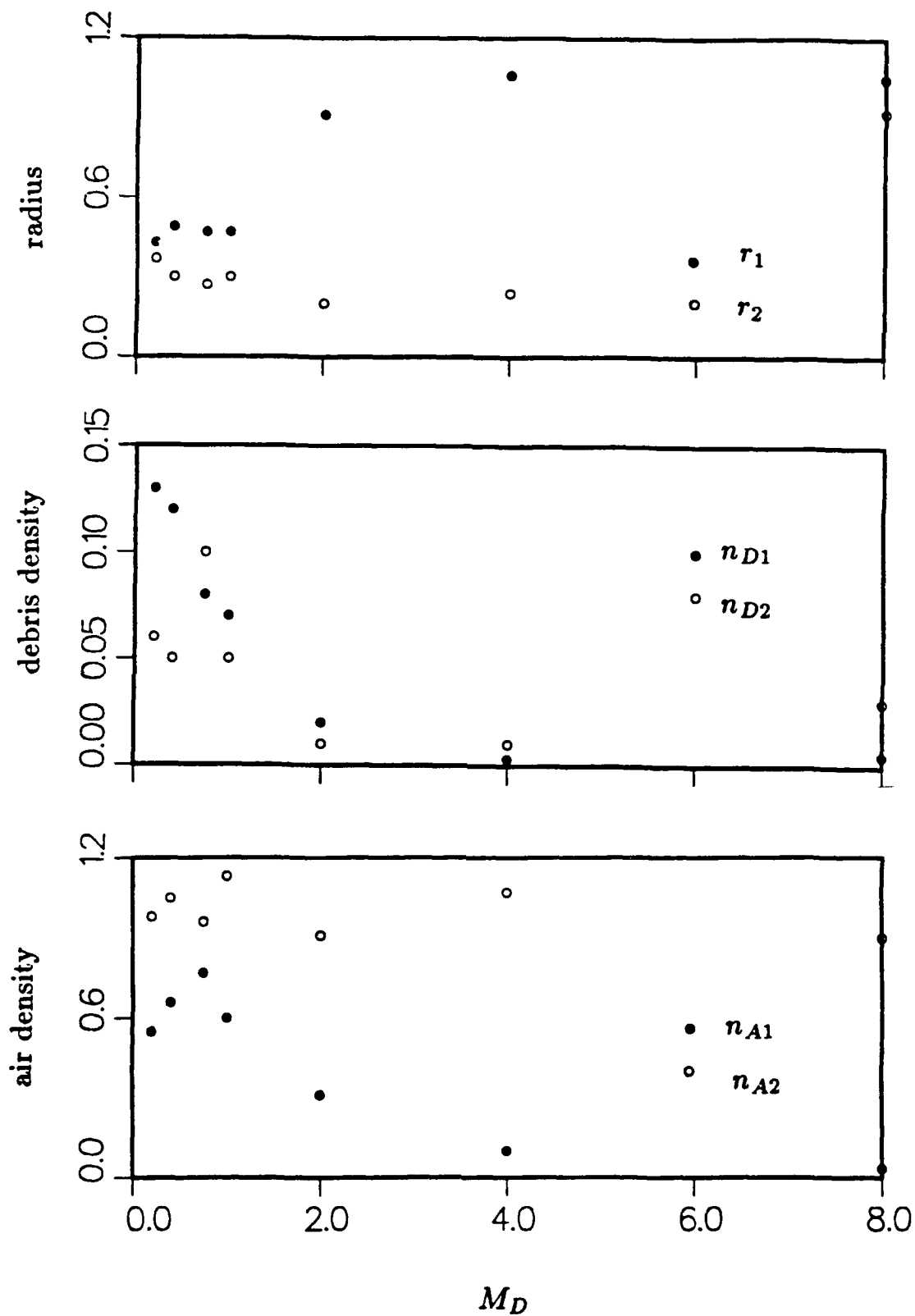


Figure 3.19. Results of simulations with various M_D showing: (top panel) normalized radii, r_1 and r_2 (normalized to r_* = confinement radius = smaller of R_B and R_M); (middle panel) debris density, n_{D1} , n_{D2} ; and (bottom panel) air density, n_{A1} , n_{A2} .

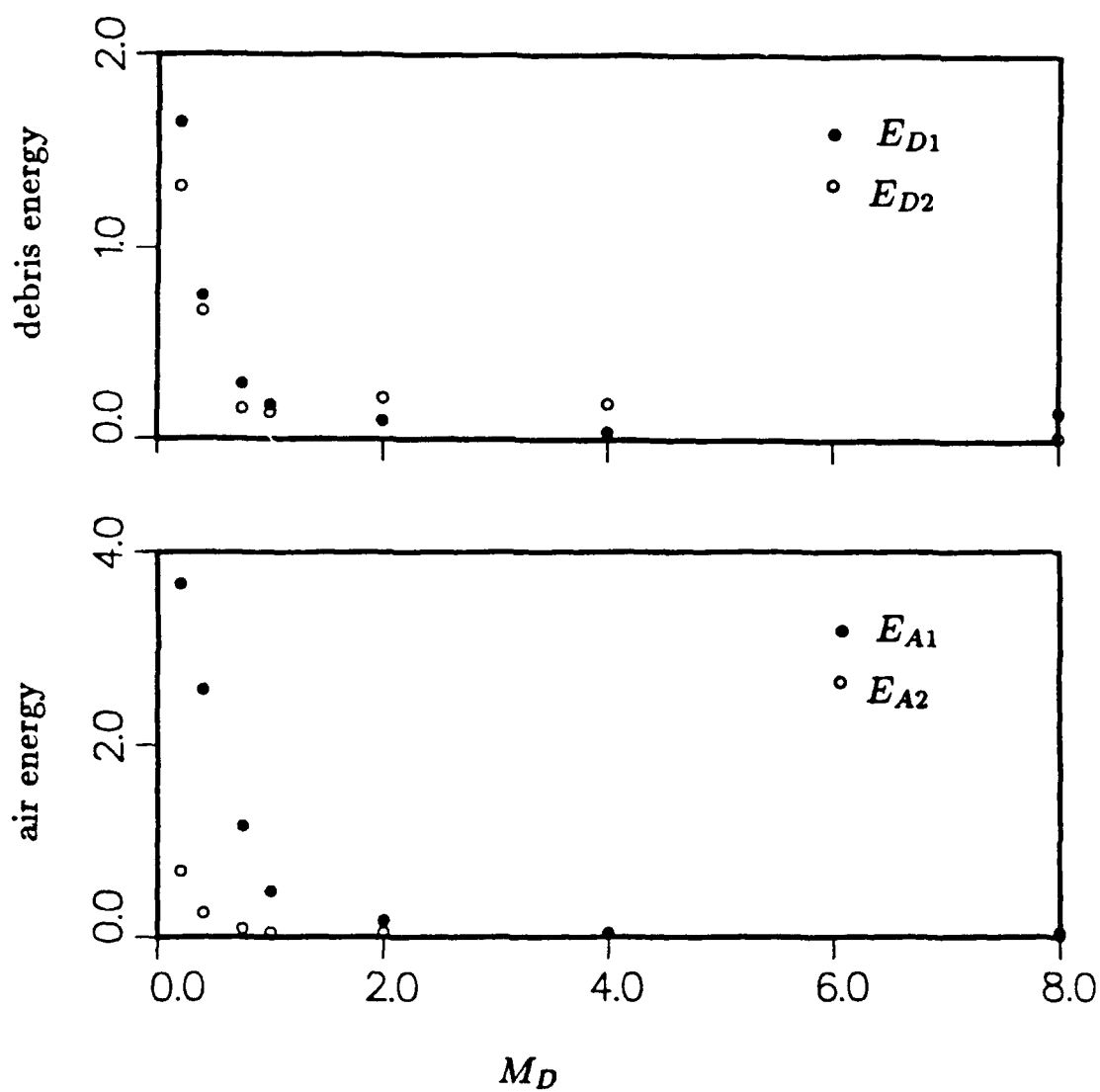


Figure 3.20. Results of simulations with various M_D showing: (top panel) debris energy, E_{D1} , E_{D2} ; and (bottom panel) air energy, E_{A1} , E_{A2} .

r_* , the smaller of the two stopping radii, are plotted versus M_D in the top panel of Figure 3.19. Both normalized radii are essentially constant out to $M_D \simeq 1$. For larger M_D , the normalized r_2 remains about constant (except at $M_D = 8$). This one larger value of r_2 and the larger values of r_1 for $M_D > 1$ is due in part to the lack of the magnetic field collapse eluded to earlier and to the larger ion gyroradii at larger M_D . On the other hand, it is also possible that the debris confinement radius does increase at higher M_D just because the magnetic field plays a less significant role. The middle panel of Figure 3.19 shows the debris density n_{D1} inside the cloud and in the outer halo (n_{D2}), normalized to the peak debris density. n_{D2} is about constant out to $M_D \simeq 1$, then decreases at larger M_D . The falloff of n_{D1} is due in part to the fact that the initial density relative to the background density decreases with M_D (to $M_D = 1$) [Table 3.1]. At higher M_D , when the initial peak debris density is constant, n_{D1} decreases because r_1 increases. The corresponding air densities are shown in the bottom panel of Figure 3.19. The air density inside the debris cloud is roughly constant at small M_D and decreases at large M_D , because the expanding shock at high Mach numbers tends to expel the air ions. The air density outside the main debris cloud is essentially constant. The next two graphs (Figure 3.20) show the energy of the debris (top panel) and air (bottom panel) ions in the main debris cloud and in the halo region. The energy tends to fall off monotonically with M_D . At small M_D the energy can exceed the initial energy; ions left in the cloud are heated at the magnetic field recompresses. The lower energy ($\sim 10\%E_o$) at higher M_D (≥ 1) reflects the fact that much of the initial energy goes into heating of the background ions outside of the debris cloud and in making large amplitude magnetic disturbances.

3.4 Summary

In this section we have discussed debris and air dynamics related to VHANE and HANE bursts. In particular, we have examined a series of hybrid simulations in which the debris Mach number is varied systematically. We showed results for three typical cases: a high Mach number expansion that corresponds to a weak HANE burst, a low Mach number expansion characteristic of a VHANE burst, and an intermediate case at $M_D = 1$. We also carried out a number of other runs and characterized the debris and air properties at the end of the calculation, when the debris and magnetic field recollapsed, as a function of M_D .

Generally, we find in the low M_D expansion, similar to those discussed in Section 1 of this report, that the debris remains well contained, although there is the usual structuring of the debris when it is stopped by the magnetic field. On recovery of the magnetic field the debris also collapses, maintaining its highly structured nature, and is heated in the process. Air ions trapped inside the debris are also heated. Outside the debris cloud there is little wave activity or air heating. In contrast, at higher M_D a shock forms as the debris expands, energizing the air ions in the outer region. Constraints of the present calculations do not allow the correct recollapse of the magnetic field, so the debris tends to remain out to a radius corresponding to the equal mass radius. Heating of the debris is smaller in this case, as much of the energy goes into the magnetic field disturbances and heating of the air ions. The intermediate $M_D = 1$ case shows aspects of both types of expansions. Like

the lower M_D cases, the debris structures at $r \simeq R_B \simeq R_M$, recollapses, and heats. Like the higher M_D runs, a (weak) expanding shock is formed and heats the air ions to some degree. It is not evident here that $M_D = 1$ is a special case or gives rise to particularly large magnetosonic waves.

In this study we have begun to develop scaling relations for HANE/VHANE bursts. It appears that the debris stays well confined, i.e., no large jetting is seen, at all Mach numbers. At lower M_D , the final radius is about half of the confinement radius; at larger M_D the final radius is roughly equal to the confinement radius. It has also been shown that the energy in the debris and air ions decreases with M_D . The energy remaining in the debris decreases to about 10% of the initial debris kinetic energy for $M_D \geq 1$, as more energy goes into heating of the background ions and in the generation of the shock. Because the present calculations are done in the two dimensions perpendicular to the ambient magnetic field direction, however, we cannot say how much debris remains in the burst region when dynamics along \vec{B} are included, and how that fraction varies with M_D . Later calculations will include such parallel effects and allow us to estimate this fraction. We also eventually plan to compare the results here with the more general 2-D calculations of Brecht [unpublished, 1991] and Simonson and Hewett [1991].

References

- Simonson, G., and D. W. Hewett, Recent magnetic debris containment calculations (U), Livermore National Lab. Report, UCRL-ID-10741, 1991.
- Thompson, J. H., Contact author for reference, 1991.

4. Parallel Streaming Deposition Model

4.1 Introduction

So far, we have discussed the case of debris-air dynamics perpendicular to the magnetic field in both the HANE and VHANE regime. When debris streams out perpendicular to \vec{B} , it is stopped by air ions in the HANE regime, and the magnetic field in the VHANE case. Some debris ions are deposited in the ionosphere, either because they stream down (or up) field lines or because they are turned from streaming perpendicular to the field to the parallel direction, as discussed in Section 2. Many more air ions are energized and deposited in the ionosphere as well, creating the kinetic energy patches. How far the ions go into the ionosphere and where they deposit their energy is generally treated as a simple single particle collisional process. At lower altitudes the background air density increases and the mean free path of the ions thus becomes shorter. The altitudes at which such collisional processes become important are typically below 200 km; above this height the mean free path is so large that the ions essentially free stream. For example, Kilb [1990] shows that an Fe^+ ion with a velocity of 270 km/sec has a mean free path of 38000 km when interacting with the atmosphere at 400 km.

However, it is well known that anomalous wave-particle processes in a plasma can reduce this streaming distance significantly. For example, ions backstreaming from the Earth's bow shock into the solar wind have a classical mean free path of about 10^8 km. *In situ* satellite measurements indicate that such ions are actually stopped over a distance on the order of 10^5 km [Bonifazi and Moreno, 1981]. This anomalously short stopping distance occurs because the backstreaming ions generate electromagnetic instabilities which produce waves that in turn scatter the ions [see Gary (1991) for a recent review]. These same kinds of electromagnetic instabilities have been observed in hybrid simulations of HANEs [Brecht and Thomas, 1988]. The issue to be addressed here is how one can estimate the effective stopping distance due to such instabilities and whether such an effect can be important for HANE and VHANE bursts. In Section 4.2 we review the basic physics and derive some elementary scaling relations. Then in Section 4.3 we apply these conditions to some simple models for HANE bursts. Finally, in Section 4.4 we draw some conclusions and suggest future refinements of the basic model.

4.2 Background

Electromagnetic instabilities resulting from the relative streaming of two ion components have been studied for a long time [Gary *et al.*, 1984; Winske and Leroy, 1984; Gary *et al.*, 1986; Gary, 1991]. Generally, these studies have involved homogeneous beams in space. The linear [Gary *et al.*, 1984] and quasi-linear [Winske and Leroy, 1984] properties of the instabilities have been studied analytically and numerically, while the nonlinear behavior have been deduced from hybrid simulation studies [Winske and Leroy, 1984; Gary *et al.*, 1986; Winske and Quest, 1986; Thomas and Brecht, 1986]. More recently, the instability has been studied in time [Miller *et al.*, 1991] and space [Onsager *et al.*, 1991] varying situations. These electromagnetic instabilities are particularly interesting in the HANE

regime because they are quite robust, i.e., they do not depend strongly on the details of the velocity distribution and they persist in a highly turbulent regime, when even the direction of the magnetic field is not well defined.

We consider a field aligned ion beam, density n_b and ion mass m_b , streaming with velocity V_b relative to a background plasma, ion density n_i and mass m_i , along an ambient magnetic field B_o . We define the total density $n_o = n_b + n_i$ and the Alfvén speed $v_A = B_o/(4\pi n_o m_i)^{1/2}$. We generally consider the plasma components as cold, i.e., $\beta_j = 8\pi n_o T_j / B_o^2 \leq 1$ where j is the plasma species (beam, background, or electrons). In this situation two electromagnetic ion beam instabilities can occur. One instability involves the (anomalous) cyclotron resonance of the Doppler shifted wave with the beam, i.e.,

$$\omega_r - kV_b \simeq -\Omega_b \quad (4.1)$$

where $\Omega_j = eB_o/m_j c$ is the cyclotron frequency of the j -th species. This instability will be referred to as the “resonant” mode. The other instability is a nonresonant (i.e., fluid) interaction that involves the presence of the beam to give an effective $T_{\parallel}/T_{\perp} > 1$. This mode, termed here the “nonresonant instability” is thus a fire-hose-like instability. There is no corresponding resonance condition like Eq. (4.1) for the nonresonant instability.

The two instabilities have distinct linear properties, which are exhibited in Figures 4.1-4.4. Figure 4.1 makes the point discussed above: namely, that the beam ions are in cyclotron resonance with the waves for the resonance mode, while waves generated by the nonresonant instability do not fall in velocity space where either ion species resides. Generally, the phase velocity of the resonant waves lies in the vicinity of the beam ions, while that of the nonresonant instability lies close to the background ions. Figure 4.2 shows growth rates for the resonant (R) and nonresonant (NR) instabilities maximized over wavenumber versus beam density n_b/n_o for $V_b/v_A = 10$ and $m_b = m_i$. The nonresonant instability has a finite threshold for growth. Above threshold the growth rate increases linearly with n_b/n_o . On the other hand, the resonant instability has no threshold: positive growth persists to $n_b \rightarrow 0$. However, the maximum growth rate increases more slowly with beam density so that eventually ($n_b/n_o > 0.08$) the growth rate of the nonresonant instability is larger. Figure 4.3 shows maximum growth rates as a function of V_b/v_A for $n_b/n_o = 0.1$. Both instabilities have a finite threshold, with that of the resonant mode being smaller. Above threshold γ increases linearly with V_b/v_A for the nonresonant mode to $V_b/v_A \sim 15$; thereafter it increases at a slower rate. On the other hand, the growth rate for the resonant mode increases very fast above threshold to a maximum value; at higher V_b/v_A the maximum growth rate is essentially constant. Figure 4.4 presents threshold values for the instabilities as a function of V_b/v_A and n_b/n_o . Generally, the resonant instability (solid curve) has a lower threshold, $V_b/v_A < 2$, which does not vary much with beam density. (The dotted line corresponds to conditions when the two modes have equal growth rates; above the line the nonresonant mode is more unstable.)

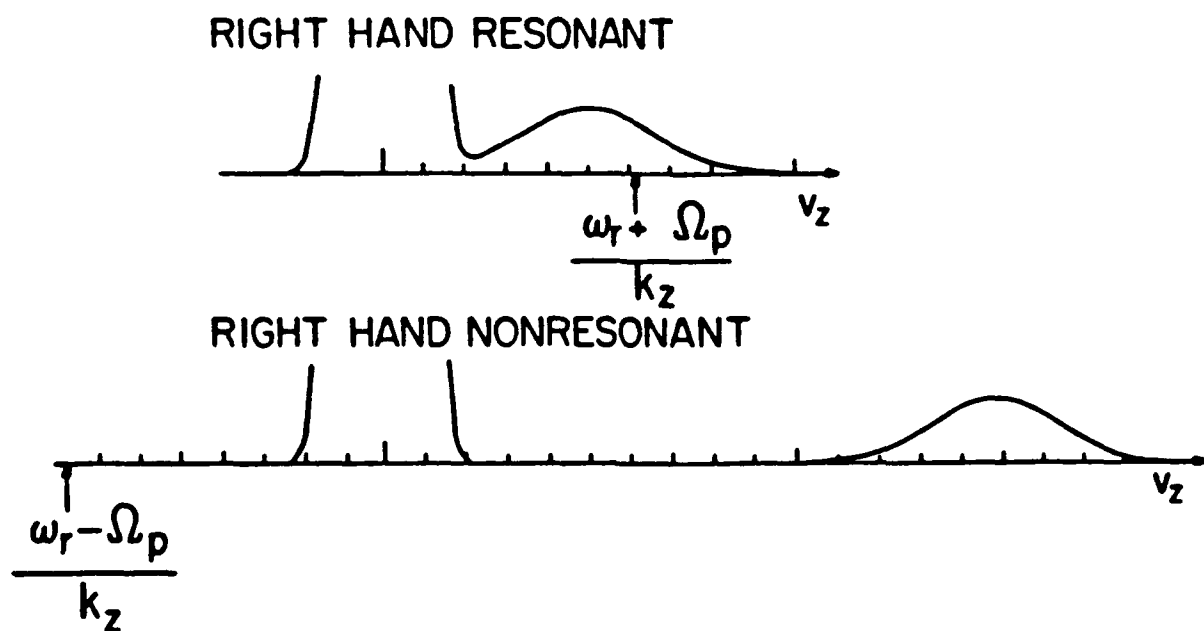


Figure 4.1. Schematic of background and beam velocity distributions along with the location of cyclotron resonances for the two instabilities.

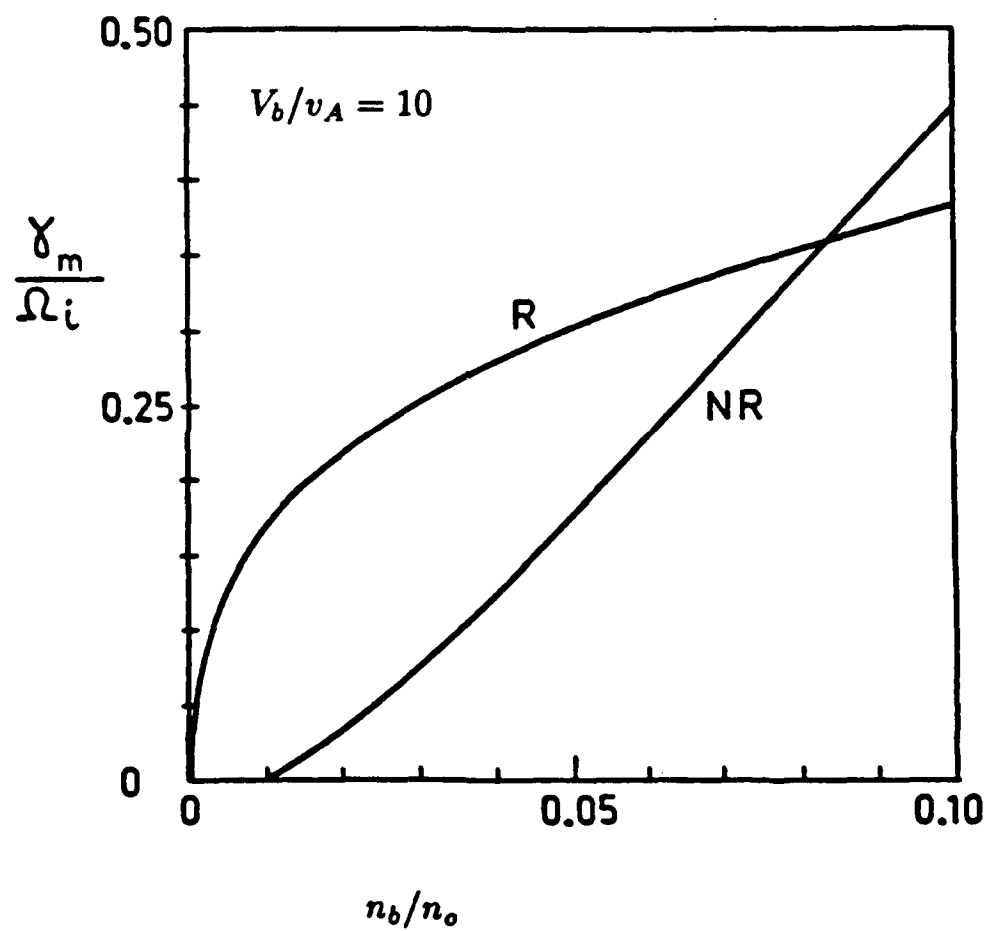


Figure 4.2. Growth rates for the resonant (R) and nonresonant (NR) instabilities maximized over wavenumber versus n_b/n_o for $V_b/v_A = 10$.

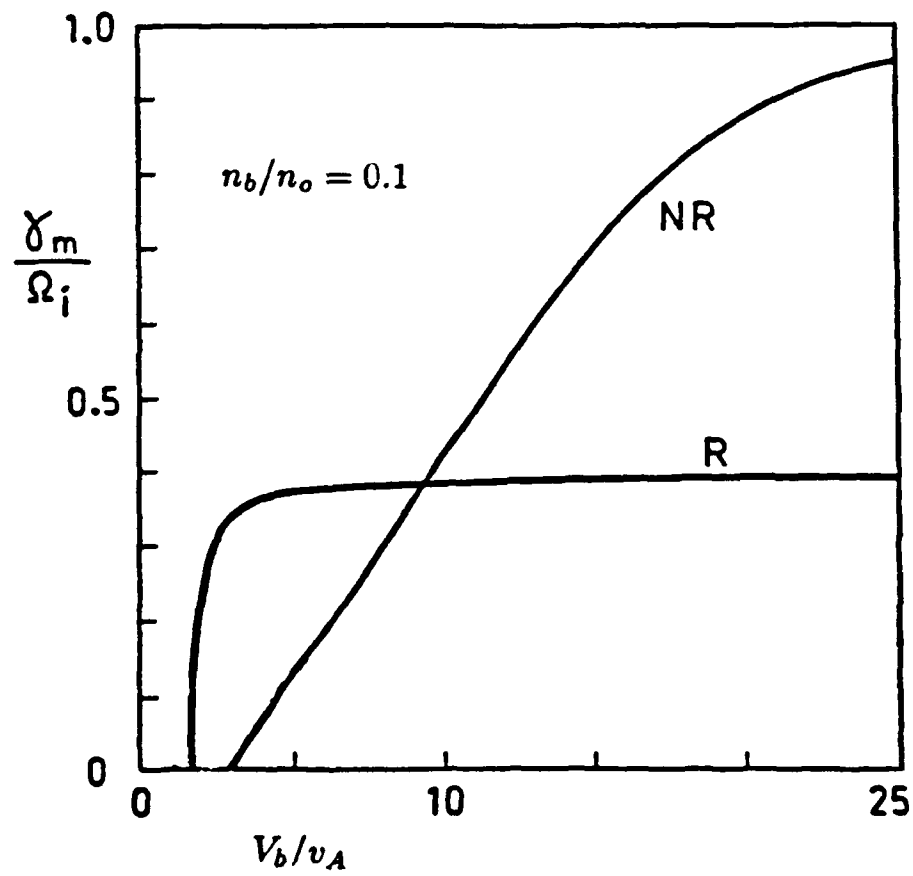


Figure 4.3. Growth rates maximized over wavenumber for the two instabilities as a function of V_b/v_A for $n_b/n_o = 0.1$.

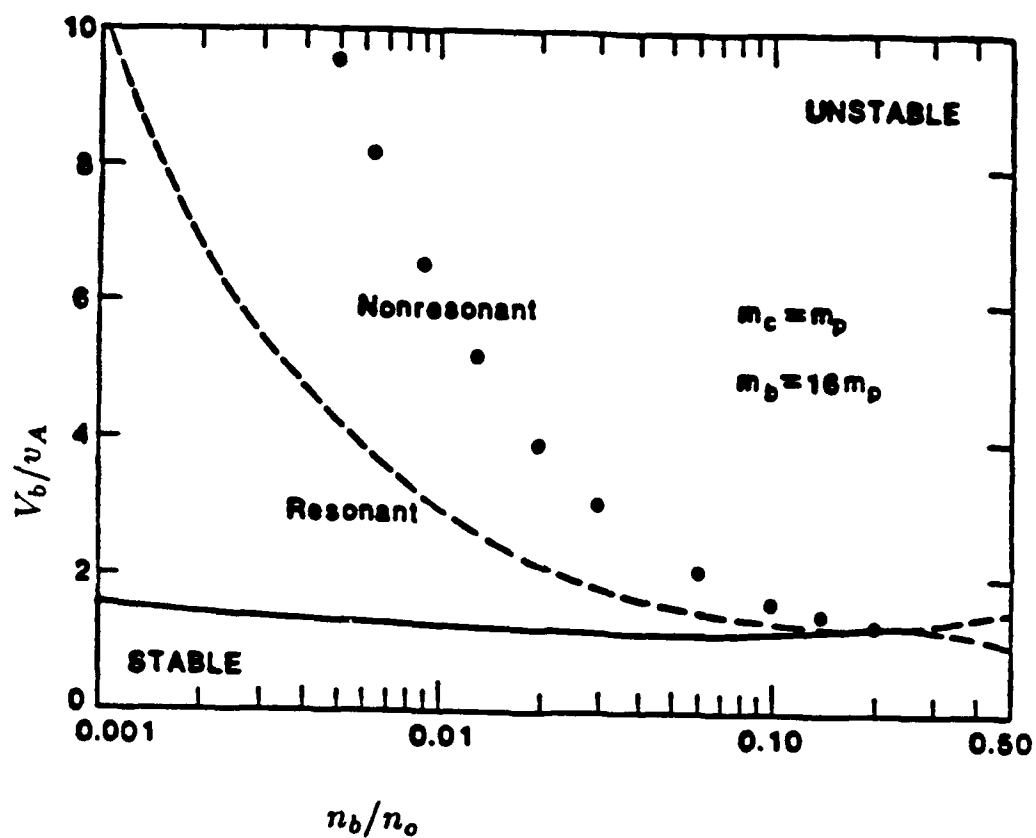


Figure 4.4. Thresholds for the resonant (solid curve) and nonresonant (dashed curve) instabilities as a function of V_b/v_A and n_b/n_o . The dotted curve is where the two instabilities has equal growth rates; above the curve the nonresonant instability dominates.

We can summarize the linear properties of the two instabilities as follows. The growth rates of the two modes vary as:

$$\text{resonant : } \frac{\gamma}{\Omega_i} \simeq \frac{1}{2} \left(\frac{n_b}{n_o} \right)^{1/3} \left(\frac{m_i}{m_b} \right)^{2/3} \quad (4.2)$$

$$\text{nonresonant : } \frac{\gamma}{\Omega_i} \simeq \frac{1}{2} \frac{n_b}{n_o} \frac{V_b}{v_A} \quad (4.3)$$

Also, the thresholds for the two instabilities can be expressed as:

$$\text{resonant : } V_b \sim 1 - 2v_A \quad (4.4)$$

$$\text{nonresonant : } V_b > \left(\frac{n_o}{n_b} \frac{m_i}{m_b} \right)^{1/2} v_A \quad (4.5)$$

Again, this result follows from Figure 4.4.

In addition to these linear properties the nonlinear evolution of these two instabilities has been studied extensively via hybrid simulations in both 1-D [Winske and Leroy, 1984; Gary *et al.*, 1986] and in 2-D [Winske and Quest, 1986; Thomas and Brecht, 1986]. Figure 4.5 shows an example of a 1-D calculation. Here V_b/v_A is taken to be 10 and $n_b/n_o = 0.02$, i.e., in this case the resonant instability dominates. The left panels of the figure show $v_x - x$ phase space for the two ion species at various times. The right panels show profiles in x of one component of the magnetic field at the same times. Initially, there are two well defined ion streams and no fluctuations. As the instability is excited, waves grow and the beams begin to couple together. Times are expressed here in terms of the inverse growth time. By $t = 5/\gamma$ coupling of the two beams has begun, and by $t \sim 10/\gamma$ the beams have completely merged.

One issue that is particularly important for the HANE case is the effect of a finite length beam (as we will see later), which occurs as the debris ions compress into a thin coupling shell. Figure 4.6 shows a simulation of a finite length beam segment interacting with a uniform background plasma [Onsager *et al.*, 1991]. One sees that very quickly ($\Omega_i t = 10$) there is already the beginning of significant slowing of the beam and background plasmas and eventually both are strongly coupled. In this case $n_b/n_o = 0.4$ and $V_b/v_A = 10$, so that Eq. (4.2) implies $\gamma/\Omega_i \simeq 0.4$ and $\Omega_i t \simeq 10$ corresponds to $\gamma t = 4$. Detailed analysis of such simulations indicate that while the nonresonant instability has a larger linear growth rate, the resonant mode is actually more important because the resonant mode remains in contact with the finite length beam for a longer period of time. Based on these simulation results and linear theory, we can then construct a coupling model.

4.3 HANE Coupling Model

The HANE anomalous debris coupling model is based on Eqs. 4.2-4.5 and the above discussion concerning the simulations. The basic assumption of the model is that when the debris density exceeds the ambient air density, the relevant instability is the nonresonant

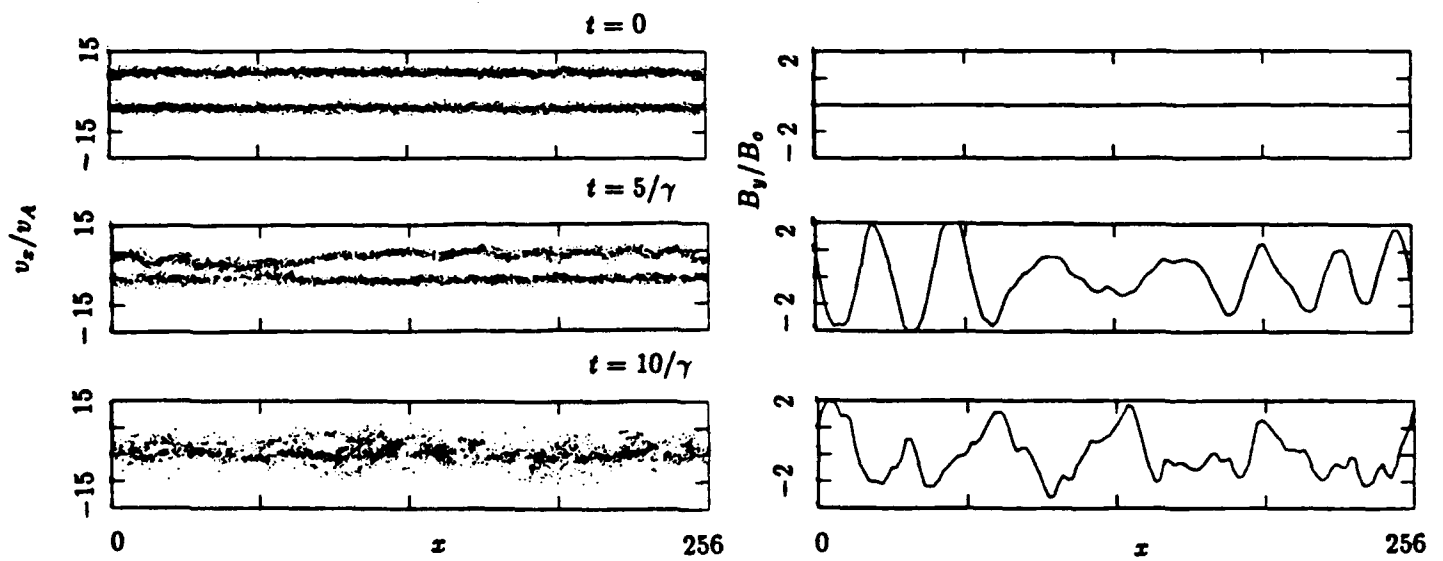


Figure 4.5. Results of a 1-D hybrid simulation ($n_b/n_o = 0.02$, $V_b/v_A = 10$) showing growth of waves (right panels) and coupling of the two ion streams (left panels).

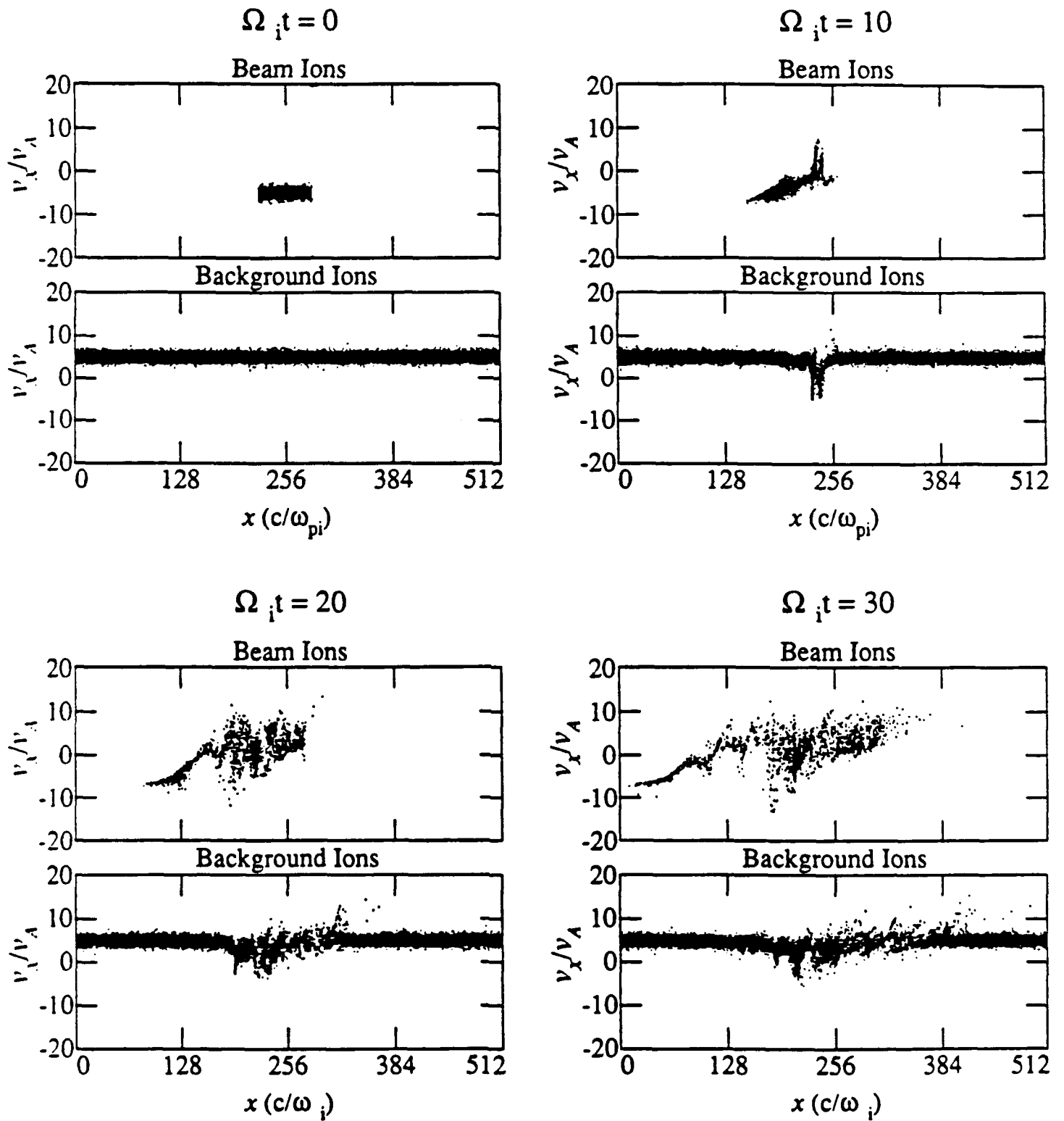


Figure 4.6. Results of a 1-D hybrid simulation with a finite length ion beam ($n_b/n_o = 0.4, V_b/v_A = 10$) showing rapid coupling of the two beams due to the resonant instability.

mode. In this case the debris acts like the background plasma and the nonresonant mode is most important because it propagates with a phase velocity near that of the debris. The resonant instability is more relevant when either the nonresonant instability is stable (it has a higher threshold than the resonant mode) or when the debris density is less than that of the ambient air. In either case we compute the (local) growth rate γ and take the coupling time to be $5/\gamma$. In terms of equations, the model is thus:

1. When $n_D > n_A$ and

$$V_D > \left(\frac{n_A + n_D}{n_A} \frac{n_A}{n_D} \right)^{1/2} v_A \quad (4.6)$$

the nonresonant mode dominates. Its growth rate is

$$\gamma = \frac{1}{2} \left(\frac{n_A^{1/2} n_D^{1/2}}{n_A + n_D} \right) \frac{V_D}{v_A} \left(\frac{m_A}{m_D} \right)^{1/2} \Omega_A \quad (4.7)$$

where v_A is computed using the background air density and mass.

2. When $n_D < n_A$ and $V_D > 1.5v_A$, the resonant mode dominates with

$$\gamma = \frac{1}{2} \left(\frac{n_D}{n_A + n_D} \right)^{1/3} \left(\frac{m_A}{m_D} \right)^{2/3} \Omega_A \quad (4.8)$$

In both cases the coupling time is

$$\tau_c \sim 5/\gamma \quad (4.9)$$

and the anomalous coupling distance is roughly

$$X_{an} \sim 5V_D/\gamma \quad (4.10)$$

This simple model does not necessarily give a smooth transition from one regime to another, nor does it attempt to work out the continuous slowing of the debris. As we show next, we are only interested at this point in comparing these coupling times and distances with their collisional counterparts to look for large differences between the two rates.

We assume a 1 MT burst yielding 10^{15} J of kinetic energy, i.e., 500 kg of mass with velocity $V_D = 2000$ km/sec. Taking the debris ion atomic mass $A=30$ then yields $N_D = 10^{28}$ debris ions. We shall assume two spatial models for the debris that represent extreme limits. First, we assume that the debris expands into a sphere of radius R with uniform density, i.e.,

$$N_D = \frac{4\pi}{3} R^3 n_D(R) \quad (4.11)$$

or

$$n_D(R) = \frac{2.4 \times 10^{12}}{R^3(\text{km})} \text{ cm}^{-3} \quad (4.12)$$

We consider a burst at 800 km, roughly halfway between STARFISH altitudes (~ 400 km) and the VHANE regime (~ 1200 km). We take air mass densities from Kilb [1990] along with collisional coupling lengths, X_{cl} . Taking the magnetic field to be 0.3G and the air atomic mass to be 14, we find that the ambient air number density is

$$n_A = 4.3 \times 10^{22} \rho_b \text{ cm}^{-3} \quad (4.13)$$

where ρ_b is the air mass density in gm per cm^{-3} . The Alfven speed is

$$v_A = 1.75 \times 10^5 n_A^{-1/2} \text{ km/sec} \quad (4.14)$$

At altitude h , the debris density is thus

$$n_D(h) = \frac{2.4 \times 10^{12}}{(800 - h)^3} \quad (4.15)$$

In Table 4.1 are tabulated values for ρ_b , n_A , n_D , and V_A at various altitudes h . We see that in this model the debris density is always less than the air density. In this case we use Eq. (4.8) to evaluate the growth rate and (4.10) to estimate the anomalous coupling distance. The last column in the table is the collisional coupling distance. As one might expect from this model, at higher altitudes the debris density is larger, giving rise to larger growth rates and hence shorter coupling distances. Above ~ 330 km the anomalous coupling distance is shorter than the collisional stopping length. At 600 km, where the collisional mean free path is essentially infinite, the anomalous stopping distance is about 400 km. Because the anomalous stopping distance increases at lower altitude, $X_{an} \sim 400$ km is a lower limit. From Table 4.1 we see that the collisional stopping distance at 200 km (i.e., 600 - 400 km) is also small. Thus, one would expect that the overall collisional and anomalous stopping distances are about the same in this case. However, the details of how the ions slow down and deposit their energy along the trajectory may be different.

The second limiting case we consider assumes that the debris compresses into a thin coupling shell of thickness $\rho_i = V_D/\Omega_D \sim 20$ km. In this case the debris density falls off at a much slower rate

$$N_D = 4\pi R^2 n_D(R) \Delta \quad (4.16)$$

with $\Delta \sim \rho_i$ so that for an 800 km burst

$$n_D = \frac{4 \times 10^{15}}{(800 - h)^2} \text{ cm}^{-3} \quad (4.17)$$

As we show in Table 4.2, the debris density now exceeds the air density at all altitudes down to 200 km. In this case the nonresonant instability [Eq. (4.7)] dominates. At lower altitudes the debris density drops, while the air density increases, which increases the ratio of $n_A/(n_A + n_D)$. The ratio of V_D/v_A also rises rapidly, so that the growth rate increases. Consequently, the anomalous stopping distance becomes shorter. For all values

Table 4.1. Comparison of anomalous and collisional stopping distances for a burst at 800 km with a uniform debris distribution [Eq. (4.11)].

$h(km)$	$\rho_b(g/cm^3)$	$n_A(cm^{-3})$	$n_D(cm^{-3})$	$v_A(km/s)$	$\gamma(sec^{-1})$	$X_{an}(km)$	$X_{cl}(km)$
200	2.5×10^{-13}	1.1×10^{10}	1.1×10^4	1.7	0.6	16100	55
250	6.3×10^{-14}	2.7×10^9	1.4×10^4	3.4	1.1	9300	320
300	2.1×10^{-14}	9.0×10^8	1.9×10^4	5.8	1.7	5900	1050
400	9.2×10^{-16}	4.0×10^7	3.8×10^4	28	6.0	1660	4×10^4
600	1.0×10^{-16}	4.3×10^6	3.0×10^5	84	25.	400	∞

Table 4.2. Comparison of anomalous and collisional stopping distances for a burst at 800 km with a shell debris distribution [Eq. (4.16)].

$h(\text{km})$	$\rho_b(\text{g/cm}^3)$	$n_A(\text{cm}^{-3})$	$n_D(\text{cm}^{-3})$	$v_A(\text{km/s})$	$\gamma(\text{sec}^{-1})$	$X_{an}(\text{km})$	$X_{cl}(\text{km})$
200	2.5×10^{-13}	1.1×10^{10}	1.1×10^{10}	1.7	84000	0.1	55
250	6.3×10^{-14}	2.7×10^9	1.3×10^{10}	3.4	15500	0.7	320
300	2.1×10^{-14}	9.0×10^8	1.6×10^{10}	5.8	5400	1.9	1050
400	9.2×10^{-16}	4.0×10^7	2.5×10^{10}	28	200	50	4×10^4
600	1.0×10^{-16}	4.3×10^6	1.0×10^{11}	84	0.5	2×10^4	∞

of h , X_{an} is less than X_{cl} by about three orders of magnitude. Thus, even if we double the coupling times [Eq. (4.10)] and increase the thickness of the debris shell by a factor of 5, X_{an} will still be less than X_{cl} by two orders of magnitude. We should also remark that the analytic approximations for the growth rates may not be valid for very extreme parameters ($V_D/v_A \gg 1$) such that the coupling distance becomes comparable to the wavelength of the mode.

4.4 Summary

In this section we have used well known properties of electromagnetic ion beam instabilities to derive a simple model for anomalous debris-air coupling when the debris streams along field lines. The model is based on the local debris and air densities and the relative streaming velocity compared to the local Alfvén speed. When the debris density exceeds that of the air, the nonresonant instability dominates, with a threshold condition for growth given by Eq. (4.6) and a growth rate by Eq. (4.7). This type of situation might occur in a HANE burst if the debris velocity spread is fairly small and the debris streams out in a narrow shell. In this case the anomalous coupling distance decreases at lower altitudes, as does the usual collisional stopping distance. These two effects then can work together to deposit the energy at higher altitudes.

A more likely situation, however, is that the debris will spread out over a larger spatial region with a lower density, less than that of the air (except for very high altitude bursts). In this case the resonant electromagnetic ion beam instability provides the coupling. As the ratio of debris to air density decreases at lower altitudes, this type of coupling becomes less effective, unlike collisional processes.

Thus far, we have shown that under some conditions anomalous slowing of energetic debris as well as of air ions can yield stopping distances (mean free paths) much shorter than those obtained by collisional effects. This has been demonstrated for specific point by point comparisons. What is actually needed, however, is a formula valid for the entire path length of an energetic ion to give the integrated, rather than the local, effect. When the slowing down rate are small, one could imagine using a WKB-like approach to estimate the cumulative effect of the slowing of an energetic ion. And one may wish to consider the ions as deposited according to where they lose their energy, rather than to their final stopping point [Sappenfield, private communication, 1990]. To investigate these processes more accurately, one should carry out simulations of debris ions with a finite spatial spread interacting with an air background that contains an exponentially increasing density. Such calculations would then allow comparison with the simple formulas derived here as well as testing the sensitivity of parameters of the debris deposition model. We defer this more detailed study to the future.

4.5 References

- Bonifazi, C., and G. Moreno, Reflected and diffuse ions backstreaming from the Earth's bow shock, 2. Origin, *J. Geophys. Res.*, **86**, 4405, 1981.
- Brecht, S. H., and V. A. Thomas, Contact authors for reference, 1988.
- Gary, S. P., Electromagnetic ion/ion instabilities and their consequences in space plasmas: A review, *Space Sci. Rev.*, **56**, 373, 1991.
- Gary, S. P., C. W. Smith, M. A. Lee, M. L. Goldstein, and D. W. Forslund, Electromagnetic ion beam instabilities, *Phys. Fluids*, **27**, 1852, 1984.
- Gary, S. P., C. D. Madland, D. Schriver, and D. Winske, Computer simulations of electromagnetic cool ion beam instabilities, *J. Geophys. Res.*, **91**, 4188, 1986.
- Kilb, R. W., Working paper, November, 1990.
- Miller, R. H., T. I. Gombosi, S. P. Gary, and D. Winske, The directional dependence of magnetic fluctuations generated by cometary ion pickup, *J. Geophys. Res.*, **96**, 9479, 1991.
- Onsager, T. G., D. Winske, and M. F. Thomsen, Interaction of a finite length ion beam with a background plasma: Reflected ions at the quasi-parallel bow shock, *J. Geophys. Res.*, **96**, 1775, 1991.
- Thomas, V. A., and S. H. Brecht, Simulation of magnetic phenomena driven by parallel ion motion, *Phys. Fluids*, **29**, 3398, 1986.
- Winske, D., and M. M. Leroy, Diffuse ions produced by electromagnetic ion beam instabilities, *J. Geophys. Res.*, **89**, 6623, 1984.
- Winske, D., and K. B. Quest, Electromagnetic ion beam instabilities: Comparison of one and two dimensional simulations, *J. Geophys. Res.*, **91**, 8789, 1986.

5. Multibursts

5.1 Introduction

The question of nuclear phenomenology related to multiple nuclear bursts at high altitudes remains largely unknown. The systems codes generally treat the effects of each burst separately, but include atmospheric heave due to earlier bursts [Sappenfield, 1987]. However, the dynamics of debris and air interactions in such situations has not been studied in great detail. In this section we present a few preliminary results of kinetic simulations of two simultaneous bursts in the VHANE regime. This regime is chosen because the dynamics are simpler and better understood. In particular, we will show an example of a full particle calculation that indicates both electron and ion heating exceeding that from a single burst. We also present an example of a hybrid code run with a background plasma that shows different ion dynamics. We feel that multibursts in the VHANE regime also offer the possibility of doing unique ion/ion interactions on the AGNES laser facility, as discussed later.

5.2 Particle Simulation of a Multiburst

In the past few years we have carried out particle simulations of VHANEs over a wide range of conditions [Winske, 1987, 1988, 1990; Winske and Jones, 1990]. Most of these calculations have been done in the large gyroradius limit ($\rho_i/R_B = \text{ion gyroradius/magnetic confinement radius} \geq 1$) and show the development of a structuring instability on the surface of the expanding plasma cloud and related ion and electron heating. Here, we carry out a comparable particle simulation of two simultaneous bursts. In this case we take two equal bursts, each with $\rho_i = R_B = 8c/\omega_e$, expanding in 2-D perpendicular to an ambient magnetic field. The separation between the two bursts in this case is also R_B . The results of the calculation are shown in Figures 5.1-5.3. Figure 5.1 shows the debris ions in x-y space at several times. The ions for each burst are displayed in separate (left-right) panels. As in a single burst, the ions expand, compress into a shell, and structure. At later times the inner most ions contract, while the ions on the outer edge continue to expand, leading to a cloud that extends out beyond R_B . In addition to these single burst effects, there is obviously an interaction going on where the two clouds intersect. The ions in this region are more diffuse, i.e., the flutes are somewhat more elongated and the ions are more scattered. This asymmetry persists to late times. Note in particular that the debris from the two clouds tends to mix together.

Figure 5.2 shows corresponding plots for the electrons from the two bursts. As with the ions, one sees expansion, compression, and structure. However, the electrons do not mix together. This is not unexpected, as the electron gyroradius is much smaller. Charge neutrality is maintained as the electrons associated with the debris ions from one burst just pair up with other debris ions at late times as the ions (with larger gyroradius) intersect.

Ion and electron heating associated with this process is shown in Figure 5.3. where the ions (left panel) and electrons (right panel) from one burst are shown at two different times

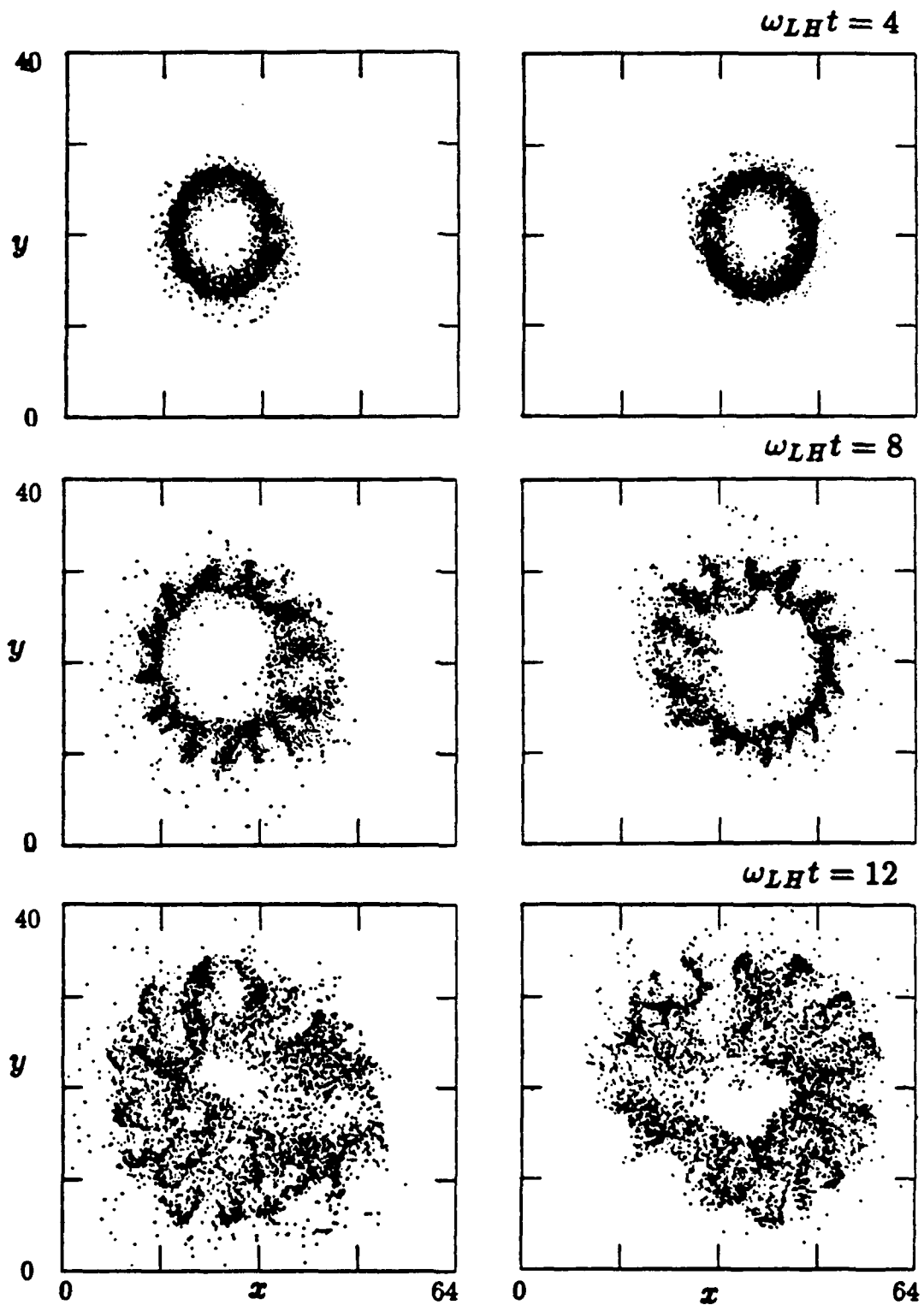


Figure 5.1. Results of particle simulations of two simultaneous expanding plasma clouds, showing the ions of each burst separately. The structure is more pronounced on the colliding side. (Lengths are normalized to c/ω_e .)

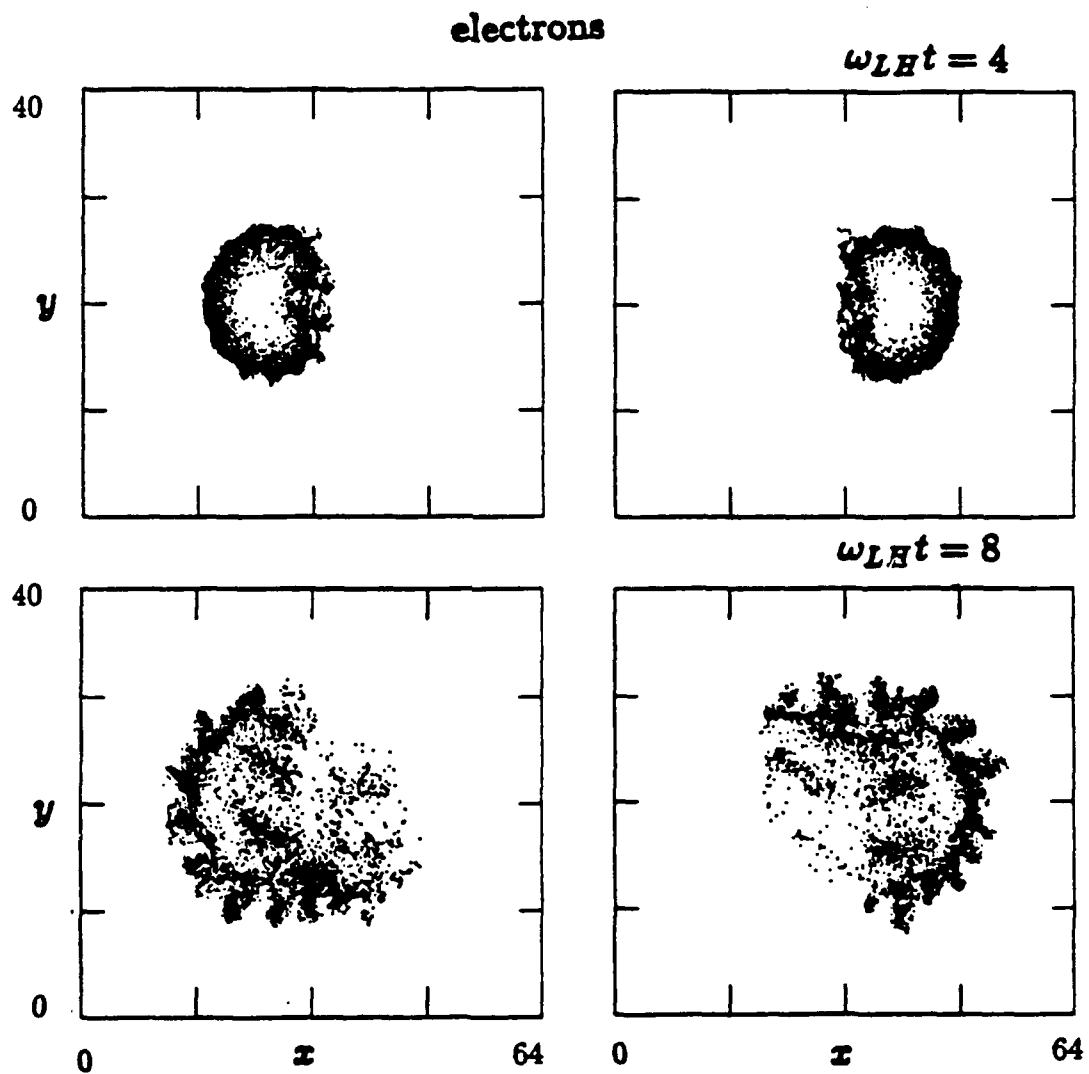


Figure 5.2. Results of the same run showing the electrons; unlike the ions, the electrons of one cloud do not penetrate into the other cloud.

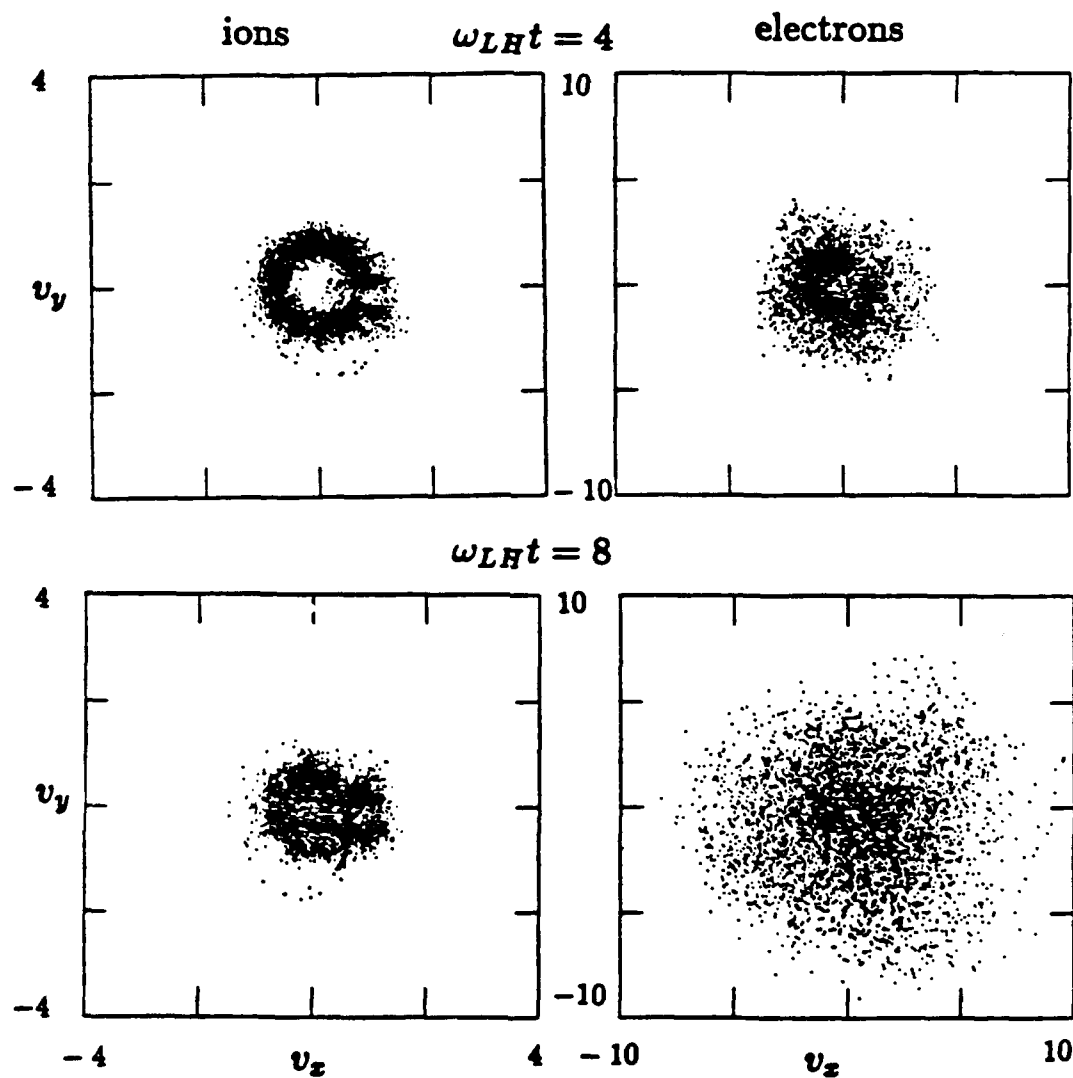


Figure 5.3. Results of the same run showing velocity space perpendicular to the magnetic field. Ions are energized in the direction of the other cloud, while electron heating is isotropic. (Velocities are normalized to the expansion velocity.)

($\omega_{LH}t = 4$, corresponding to the appearance of structure and $\omega_{LH}t = 8$ corresponding to strong penetration of the two debris clouds). There is strong ion heating in the region of the overlap of the two clouds; the energization is directed toward the other cloud. Electron heating is also quite strong and essentially isotropic.

It is believed that the heating and other effects associated with the multiburst case are not due to any sort of ion/ion streaming instability. Instead, the heating is attributed to two effects: (1) interaction with the macroscopic fields and (2) interaction with the waves generated by the flute instability. The first process involves ions from one burst interacting with the macroscopic electric field of the second burst, which tends to accelerate some ions toward the center of the second cloud (Figure 5.3). There is also the effect that the ions are expanding into a region of essentially zero magnetic field so that they become even less "magnetized" than they were previously. The second process, namely the interaction with waves generated by the instability in each burst separately, leads to the strong, nearly isotropic electron heating. Later, in Section 5.4 we will return to the question of the possible generation of direct ion/ion instabilities and their possible role in electron and ion heating in multibursts.

5.3 Hybrid Simulation of a Multiburst

We have also carried out a few multiburst simulations using a hybrid (particle ions, massless fluid electrons) code. The calculations are similar to those in Section 1, except that now there are two equal debris clouds expanding perpendicular to a background magnetic field. An example of one such calculation is shown in Figures 5.4-5.7. In this case the initial debris density of the clouds relative to the background plasma is $n_{D0}/n_0 = 41$, and the debris masses are $m_D/m_e = 4$. The separation of the clouds is $r_s = R_B = 12.8c/\omega_i$. The debris expands at $M_D = V_D/v_A = 0.5$ with a directed gyroradius of $2c/\omega_i$. Figure 5.4 displays contour plots of the density at various times. One sees the initial expansion of the two clouds and their compression into thin shells. As the two clouds intersect, there is a complex collision ($\Omega_i t = 32$) with the formation of one cavity by $\Omega_i t = 48$. At later times the clouds recollapse with the magnetic field. The corresponding contours of the magnetic field are shown in Figure 5.5. Again, the initial intersection of the two cavities and their eventual merging into a single cavity along with the later recovery of the magnetic field is evident.

A time series showing ion dynamics for one of the debris clouds is presented in Figure 5.6. As in the full particle runs, one again sees the initial radial expansion, the plasma being squeezed into a thin shell, and flute modes growing on the surface. (As is well known, in the hybrid simulations of VHANE expansions [Thomas and Brecht, 1988], the structure forms somewhat later than in the full particle simulations.) As in the single burst expansion (lower right panel), the collapse of the debris carries along its embedded structure, leading to a final debris cloud with $r \sim R_B/2$ that remains highly turbulent. However, unlike the full particle simulations, the debris from the two clouds does not intersect. In this case as the clouds expand, air ions become trapped between the two clouds, giving rise to a large radial electric field ($E_r \sim \nabla p_e$) that tends to repel the debris ions.

Hybrid Simulations: 2-D \perp to B

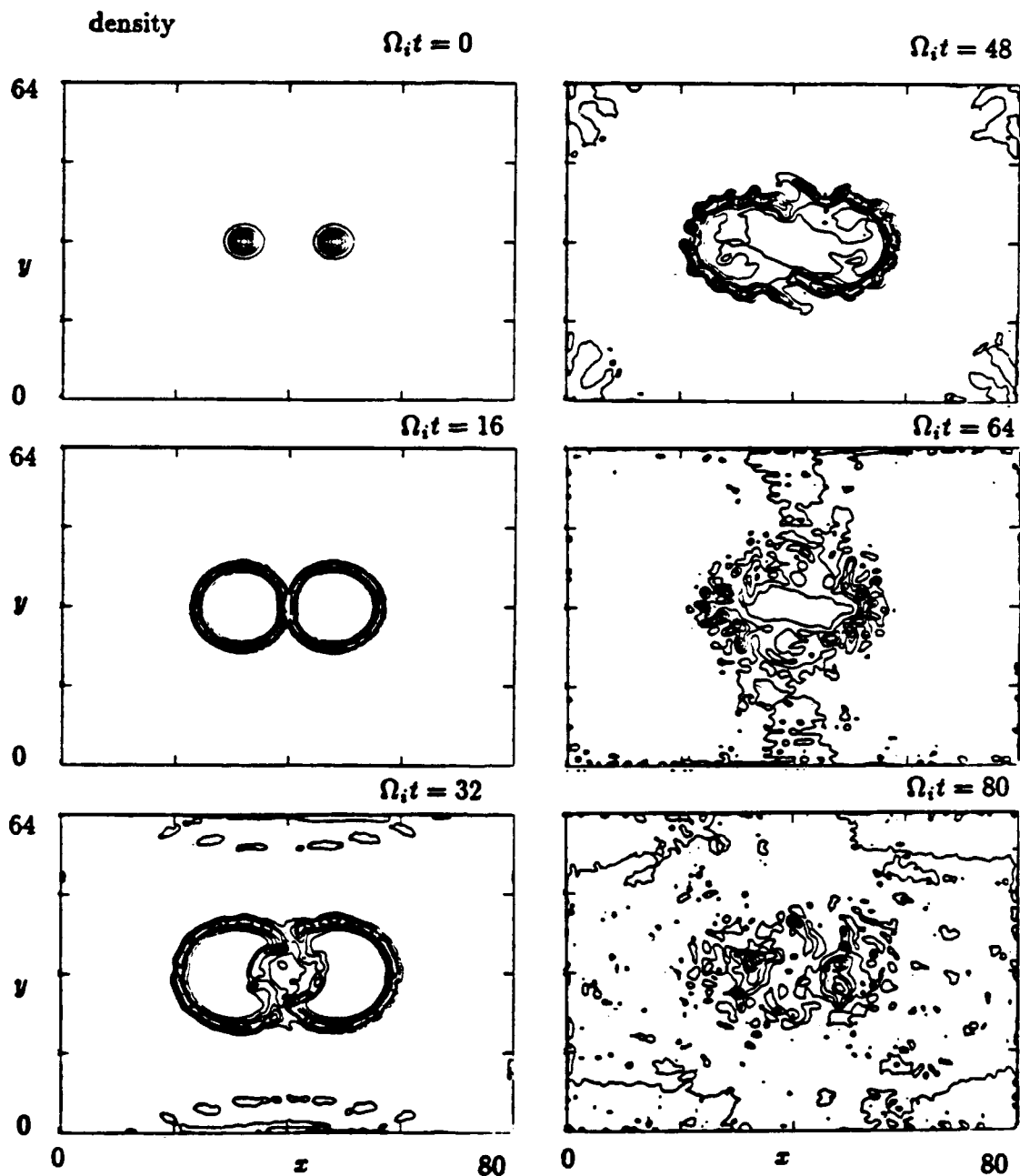


Figure 5.4. Hybrid simulation of two simultaneous debris expansions, showing ion density contours at various times.

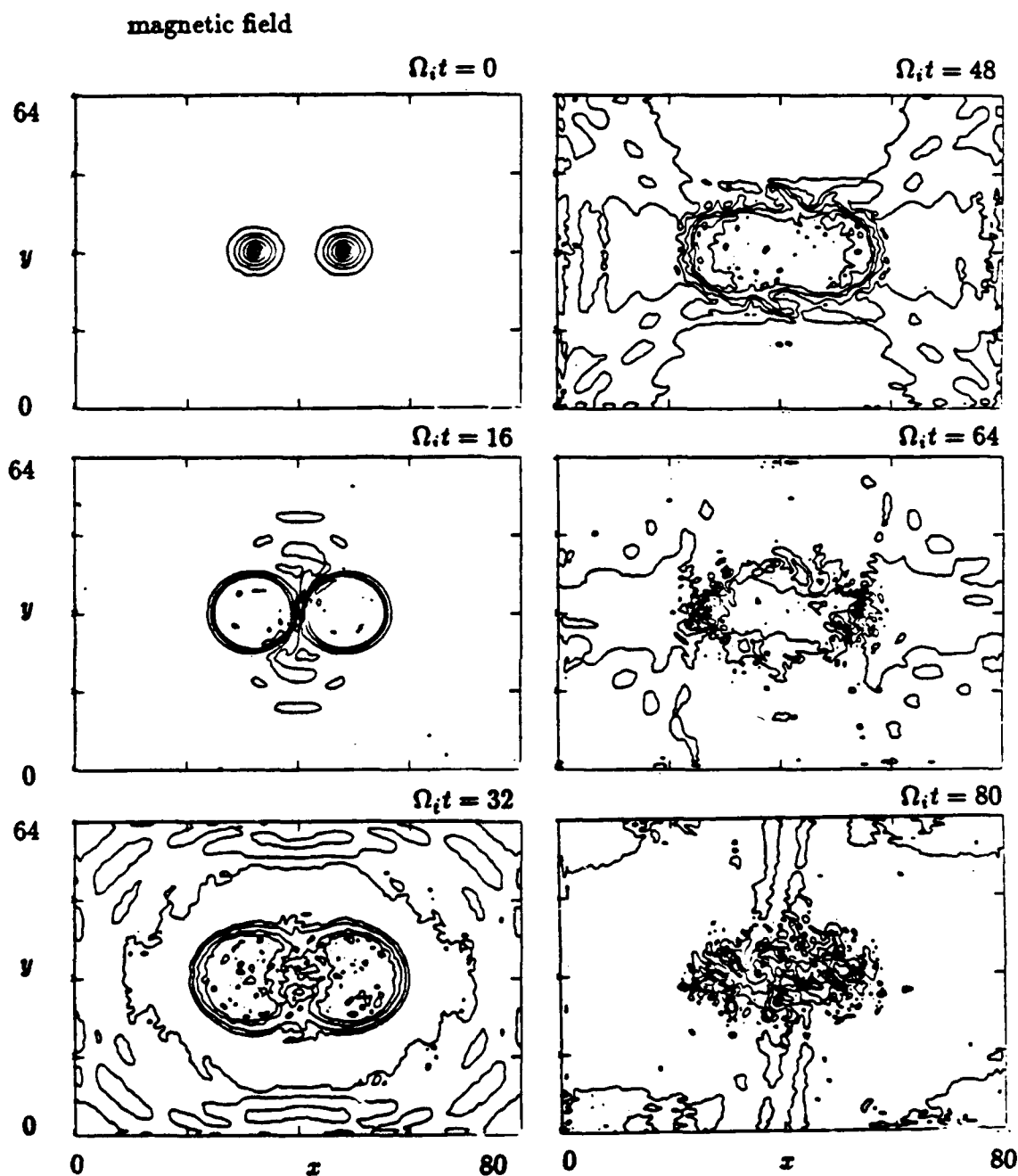


Figure 5.5. Corresponding magnetic field contours for the same case, showing the merging of the two clouds to form one large cavity.

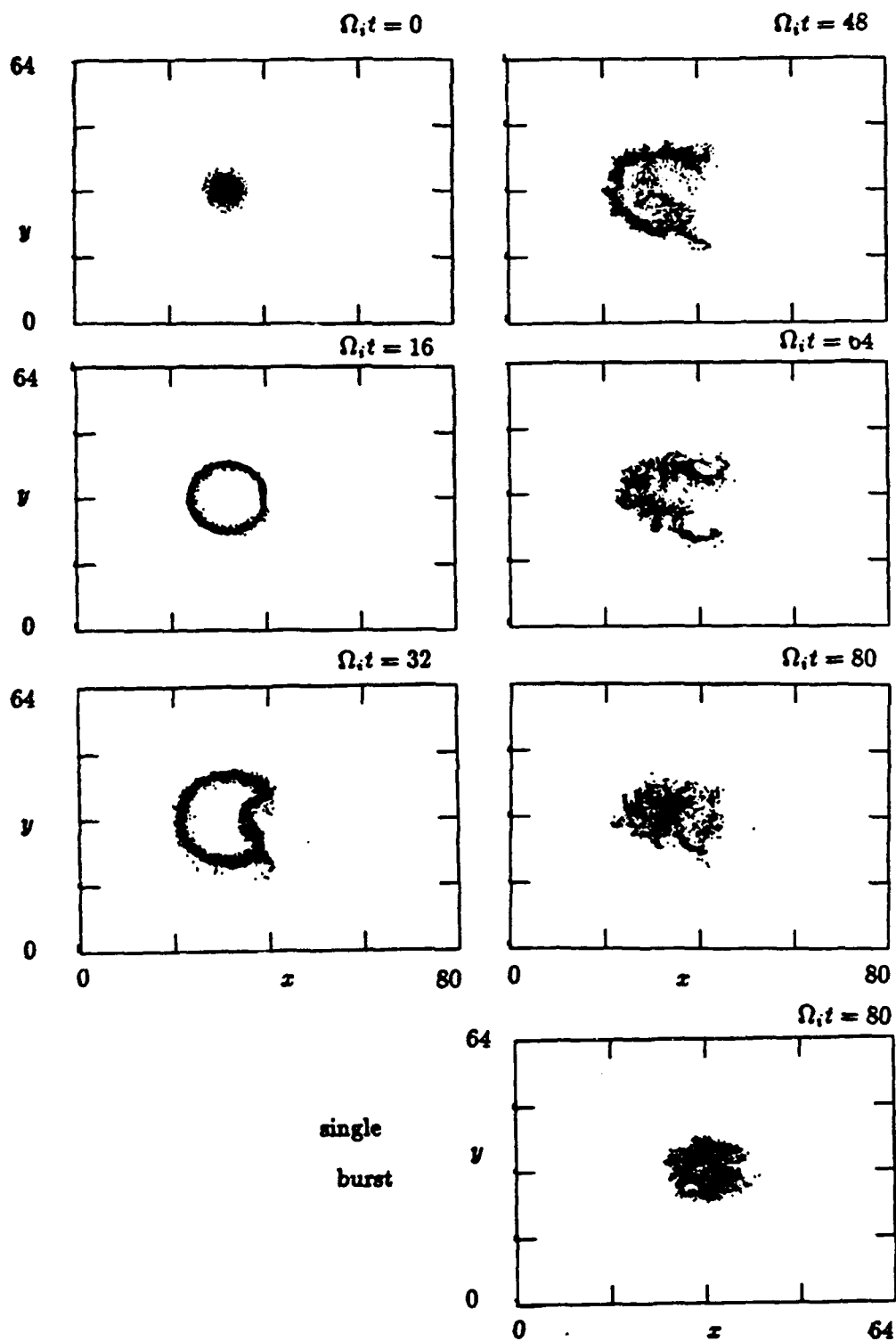


Figure 5.6. Results of the same hybrid run showing ions from one burst in the x-y plane at various times; results for the single burst case at the same final time shown for comparison.

Corresponding velocity space plots of these same ions are given in Figure 5.7. As the debris expands, the radial velocity decreases. In this case, however, there is some energization as the two clouds collide ($\Omega_i t = 32$). The more energetic ions have been reflected off the interface of the two colliding clouds. As in the runs in Section 1, at later times the ions are heated as the magnetic field collapses. Although difficult to see in the bottom two panels, the ion heating in the multiburst case is actually greater than in the single burst. (While some ions in the single burst end up at higher velocities, the multiburst case has a flatter velocity distribution and hence proportionally more ions at higher energy.)

5.4 Summary

In this section we have shown examples of VHANE multiburst simulations carried out with full particle and hybrid codes. Both types of calculations exhibit many features seen in single bursts in the VHANE regime, especially the expansion of the plasma dragging the magnetic field to form a diamagnetic cavity and the development of structure on the surface of the expanding cloud. And, as discussed in Section 1, there is also some heating of the plasma that occurs as the magnetic field recollapses. However, the multiburst cases also show new and interesting effects that strongly support the notion that multibursts cannot simply be modeled as a superposition of single bursts. These include additional heating of the ions and electrons, and acceleration or deceleration of the colliding debris. A first analysis of these simulations suggest that the new effects are due to the interaction of the plasma in one burst with the macroscopic and microscopic fields generated by the other burst. The macroscopic electric field that is produced in the compression shell of one burst can either accelerate ions from the other burst toward the center of the first burst if there is no background plasma, or reflect the ions when there is background plasma compressed between the two clouds. The motion of ions is also affected by the absence of the magnetic field when they enter the cavity of the other burst.

Microscopic fields due to the lower hybrid drift instability that generates structure on the surface of the clouds also contributes to the ion and electron heating. In particular, it is felt that the large and isotropic electron heating results from this type of interaction, rather than from the excitation of some sort of ion/ion instability. Such cross-field instabilities [Lampe *et al.*, 1975] can occur near the end of the expansion, when the relative ion-ion speed drops below the local Alfvén speed. Such instabilities do not occur in the hybrid formation with $m_e = 0$ and are not well resolved in the full particle simulations (small m_i/m_e precludes many growth times during the interaction). Such instabilities, however, cannot be ruled out in an actual VHANE multiburst.

VHANE multibursts would be a very interesting study using the AGNES facility at NRL. The VHANE regime is easily modeled using the existing experimental conditions [Ripin *et al.*, 1987]. The above simulations suggest that there are several new effects that can be investigated, both in the presence or in the absence of a background plasma. In addition, multiburst experiments could be used to help resolve the old issue of debris air coupling, by examining the cross-field ion instabilities mentioned above without the need

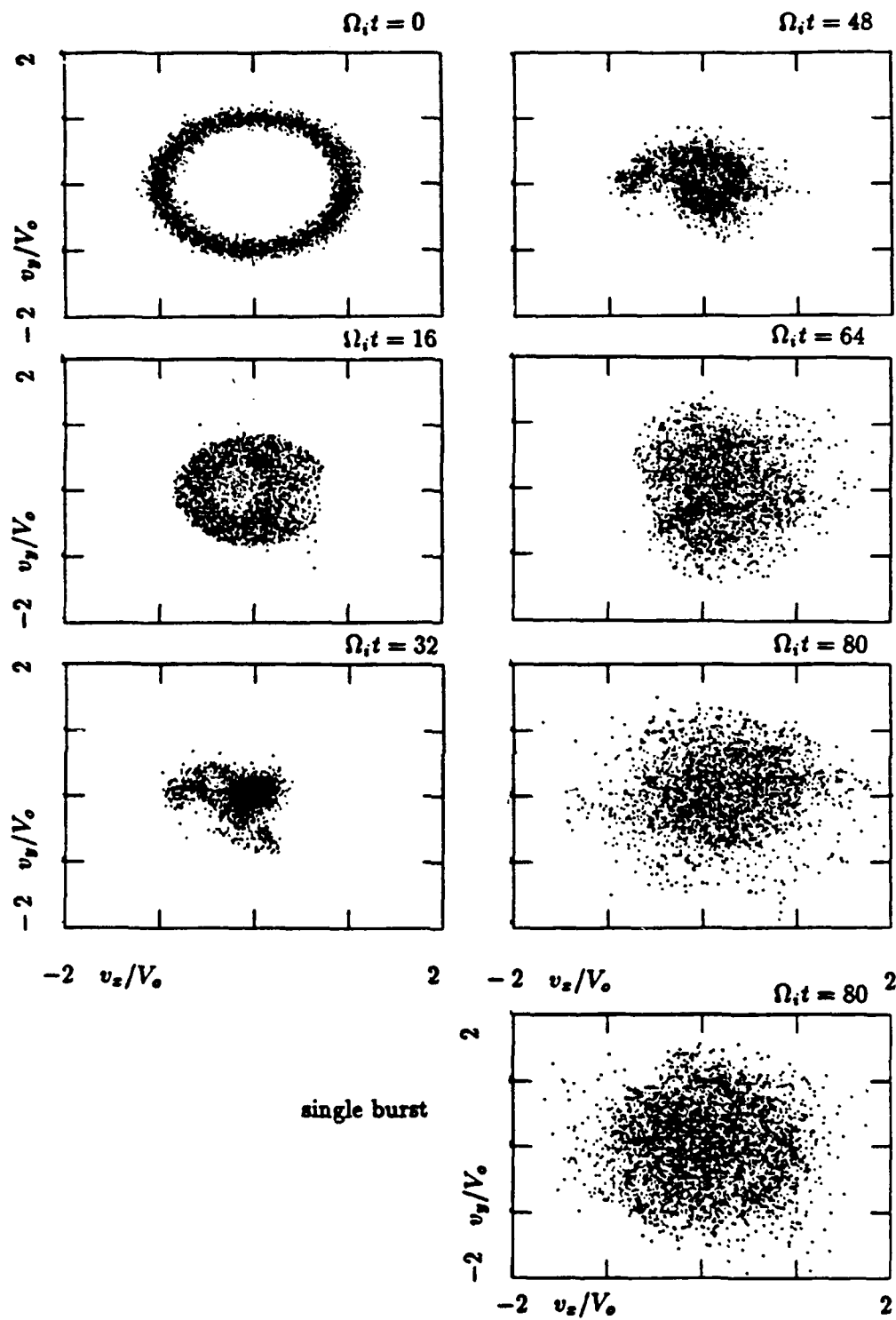


Figure 5.7. Results for the same run showing the ions in velocity space.

for a preionizer. Laser experiments have already been successfully employed to study ion-ion interactions for the ICF program [Berger *et al.*, 1991] and similar studies could be very relevant to the early time problem. We are presently working out the details of such an experiment and will present the results in a future report.

References

- Berger, R. L., J. R. Albritton, C. J. Randall, E. A. Williams, W. L. Kruer, A. B. Langdon, and C. J. Hanna, Stopping and thermalization of interpenetrating plasma streams, *Phys. Fluids B*, 3, 3, 1991.
- Brecht, S. H., and V. A. Thomas, Contact authors for reference, 1988.
- Lampe, M., W. M. Manheimer, and K. Papadopoulos, Anomalous transport coefficients for HANE applications due to plasma microinstabilities, NRL Memo Report 3076, 1975.
- Ripin, B. H., E. A. McLean, C. K. Manka, C. Pawley, J. A. Stamper, T. A. Peyser, A. N. Mostovych, J. Grun, A. B. Hassam, and J. D. Huba, Large Larmor radius interchange instability, *Phys. Rev. Lett.*, 59, 2299, 1987.
- Sappenfield, D., Contact author for reference, 1987.
- Winske, D., The lower hybrid drift instability as mechanism for early time structuring, Los Alamos Report LA-UR 87-2572, 1987.
- Winske, D., Early time structuring at very high altitudes: instability mechanism, properties, and consequences, Los Alamos Report LA-UR 88-3118, 1988.
- Winske, D., Plasma dynamics in very high nuclear explosions: 1. ions, Los Alamos Report LA-UR 90-1005, 1990.
- Winske, D., and M. E. Jones, Plasma dynamics in very high altitude nuclear explosions: 2. electrons, Los Alamos Report LA-UR 90-3282, 1990.

Distribution List

Prof. D. Papadopoulos
Astronomy Program
University of Maryland
College Park, MD 20742

Dr. J. D. Huba
Code 4780
Naval Res. Lab.
Washington, DC 20375

Dr. S. Brecht
Berkeley Research Associates
P.O. Box 241
Berkeley, CA 94701

Dr. N. T. Gladd
Berkeley Research Associates
P.O. Box 241
Berkeley, CA 94701

Dr. J. Workman
Berkeley Research Associates
P.O. Box 241
Berkeley, CA 94701

Dr. D. Simons
ESS-7
MS D466

Dr. M. Pongratz
ESS-DOT
MS D446

Dr. B. H. Ripin
Code 4732
Naval Res. Lab.
Washington, DC 20375

Dr. E. McLean
Code 4732
Naval Res. Lab.
Washington, DC 20375

Dr. D. Sowle
Mission Research Corp.
P. O. Box 719
Santa Barbara, CA 93102

Dr. T. Mazurek
Mission Research Corp.
P. O. Box 719
Santa Barbara, CA 93102

Dr. C. Longmire
Mission Research Corp.
P. O. Box 719
Santa Barbara, CA 93102

Dr. E. Witt
Mission Research Corp.
P. O. Box 719
Santa Barbara, CA 93102

Dr. J. M. Cornwall
Dept. of Physics
UCLA
Los Angeles, CA 90024

Dr. D. Hammer
Laboratory for Plasma Studies
809 Upson Hall
Cornell University
Ithaca, NY 14853

Dr. H. Carl Fitz
Physical Research, Inc.
134 Holiday Ct., Suite 309
Annapolis, MD 21401

Dr. R. Armstrong
Mission Research Corp.
One Tara Blvd. Suite 302
Nashua, NH 03062

Dr. C. K. Manka
Code 4732
Naval Res. Lab.
Washington, DC 20375

Dr. Paul Bernhardt
Code 4780
Naval Res. Lab.
Washington, DC 20375

Dr. E. Hyman
SAIC
1710 Goodridge Dr.
McLean, VA 22102

Dr. L. Wittwer
RAAE
Defense Nuclear Agency
6801 Telegraph Rd.
Alexandria, VA 22310-3398

Dr. B. Prasad
RAAE
Defense Nuclear Agency
6801 Telegraph Rd.
Alexandria, VA 22310-3398

Director
Attn: CSTI
Defense Nuclear Agency
6801 Telegraph Rd.
Alexandria, VA 22310-3398

Dr. R. W. Kilb
Mission Research Corp.
P. O. Box 719
Santa Barbara, CA 93102

Dr. W. W. White
Mission Research Corp.
One Tara Blvd. Suite 302
Nashua, NH 03062

Dr. M. Hausman
Mission Research Corp.
P. O. Box 719
Santa Barbara, CA 93102

Defense Technical Information Center
Cameron Station
Alexandria, VA 22314

Dr. R. Henderson, W385
Director, JASON Program Office
The MITRE Corp.
7525 Colshire Dr.
McLean, VA 22102

DASIAC
815 State St.
P.O. Drawer QQ
Santa Barbara, CA 93102

Dr. G. Simonson
L-84
Lawrence Livermore Natl. Lab.
Livermore, CA 94550

Dr. J. H. Thompson
Physical Research, Inc.
P.O. Box 30129
Santa Barbara, CA 93130